

Thesis

BELFKIR Mohamed

December 2020

Contents

1	Introduction	11
2	Theoretical Framework	13
2.1	Introduction	13
2.2	Standard Model (SM) of particle physics	14
2.2.1	Elementary Particles	14
2.2.2	Elementary Interactions	15
2.3	Electroweak Symmetry Breaking (EWSB)	18
2.4	Higgs Boson Discovery	19
2.4.1	p-p collisions	20
2.4.2	Higgs boson production	21
2.4.3	Higgs boson decay channels	24
2.4.4	Higgs measurements	25
2.5	Double Higgs boson	28
2.5.1	Di-Higgs production and decays	28
2.5.2	Di-Higgs as a probe of BSM physics	31
2.5.3	Current Measurements	33
2.6	Effective Field Theory (EFT)	36
2.7	Conclusion	36
3	The Large Hadron Collider and the ATLAS detector	39
3.1	The Large Hadron Collider	39
3.1.1	Acceleration chain	40
3.1.2	Luminosity	41
3.1.3	Pile-up	43
3.2	ATLAS A Toroidal LHC ApparatuS detector	43
3.2.1	Coordinated system	44
3.2.2	The Inner Tracker	44
3.2.3	Calorimeter system	48
3.2.4	Muon Spectrometer	51
3.2.5	Trigger	53
3.3	Physics objects reconstruction	54
3.3.1	Track and Vertex reconstruction	54
3.3.2	Electron and Photon reconstruction	54
3.3.3	Muon reconstruction and identification	63
3.3.4	Jet reconstruction	65
3.3.5	Missing transverse energy	65

4 Photons in ATLAS	67
4.1 Photons Isolation	67
4.2 Photons Identification	68
4.3 Shower shape mis-modelling	71
4.3.1 Cell-based reweighting correction	71
4.3.2 Electron results	72
4.3.3 Cell-based reweighting for photons	73
4.4 Convolutional Neural Network for Photon Identification	79
4.5 Conclusion	85
5 Jets and Tagging in ATLAS	89
5.1 Jet Reconstruction	89
5.1.1 Topological Cluster	89
5.1.2 Particle Flow	89
5.2 Jet Tagging	89
5.2.1 Jet Vertex Tagging	89
5.2.2 B-jet Tagger	89
5.3 Jet Energy Calibration	90
5.3.1 Jet Calibration Chain	90
5.3.2 B-Jet Calibration	90
5.4 Conclusion	90
6 Experimental Setup for Self-coupling measurement	91
7 Conclusion	93
8 Appendix 1	95

List of Figures

2.1	Shape of the Higgs potential for $\mu^2 < 0$ this potential has an infinite amount of minima. [5]	18
2.2	The χ^2 function for the SM as a function of the Higgs mass, LEP and Tevatron exclusions limits are shown.	20
2.3	The CT14 PDFs at $Q=2$ GeV (left) and $Q = 100$ GeV (right) for different partons. These PDFs are computed at next-to-next-to-leading order.	21
2.4	Feynman diagrams for the main production modes of Higgs boson.	22
2.5	Cross sections for different Higgs boson production modes at a proton-proton collider with a centre-of-mass energy of 6-15 TeV (a). A Higgs mass of 125 GeV is assumed in this plot. Additionally, cross sections as a function of Higgs mass are shown (b) [12].	23
2.6	Higgs boson total decay width as a function of Higgs mass [13].	24
2.7	Higgs boson branching ratio of the possible Higgs decay channels as a function of the Higgs mass [14]	24
2.8	Feynman diagrams of the $H \rightarrow \gamma\gamma$ decay. Other particles can also propagate in the loop.	25
2.9	Weighted distributions of the invariant mass of di-photon [16].	26
2.10	The observed local p-value as a function of m_H (solid line) and the expectation with its $\pm 1\sigma$ band assuming the presence of a Standard Model Higgs boson at that mass (dashed line) from the combination of the ZZ^* , $\gamma\gamma$ and WW^* channels by the ATLAS experiment. The horizontal dashed lines indicate the p-values corresponding to significances of 1 to 6σ [16].	26
2.11	The inclusive diphoton invariant mass distribution [19].	27
2.12	Cross sections times branching fraction for $ggF+b\bar{b}H$, VBF , VH and $t\bar{t}H+tH$ production, normalized to their SM predictions [19].	27
2.13	The particle content of the Standard Model (SM).	28
2.14	Leading Order (LO) Feynman diagrams contributing to ggF Higgs boson pair production through a top-quark loop (box) and through the triple self-coupling of the Higgs boson (triangle).	29
2.15	HH production modes, in decreasing order of cross section. λ refers to Higgs tri-linear coupling: (a) ggF mode, (b) VBF mode, (c) Vector boson association (VH) and (d) top associated production.	30
2.16	Total cross sections at the NLO for HH production as a function of centre-of-mass energy. Assuming κ_λ and κ_t equals to their SM values.	30
2.17	Di-Higgs system decay branching ratios assuming SM Higgs bosons with $m_H = 125.09$ GeV.	31
2.18	Illustration of both box and triangle diagrams contribution to di-Higgs invariant mass spectrum.	32
2.19	Higgs pair invariant-mass distribution in ggF for various values of κ_λ assuming $\kappa_t = 1$	33

2.20	Total LO and NLO cross sections for HH production at the LHC with $\sqrt{s} = 14$ TeV, as a function of the self-interaction coupling κ_λ	33
2.21	The expected and observed 95% CL limits on the non-resonant production cross section $\sigma_{gg \rightarrow HH}$ as a function of κ_λ . The red line indicates the predicted HH cross section if κ_λ is varied but all other couplings remain at their SM values. The red band indicates the theoretical uncertainty of this prediction.	34
2.22	Upper limits at 95% CL on the cross-section of the ggF SM HH production normalised to its SM expectation $\sigma_{gg \rightarrow HH}^{SM}$ from the $b\bar{b}\tau\tau$ [24], $b\bar{b}b\bar{b}$ [25], $b\bar{b}\gamma\gamma$ [22], $WWWW$ [26], $WW\gamma\gamma$ [27] and $b\bar{b}WW$ [28] searches, and their statistical combination.	35
2.23	Upper limits at 95% CL on the cross-section of the ggF non-resonant as a function of κ_λ	35
3.1	Overview of the CERN accelerator complex, including the LHC and its pre-accelerators [33]. The four main LHC experiments are depicted, too	40
3.2	Cumulative luminosity versus time delivered to (green), recorded by ATLAS (yellow), and certified to be good quality data (blue) during stable beams and for pp collisions at 7 and 8 TeV centre-of-mass energy in 2011 and 2012 (Run 1).	42
3.3	Luminosity delivered by the LHC during the Run 2 data taking. ATLAS recorded this data with an efficiency above 90%.	42
3.4	Recorded integrated luminosity as function of the mean number of interaction per bunch crossing in pp collisions recorded by the ATLAS detector during Run 2 at 13 TeV [34].	43
3.5	Sketch of the ATLAS detector with its different sub-detectors.	44
3.6	Coordinate system used by the ATLAS and CMS experiments at the LHC.	45
3.7	Layout of the Inner Detector (ID) [38].	45
3.8	(a) Transverse view of 3 of the Insertable-B-Layer (IBL) staves, located directly on the beam pipe. (b) The layout of one of the 14 IBL staves [38].	46
3.9	Unfolded longitudinal impact parameter resolution measured from data in 2015, $\sqrt{s} = 13$ TeV, with the Inner Detector including the IBL, as a function of η for values of $0.4 \leq p_T \leq 0.5$ GeV compared to that measured from data in 2012, $\sqrt{s} = 8$ TeV [40].	47
3.10	The average efficiency to reconstruct primary tracks with a production vertex before the first layer in jets as a function of jet p_T . The same sample generation, with limited statistics, is used for both reconstruction algorithms resulting in correlated features [42].	48
3.11	Rejection factor against light jets as a function of b -jet efficiency for the combined IP3D+SV1 tagger. Compared are the results with and without IBL.	49
3.12	The Perigee representation of the track [45].	50
3.13	ATLAS Calorimeter system.	51
3.14	Accordion shape of the EM calorimeter.	52
3.15	Side view of one quadrant (<i>right</i>) and transverse view (<i>left</i>) of the muon spectrometer.	53
3.16	Transverse cross section of the MDT tube.	53
3.17	The primary track reconstruction efficiency in minimum bias Monte Carlo samples containing exactly one and on average 21 or 41 interactions. The distributions are shown for tracks passing the default(dashed) and robust (solid) requirements.	55
3.18	The vertex reconstruction efficiency (<i>left</i>) and fake probability (<i>right</i>) as a function of the average number of interactions.	55
3.19	Diagram of the super clustering algorithm for electrons and photons. Seed clusters are shown in red, satellite clusters in blue.	56
3.20	The cluster, track, cluster and track, and electron reconstruction efficiencies as a function of the generated electron E_T	57

3.21	The converted photon reconstruction efficiency and contributions of the different conversion types as a function of E_T^{true}	57
3.22	Flowchart showing the logic of the ambiguity resolution for particles initially reconstructed both as electrons and photons.	58
3.23	Schematic overview of the calibration chain for the electron and photon energies [64].	58
3.24	Schema of the calorimeter isolation method: the grid represents the second-layer calorimeter cells in the η and ϕ directions. The candidate electron is located in the centre of the purple circle representing the isolation cone. All topological clusters, represented in red, for which the barycentres fall within the isolation cone are included in the computation of the isolation variable. The 5x7 cells represented by the yellow rectangle correspond to the subtracted cells in the core subtraction method.	61
3.25	Efficiency of the different isolation working points for electrons from inclusive $Z \rightarrow e^+e^-$ events as a function of the electron E_T . The lower panel shows the ratio of the efficiencies measured in data and in MC simulations [67].	62
3.26	The transformed LH-based identification discriminant d_L for reconstructed electron candidates with good quality tracks with $30 < E_T < 35$ GeV and $ \eta < 0.6$ [70].	62
3.27	The electron identification efficiency in $Z \rightarrow e^+e^-$ events in data as a function of E_T for the Loose, Medium and Tight operating points.	63
3.28	Muon reconstruction and identification efficiencies for the <i>Loose</i> , <i>Medium</i> and <i>Tight</i> criteria as function of p_T . The panel at the bottom shows the ratio of the measured to predicted efficiencies, with statistical and systematic uncertainties.	65
4.1	Distribution of E_T^{cone40} in data and simulation, in the central region of the detector ($ \eta < 0.6$), separately for converted (left) and unconverted (right) photons after the data-driven shifts are applied.	68
4.2	Efficiency of the isolation working points for converted(left) and unconverted (right) photons as a function of photon E_T . The lower panel shows the ratio of the efficiencies measured in data and in simulation (scale factors).	68
4.3	Schematic representation of the photon identification discriminating variable [81].	69
4.4	Distributions of the R_η and w_{s3} for converted and unconverted photon candidates with E_T in [10,50] GeV and $ \eta < 2.37$ selected from radiative Z events for data (black), uncorrected MC (dashed red line) and the corrected MC (solid blue line).	70
4.5	The photon identification efficiency with E_T -dependent selection, and the ratio of data to MC efficiencies, for unconverted photons with a Loose isolation requirement applied as pre-selection, as a function of E_T in four different $ \eta $ regions. The combined scale factor, obtained using a weighted average of scale factors from the individual measurements, is also presented; the band represents the total uncertainty.	71
4.6	The photon identification efficiency with E_T -dependent selection, and the ratio of data to MC efficiencies, for converted photons with a Loose isolation requirement applied as pre-selection, as a function of E_T in four different $ \eta $ regions. The combined scale factor, obtained using a weighted average of scale factors from the individual measurements, is also presented; the band represents the total uncertainty.	72
4.7	Efficiencies of the Tight photon identification for unconverted (left) and converted (right) signal photons, plotted as a function of photon E_T . The Loose isolation is applied as a pre-selection. For both plots, the bottom panel shows the ratios between the E_T -dependent and the E_T -independent identification efficiencies.	73

4.8 (a) Energy profile in η direction, (b) Energy profile in ϕ direction, (c) R_η variable and (d) R_ϕ variable before (red) and after reweighting for electrons from $Z \rightarrow e^+e^-$ for $1.80 < \eta < 2.00$ first column and $0.40 < \eta < 0.60$ in the second column (the bottom plot is the data/MC ratio).	74
4.9 The energy profile in ϕ and η directions (a,b) and the corresponding R_ϕ and R_η variables, for unconverted photons with $0.40 < \eta < 0.60$. The black points correspond to Data 2017, red points to non-reweighted MC and blue points to the reweighted MC from $Z \rightarrow ll\gamma$	75
4.10 The energy profile in ϕ and η directions (a,b) and the corresponding R_ϕ and R_η variables, for unconverted photons with $0.40 < \eta < 0.60$. The black points correspond to Data 2017, red points to non-reweighted MC and blue points to the reweighted MC from $Z \rightarrow ll\gamma$	76
4.11 The energy profile in ϕ and η directions (a,b) and the corresponding R_ϕ and R_η variables, for unconverted photons with $0.40 < \eta < 0.60$. The black points correspond to the pseudo data, red points to non-reweighted MC and blue points to the reweighted MC from $Z \rightarrow ll\gamma$	77
4.12 The energy profile in ϕ and η directions (a,b) and the corresponding R_ϕ and R_η variables, for unconverted photons with $1.00 < \eta < 1.20$. The black points correspond to the pseudo data, red points to non-reweighted MC and blue points to the reweighted MC from $Z \rightarrow ll\gamma$	78
4.13 CNN classifier schema.	80
4.14 Illustration of the global CNN classifier graph.	81
4.15 Neural network loss and accuracy as function of epoch number	82
4.16 Network ROC curve for (a) Unconverted photons (b) Converted photons, the yellow line show the ROC curve and the blue dot show the Tight WP, x-axis is the ϵ_{eff} and y-axis show the ϵ_{rej} as defined in equation 4.5.	83
4.17 Relative signal efficiency improvement for similar Tight WP background rejection (a) for Unconverted photons and (b) Converted photons.	84
4.20 CNN output distribution as computed for data (black) and MC (blue) for (a) for Unconverted photons and (b) Converted photons with $ \eta < 0.4$	84
4.18 Photon identification efficiency for CNN (red) and cut-based (blue) indicated with ATLAS, for data (full marks) and MC (open marks). For both Tight WP (top) and Loose WP (bottom). Unconverted photons (right) and converted photons (left). As a function of photon E_T . Bottom ratios show the scale factors. 2017 Data is used.	86
4.19 Photon identification efficiency for CNN (red) and cut-based (blue) indicated with ATLAS, for data (full marks) and MC (open marks). For both Tight WP (top) and Loose WP (bottom). Unconverted photons (right) and converted photons (left). As a function of pile up $<\mu>$. Bottom ratios show the scale factors. 2017 Data is used.	87

List of Tables

2.1	Generations of quarks and leptons with their masses and electrical charges	15
2.2	The 95% CL observed and expected limits on the Higgs boson pair cross-section in pb and as a multiple of the SM production cross-section. The $\pm 1\sigma$ band around each 95% CL limit is also indicated.	34
2.3	The 95% CL observed and expected limits on the Higgs boson pair cross-section normalized to the SM production cross-section and the allowed κ_λ interval.	35
3.1	Granularity of the EM calorimeter ($\Delta\eta \times \Delta\phi$) [46].	50
3.2	Discriminating variables used for electron and photon identification. The usage column indicates if the variables are used for the identification of electrons, photons, or both. [60].	59
3.3	Definition of the electron isolation working points.	60
4.1	Definition of the photon isolation working points.	67
4.2	Discriminating variables used for Loose, Medium and Tight photon identification.	69
4.3	Number of cells in 7x11 EM calorimeter windows.	79
4.4	Image shape of 7x11 windows in each sampling in (η, ϕ)	80

Introduction

Theoretical Framework

This chapter should contains all theory needed for SM:

- Describe the elementary particles
- Describe the fundamental interactions and their related fields
- Describe the EWSB and Higgs physics introduction
- Brief introduction to p-p collision and higgs production at LHC
- Discovery of Higgs boson at CERN 2012
- Higgs self coupling anomaly
- Describe Di-Higgs production as a direct process to measure higgs self coupling and probe of BSM effects
- Early Run 2 results and limits on κ_λ
- Introduction to EFT as an alternative interpretation of Full Run 2 results to probe physics at large scale

2.1 Introduction

This section should include a brief history of particle physics and the SM.

How the world around us made? How does it work? These are questions asked a long-ago to understand the Universe. The first efforts to elucidate those questions referred to ancient Greek philosophers. Greeks gave much to the physics by developing the fundamental basis of modern principles as the conservation of matter, atomic theory. Democritus's model introduced Atom as small indivisible building blocks (particles) that matter consists off. At that time, atoms allowed to describe a variety of phenomena.

Rutherford came in 1909 with his experience saying that atoms consist of mostly space with Electrons surrounding a dense central nucleus made up of Protons and Neutrons. At that time, Newtonian laws of motion and atoms provided a solid framework. A continuing collaboration between theorists and experimentalists brought us to a simple theory upon which all modern physic the Standard Model (SM). Currently, SM is the most accurate model describing the universe composition. In the SM, there are two types of elementary particles: fundamental constituents of matter called "Fermions", and the quanta of fields called "Bosons" exchanged between when an interaction occurs between fermions. The SM has been successfully, so far, at predicting the results from the measurements performed in the past 50 years. The following sections provide more details about the Standard Model and its particles.

2.2 Standard Model (SM) of particle physics

One of the physicist goal is to describe all natural phenomena with a minimal set of fundamental laws and theories which, at least in principle, can quantitatively explain and predict experimental results. At the microscopic scale, all matter behaviour and phenomenology, including molecular, atomic, nuclear, and subnuclear physics, are explained under three fundamental interactions: electromagnetic, weak and strong forces. At the macroscopic scale, the fourth force, the gravitational interaction, has an essential role, but has negligible at the microscopic scale. All the three interactions are described within a local relativistic Quantum Field Theory (QFT) based on the principal gauge invariance of $SU(3)\times SU(2)\times U(1)$. This is "The Standard Model" of particle physics. Within the SM matter consists of fermions and interactions are mediated by bosons.

2.2.1 Elementary Particles

This should include a description of elementary particles, Fermions and Bosons and their properties (mass, spin, charge, quantum number)

In the SM, particles are classified as either fermions or bosons depending on what statistics they obey. Fermions obey Fermi-Dirac statistics and respect the Pauli exclusion principle, i.e. two fermions in the same quantum state can not exist in the same place and time. Such particles have an intrinsic angular momentum, called spin J equal to half-integer. Bosons obey Bose-Einstein statistics, due to spin-statistics theorem, corresponding to integer spin value. Through an interaction, a boson emitted by a matter particle and then absorbed by another particle. Fermions are divided into two categories: Leptons and Quarks.

2.2.1.1 Leptons

Leptons (comes from the Greek word meaning "light") are grouped into three families or generations formed by three charged leptons: electron e , muons μ and tau τ with electric charge $-e$, where e is equal to the elementary electric charge of $\sim 1.6 \cdot 10^{-19} C$ [1], and their neutral complemented partners neutrinos : ν_e, ν_μ and ν_τ . Only electron and neutrinos are stable. A quantum number called Leptonic number (L) is associated with each lepton. Electron, muon and tau have identical properties (a charge, spin) however tau is 3477 times heavier than an electron while the muon is only 17 times the mass of an electron. The rest mass of an electron is $9.10938356 \cdot 10^{-31} Kg$. In high energy physics, the particle mass is expressed in energy with the equivalence $E = mc^2$ where the velocity of light in vacuum. Electron mass is 511 keV, with c fixed to one.

2.2.1.2 Quarks

Quarks are electrically charged particles, with charge of $+\frac{2}{3}e$ for so-called up-type quarks and $-\frac{1}{3}e$ for the down-type quarks. There are six known quark flavours, similarly to leptons, quarks are paired into three generations. The first generation consists of up (u) and down (d) quarks, the second has the charm (c) and strange (s) quarks, and top (t) and bottom (b) quarks for the third generation. Quarks can not exist in a free state due to the QCD color confinement. Table 2.1 summarises leptons and quarks.

Each of the higher generations has particles with higher mass and tends to decay to the lower one, explains why the ordinary matter made off the first-generation particles. Each fermion is associated with a corresponding anti-particle.

	1st Generation	2nd Generation	3rd Generation
Quarks	u 2.16 MeV $+\frac{2}{3}$	c 1.27 GeV $+\frac{2}{3}$	t 172.4 GeV $+\frac{2}{3}$
	d 4.67 MeV $-\frac{1}{3}$	s 93 MeV $-\frac{1}{3}$	b 4.18 GeV $-\frac{1}{3}$
Leptons	e 0.511 MeV -1	μ 105.7 MeV -1	τ 1.8 GeV -1
	ν_e 0 0	ν_μ 0 0	ν_τ 0 0

Table 2.1: Generations of quarks and leptons with their masses and electrical charges

Standard Model of elementary particles assumes neutrinos to be mass-less particles, while some experiments demonstrate that neutrinos have a non-negligible mass $\sim eV$, which makes it an incomplete theory.

2.2.1.3 Bosons

As mentioned before, bosons are particles of integer angular momentum and obey to the Bose-Einstein statistics. They are the carriers of the gauge interactions between fermions. Photon (γ) is a boson known as a quantum of the electromagnetic field including electromagnetic radiation such as light. Photons are neutral and mass-less particles. W^\pm, Z^0 are bosonic particles wish carriers the weak interaction. Z^0 boson is neutral while W^\pm charged with a charge of $\pm e$. Contrary to photons, Weak bosons are massive. W^\pm and Z^0 have been predicted at the end of 1972 by the charged (CC) and neutral currents (CN) of the weak interaction, and their masses are predicted to be so large that it took many years to build powerful accelerators to produce them. They are directly discovered at CERN in 1983 by the UA1 and UA2 collaborations [2, 3] and their masses were found to be about 80 GeV and 91 GeV respectively. Gluons are the neutral quantum of the strong force known as the "glue" that links quarks to form hadrons. The mass of the gluons is known to be strictly zero. There are eight gluons.

2.2.2 Elementary Interactions

This should include a description of the 4 interaction and their properties.

The associated group for each of the SM interactions (U(1) SU(2) SU(3)) and the its Lagrangian.

How SM combines the 3 groups in one fundamental theory which describe particle physics.

Brief summary of boson vs interactions

At the microscopic level, there are three fundamental forces: electromagnetic, weak and strong. The interactions relate to matter (fermions) by the transmission of a boson. The SM content and interactions are expressed more formally through the concepts of symmetries and gauge invariance. Each interaction is described through a gauge group. The generators of the group correspond to the gauge bosons that are mediators of the fundamental force and responsible for the interactions. The electromagnetic interaction mediated by photons, the weak force used W^\pm and Z^0 as mediators, while the gluons are mediators for the strong interaction.

2.2.2.1 Electromagnetic interaction

Electromagnetic interaction describes the dynamics of electrically charged fermions. It is described by the Quantum Electrodynamics (QED). Each quantum field theory is represented by a Lagrangian density. The QED Lagrangian representing the behaviour of a freely propagating fermion field $\psi(x, t)$ can be written as :

$$\mathcal{L} = \bar{\psi} i\gamma^\mu \partial_\mu \psi - m\psi\bar{\psi}, \quad (2.1)$$

where m is the mass of the particle. The Einstein convention is used here, with the indices $\mu = 0, 1, 2, 3$ representing the space-time components x and t .

To be a valid gauge theory the QED lagrangian should be invariant under a $U(1)$ (electromagnetic force group) local gauge transformation of the field : $\psi \rightarrow e^{i\alpha(x)}\psi$. This condition leads to additional terms to be added to the lagrangian and new gauge field A_μ that represents the photon:

$$\mathcal{L}_{QED} = \bar{\psi} i\gamma^\mu \partial_\mu \psi - m\psi\bar{\psi} + q\psi\gamma^\mu\psi A_\mu - \frac{1}{4}F^{\mu\nu}F_{\mu\nu}, \quad (2.2)$$

where $F^{\mu\nu} = -F^{\nu\mu} = \partial^\nu A^\mu - \partial^\mu A^\nu$ is the field-strength tensor for the electromagnetic force describes the kinetic propagation of the field. Note that $U(1)$ is an Abelian group which means that photons can not self-interact and the EM tensor does not have the photon self-interaction term included. The term $q\psi\gamma^\mu\psi A_\mu$ reflects the interaction between a fermion and the electromagnetic force (photon) with strength q ($q=-e$) the electromagnetic interaction charge (electric charge). The mass term of the photon is not added to the lagrangian since it spoils the gauge invariance. This is in agreement with the observation that the photon is mass-less. $U(1)$ has one generator which corresponds to the photon mediator.

2.2.2.2 Electro-Weak interaction

Electroweak interaction consists of an unification of the electromagnetic and weak interactions. It is described by the combined gauge symmetry $SU(2)_T \times U(1)_Y$, where the $U(1)_Y$ symmetry mimics that of QED with the weak hypercharge Y . The $SU(2)$ represents the weak interaction with its generator vector T called weak isospin. The Lagrangian of the theory can be written as :

$$\mathcal{L}_{EW} = \bar{\psi} i\gamma^\mu \partial_\mu \psi - eY\bar{\psi}\gamma^\mu B_\mu \psi - g_W\bar{\psi}\gamma^\mu \mathbf{T} \cdot \mathbf{W}_\mu \psi - \frac{1}{4}F^{\mu\nu}F_{\mu\nu} - \frac{1}{4}W^{i\mu\nu}W_{\mu\nu}^i, \quad (2.3)$$

where g_W is the weak coupling to the fermionic fields. The first two terms are similar to \mathcal{L}_{QED} . However, the term representing the coupling of fermions to photons is replaced by more general terms: the W_μ field and the hyper-photon B_μ field. The two charged vector bosons W^\pm appear as linear combinations of the W_μ field components, $W_\mu^\pm = \frac{1}{\sqrt{2}}(W_\mu^1 \mp W_\mu^2)$. The photon is now created through the mixing of the W_μ and B_μ fields, as :

$$A_\mu = B_\mu \cos\theta_W + W_\mu^3 \sin\theta_W, \quad (2.4)$$

where θ_W is the weak mixing angle, and the Z_μ field, corresponding to the Z boson, is generated similarly as :

$$Z_\mu = -B_\mu \sin\theta_W + W_\mu^3 \cos\theta_W. \quad (2.5)$$

The field strength tensor for the weak gauge fields W^i is defined as:

$$W_{\mu\nu}^i = \partial_\mu W_\nu^i - \partial_\nu W_\mu^i - g_W \epsilon_{ijk} W_\mu^j W_\nu^k, \quad (2.6)$$

The non-Abelian nature of $SU(2)$ generates the third term in Eq.(2.6), which gives rise to the weak boson self-interactions.

The electric charge q is related to Y and T by through the Gell-Mann-Nishijima relation:

$$q = T_3 + \frac{Y}{2}, \quad (2.7)$$

where T_3 is the third component of the isospin T . Fermions are decomposed into left-handed and right-handed chirality types. The chirality is defined for mass-less particles as the same as helicity and refers to the relation between the spin and momentum direction. While for massive particles chirality is trickier to define. Note that the electroweak force interacts only with left-handed particles because interaction with right-handed particles would violate the parity. The chirality separates between left-handed doublets, and the right-handed singlets:

$$(\nu_i \ i)_L^T, i_R \ with i = e, \mu \ or \ \tau, \quad (2.8)$$

and,

$$(u \ d)_L^T, (c \ s)_L^T, (t \ b)_L^T, u_R, d_R \dots . \quad (2.9)$$

2.2.2.3 Strong interaction

Additionally to QED, the strong interaction is described by Quantum Chromo-Dynamics (QCD), which is a local gauge symmetry under $SU(3)_C$. $SU(3)$ has eight generators corresponding to the eight gluons mediators of the strong force. The expression for the locally gauge invariant Lagrangian of the QCD, which describes interactions of quarks of mass m and quark-field spinors ψ via a mass-less gluons is:

$$\mathcal{L}_{QCD} = \sum_{flavours} \bar{\psi}_a (i\gamma^\mu \partial_\mu \delta_{ab} - g_s \gamma^\mu t_{ab}^C G_\mu^C - m \delta_{ab}) \psi_b - \frac{1}{4} F_{\alpha\beta}^A F^{A\alpha\beta}, \quad (2.10)$$

where $a = 1, 2, 3$ is the color index. The G_μ^C are the gluon fields with $C = 1, 2, \dots, 8$ that transform under the adjoint representation of the $SU(3)$ group. The t_{ab}^C are the generators of the $SU(3)$ group, the quantity g_s corresponds to strong coupling constant that determines the strength of interactions between coloured particles (quarks and gluons). The strong field tensor is defined as :

$$F_{\alpha\beta}^A = \partial_\mu G_\nu^A - \partial_\nu G_\mu^A - g_s f^{ABC} G_\mu^B G_\nu^C, \quad (2.11)$$

where f^{ABC} are the structure constants of the $SU(3)$ group. In contrast to QED, the field tensor of the QCD includes the gluon triplet and quartic self-interactions. Only particles carrying colour charge (i.e. quarks) couple to these gluons. Colour charge is conserved in each interaction. Since the $SU(3)$ group is non-Abelian, the gluons themselves must also carry (anti-)colour charge and thus interact with each other.

Finally, the Standard Model Lagrangian density could be summarized as :

$$\mathcal{L}_{SM} \sim \mathcal{L}_{EW} + \mathcal{L}_{QCD}. \quad (2.12)$$

Note that, in the \mathcal{L}_{EW} no mass term is introduced for the two newly appearing bosons, while experimental observations indicate large masses. Additionally, the fermion mass term that appeared in \mathcal{L}_{QED} is now absent in \mathcal{L}_{EW} , requiring the introduction of an additional mechanism to explain the origin of their mass. This is handled through the process of Electroweak Symmetry Breaking (EWSB), and the introduction of the Higgs mechanism to generate mass.

2.3 Electroweak Symmetry Breaking (EWSB)

This section will ask the question mass of particles and introduce the EWSB to answer.

Introduce the Higgs boson and its proprieties.

The gauge bosons mass terms cannot be simply introduced as it would break gauge invariance. In 1964, Brout-Englert-Higgs (BEH) mechanism introduces a spontaneous symmetry breaking ad-hoc in the SM to preserve the local gauge invariance [4]. In the minimal model of EWSB, mass of particle can be generated by introducing the Higgs field represented by a weak iso-spin doublet of one charged and one neutral complex scalar ($J=0$) field complex scalar :

$$\phi(x) = \frac{1}{\sqrt{2}} \begin{pmatrix} \phi_+ \\ \phi_0 \end{pmatrix}. \quad (2.13)$$

Higgs lagrangian is added to the SM lagrangian as :

$$\mathcal{L}_{\text{Higgs}} = (D^\mu \phi)^\dagger (D_\mu \phi) - V(\phi), \quad (2.14)$$

where D^μ is the covariant derivative $D^\mu = (\partial_\mu + igT^i W_\mu^i + i\frac{1}{2}g'B_\mu)$. The kinetic and the interaction of the Higgs field with weak gauge bosons is described by the term $D^\mu \phi$. $V(\phi)$ is the Higgs potential:

$$V(\phi) = \mu^2 \phi^+ \phi + \lambda (\phi^+ \phi)^2, \quad (2.15)$$

the first term can be associated to the mass of the field and the second represents the quadratic self-interaction of the scalar field. The parameter λ has to be positive to obtain a potential with finite minima, while μ can be chosen freely. For $\mu^2 > 0$, the potential has a single ground state at zero with all fields being zero ($\phi_0 = 0$). Hence the vacuum expectation value of the Higgs field would be zero and the symmetry is preserved. However, for $\mu^2 < 0$ the potential has an infinite set of minima v given by :

$$\phi_0 = \langle \phi^+ \phi \rangle = \frac{v^2}{2} = -\frac{\mu^2}{2\lambda}, \quad (2.16)$$

$v \neq 0$ being the vacuum expectation value (vev) which is illustrated in Figure 2.1.

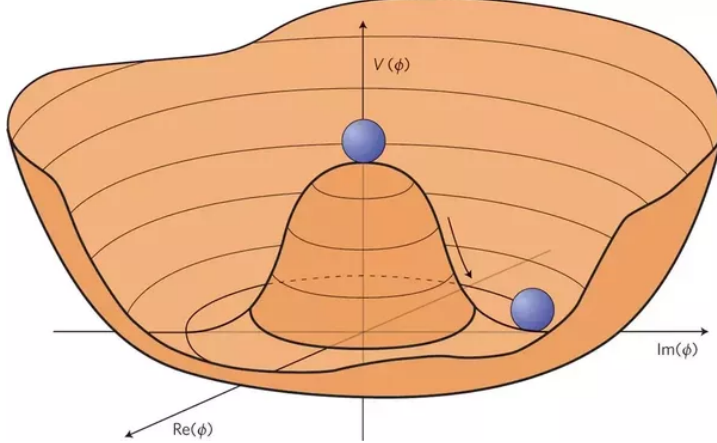


Figure 2.1: Shape of the Higgs potential for $\mu^2 < 0$ this potential has an infinite amount of minima. [5]

The choice of the physical vacuum state spontaneously breaks the Lagrangian symmetry. An expansion of ϕ_0 around its vacuum state v introduces a massive scalar and three mass-less Gladstone bosons. However,

the Goldstone bosons appear to be not physical and can be eliminated using the gauge Unitary, enforcing the Higgs doublet to be real:

$$\phi(x) = \frac{1}{\sqrt{2}} \begin{pmatrix} 0 \\ v + h(x) \end{pmatrix}, \quad (2.17)$$

where $h(x)$ is physical field linked to a new massive particle: the Higgs boson. The form of Higgs potential becomes:

$$V(\phi) = -\frac{1}{2}m_H^2 h^2(x) + \lambda_{HHH} h^3(x) + \lambda_{HHHH} h^4(x), \quad (2.18)$$

where $m_H^2 = 2\lambda^2 = 2\lambda v^2$ is the square of Higgs mass, λ_{HHH} is the coupling in a vertex with tree Higgs and λ_{HHHH} for the case of four Higgs. Accordingly, the terms giving the mass to the gauge bosons can be identified:

$$m_W = \frac{1}{2}gv \quad (2.19)$$

$$m_A = 0 \quad (2.20)$$

$$m_Z = \frac{m_W}{\cos \theta_W}. \quad (2.21)$$

The Higgs mechanism associates the degrees of freedom of hypothetical scalar (Goldstone) bosons with the longitudinal components of gauge bosons and consequently become massive. The coupling of the Higgs boson to the gauge bosons appears to be proportional to the gauge boson masses. The mass of the fermions not explained in the same way as the fermions acquire masses through the corresponding Yukawa couplings. Weak bosons masses are predicted in the SM, while Higgs boson mass is unknown and can not be constrained from other SM measurement. The Higgs mass needs to be measured, and the Higgs boson discovery is necessary to confirm the EWSB [6].

2.4 Higgs Boson Discovery

This should contains the story of Higgs boson discovery by ATLAS and CMS in 2012.

The Large Electron Positron (LEP) collider approved by the CERN Council in 1981 and commissioned eight years later, provides a detailed study of the electroweak interaction for 11 years of research. Results from LEP are used to perform stringent tests of the SM by comparing the precise results with theory predictions. LEP allows us to measure the masses of heavy fundamental particles, such as the top quark and the W boson, which are then compared to the predictions. This checks the correctness of the SM predictions. Constraining the Higgs mass is a particular interest, because this fundamental ingredient of SM has not been observed and needed to complete the SM picture. At the beginning of the LEP program no solid limit existed on the mass of the Higgs boson. The searches for the SM Higgs boson carried out by the four LEP experiments extended the sensitive range well beyond that anticipated at the beginning of the LEP program. Similarly, the Tevatron experiments CDF and D0 have excluded a range of mass $162 < m_H < 166$. Figure 2.2 shows the LEP and Tevatron exclusion limits [7, 8, 9]. A combined fit to all the data shown in 2.2 yields to the best estimated Higgs mass at that time of $m_H = 116.4^{+15.6}_{-1.3}$ GeV. This is due to the higher energy achieved and to more sophisticated detectors and analysis techniques. However, circular accelerators with electrons is limited by synchrotron radiation due to the small electron mass. Since muon acceleration is not possible at the current stage due to the short life time of muons, proton collisions represent a good way to achieve high-energy collisions needed for Higgs discovery. LEP was closed down on 2 November 2000 to make way for the construction of the Large Hadron Collider (LHC) in the same tunnel. LHC provides a nominal proton-proton collisions at a centre-of-mass energy of

\sqrt{s}) up to 14, while at the beginning of LHC the energy was 7-8 TeV and during last 4 years the maximal achieved energy is 13 TeV. LHC is detailed in a dedicated Chapter 3.

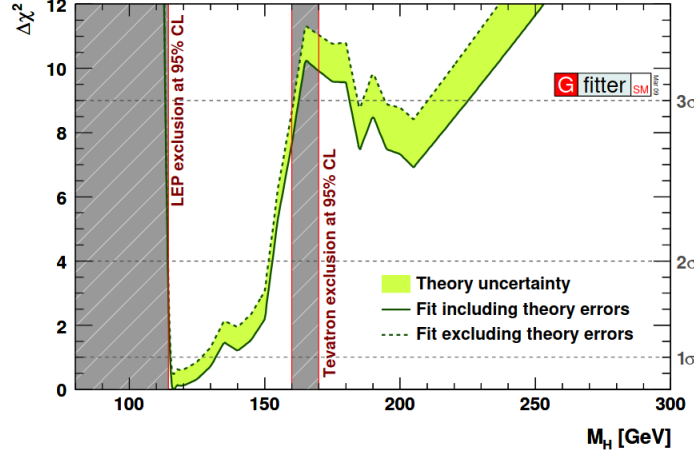


Figure 2.2: The χ^2 function for the SM as a function of the Higgs mass, LEP and Tevatron exclusions limits are shown.

2.4.1 p-p collisions

The protons protons collision and the Higgs boson cross section at 8 TeV and 13 TeV.

Protons are fermions known to be made up of two up and one down quarks (uud) called valence quarks. They interact between each other through the strong force via gluon exchange. Due to nature of QCD (non-abelian) gluons can fluctuate into quark anti-quark pairs forming the so-called sea quarks. Effectively, a proton is therefore a bound state of quarks and gluons called partons each carries a fraction x of the total proton momentum. At LHC process are produced by colliding mainly protons beams, similarly Higgs boson processes are in p-p collision.

$$p_1 + p_2 \rightarrow h. \quad (2.22)$$

The probability for a process to occur is expressed in terms of its cross section, and the dynamics of its products is determined by the dynamics of partons involved in the collision. The hard scattering cross section for such process is given by :

$$d\sigma^{p_1 p_2 \rightarrow h} = \int_0^1 dx_1 \int_0^1 dx_2 \sum_{a,b} f_{a/p_1}(x_1, \mu_F^2) f_{b/p_2}(x_2, \mu_F^2) d\hat{\sigma}^{ab \rightarrow h}(x_1, x_2, \mu_F^2), \quad (2.23)$$

where a, b are the partons involved in the process and $f_{n/p_i}(x_i)$ is the parton distribution function (PDF), which is the probability to find a parton of type n inside proton p_i with a longitudinal momentum fraction x_i at energy scale Q . $\sigma^{ab \rightarrow h}$ is the parton cross section of the process.

In general, the x dependence at a given Q^2 cannot be calculated analytically but rather are extracted from global fits to data from many experiments. There are different PDF sets which use different fitting methods and experimental data [10]. Figure 2.3 shows two examples of CT14 PDFs at given Q^2 computed using use of data from LHC experiments, and the new D\O charged lepton rapidity asymmetry data [11].

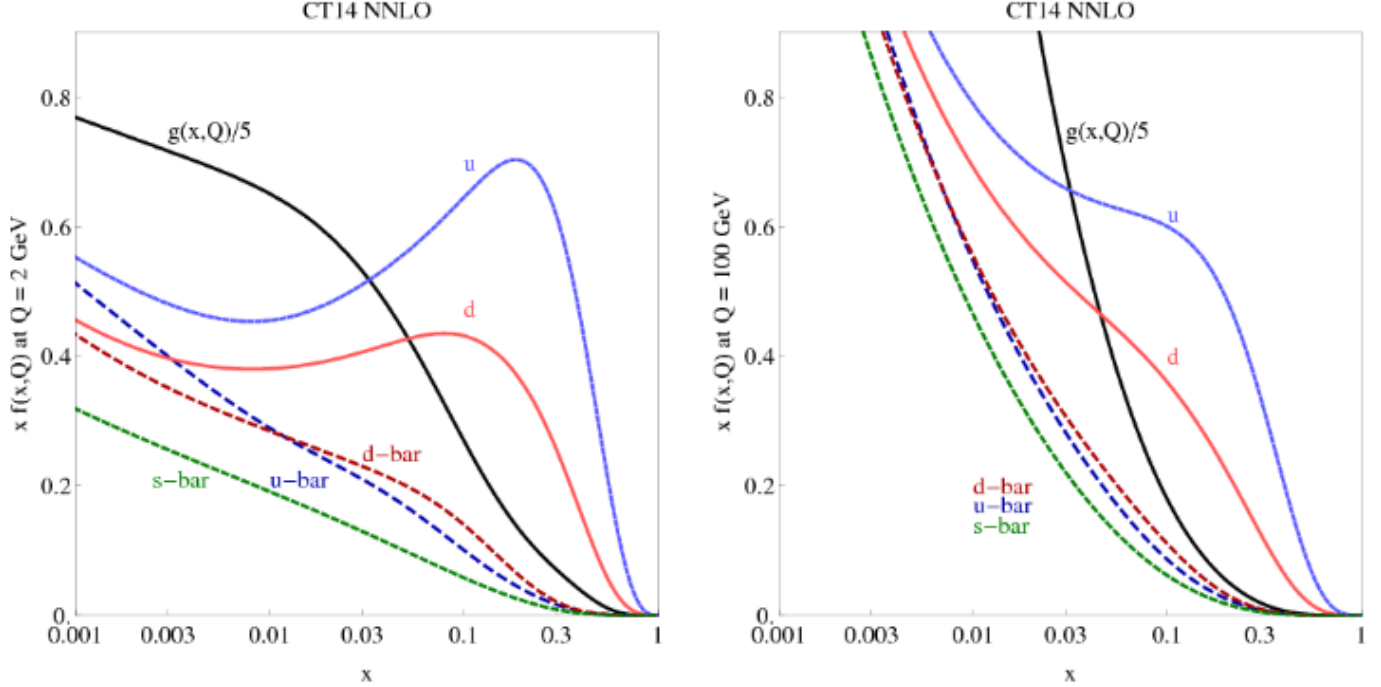


Figure 2.3: The CT14 PDFs at $Q=2$ GeV (left) and $Q = 100$ GeV (right) for different partons. These PDFs are computed at next-to-next-to-leading order.

The production of the Higgs boson at the LHC occurs in different modes. Their cross sections depend on the coupling of the Higgs boson to specific particles, but also essentially on the PDFs described above.

2.4.2 Higgs boson production

Higgs boson production modes ggF VBF VH and qqH.

The main process contributing to the Higgs boson production at LHC are represented by their leading Feynman diagrams in Figure 2.4. In the 7-13 TeV center of mass range, the most important Higgs production mode occurs via fusion of gluons (ggF).

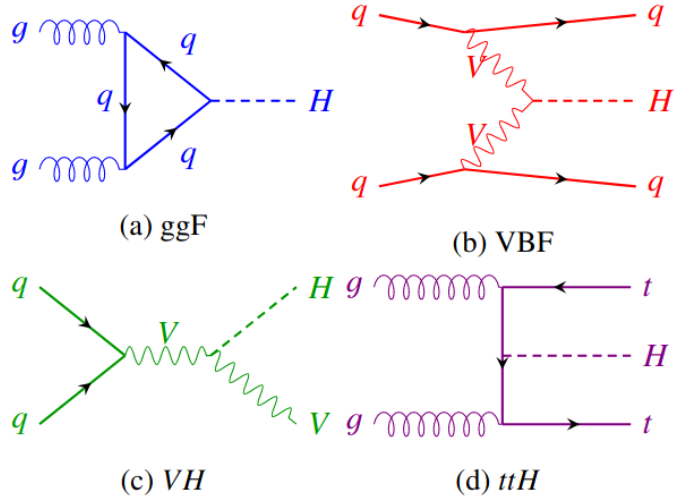


Figure 2.4: Feynman diagrams for the main production modes of Higgs boson.

In order of decreasing cross section as shown in Figure 2.5, the Higgs boson production modes are:

- gluons-gluons fusion (ggF) : the main Higgs boson production at LHC over the whole mass spectrum. The process involves the fusion of two incoming gluons that give rise to the Higgs boson through a heavy quark loop, whose main contribution comes from the top quark. The corresponding feynman diagram is shown in Figure 2.4 (a).
- Vector Boson Fusion (VBF) : each of the two interacting quarks emit a W or Z boson which, in turn, interact to produce the Higgs boson, as shown in figure 2.4 (b). Quarks deriving from the incoming partons after the emission of vector bosons proceed in the forward direction and represent the peculiar signature of this production mode, two high energy forward jets separated by a large pseudo-rapidity gap, a $\Delta\eta$ region with reduced particle density. This process has a cross section which is one order of magnitude lower than ggF for a large range of Higgs boson mass (m_H) values and it becomes comparable to ggF only for masses of the order of 1 TeV as shown in Figure 2.5 (b).
- Vector boson associated production (VH) : also known as Higgs strahlung, this process is characterized by the emission of a Higgs boson from a W^\pm or Z boson produced by two incoming quarks, as shown in figure 2.4 (c). The VH cross section is several orders of magnitude lower than the ggF and VBF cross sections for m_H larger than about 300 GeV, while the VH and VBF cross sections are comparable around $m_H = 125$ GeV as shown Figure 2.5 (b).
- Top quark associated production ($t\bar{t}H$) : a pair of top quarks, originated from the splitting of two incoming gluons, interacts to give rise to a Higgs boson, as shown in figure 2.4 (d). the production in association with a pair of top quarks allows a direct measurement of the Higgs boson coupling to the top quark. Another production mechanism analogous to the $t\bar{t}H$ process and with a similar cross section is the b-quark associated production.

The SM Higgs boson production cross section for the various production modes depends on the Higgs boson mass and on the center-of-mass energy, as shown in Figure 2.5.

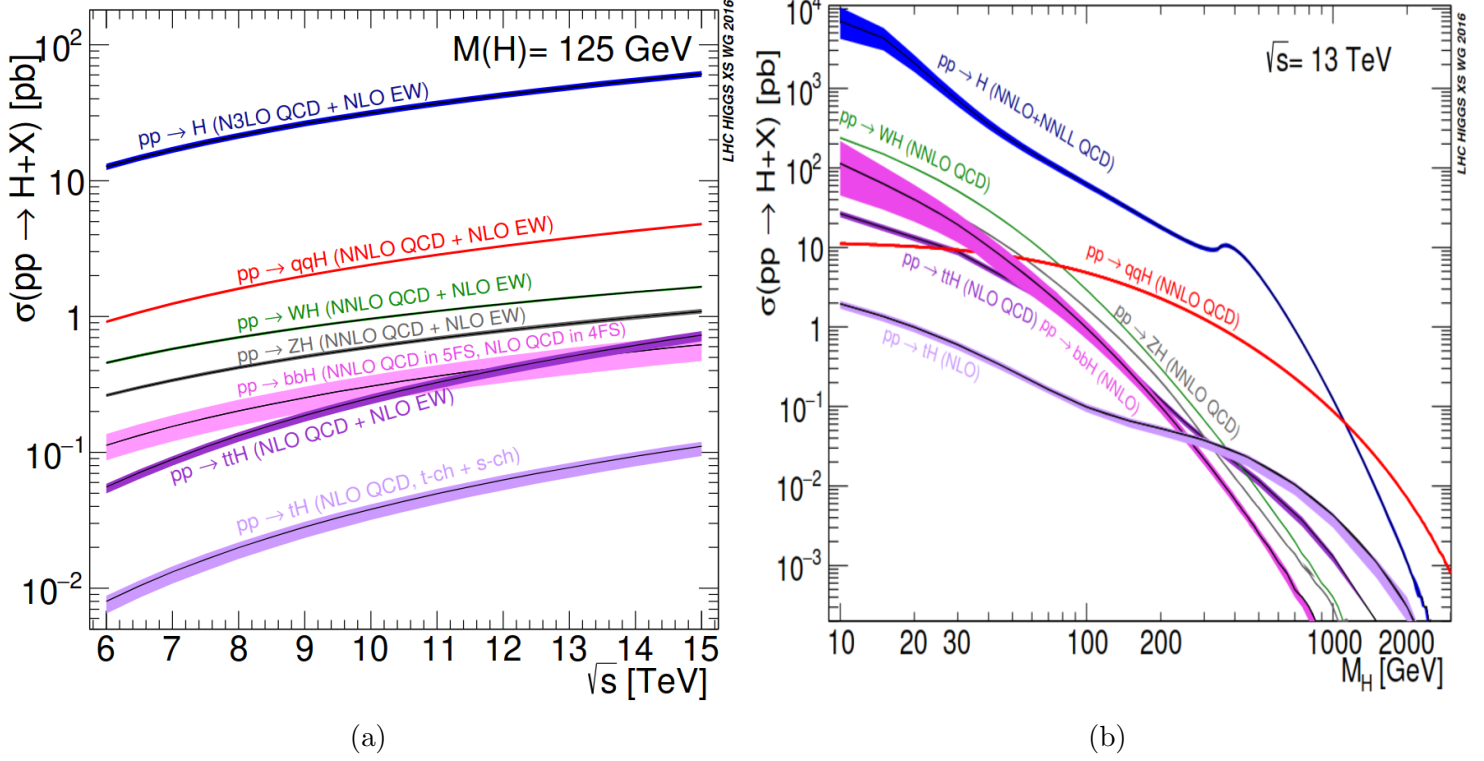


Figure 2.5: Cross sections for different Higgs boson production modes at a proton-proton collider with a centre-of-mass energy of 6-15 TeV (a). A Higgs mass of 125 GeV is assumed in this plot. Additionally, cross sections as a function of Higgs mass are shown (b) [12].

Higgs boson is an unstable particle as shown in Figure 2.6, note that the probability to decay within a given time "decay width" Γ is linked to the lifetime τ by $\Gamma\tau = \hbar$ where \hbar is the reduced Planck constant. In order to identify Higgs and its production modes, it is reconstructed from its products for a chosen decay channel.

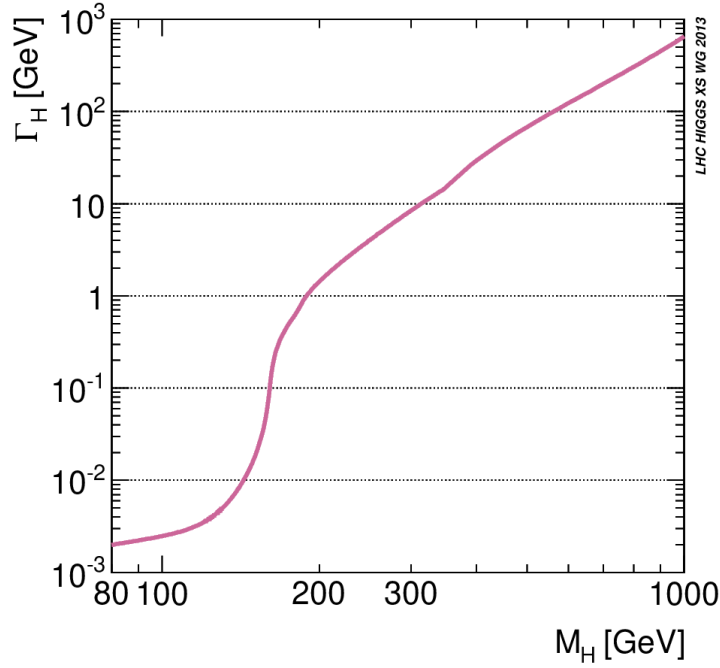


Figure 2.6: Higgs boson total decay width as a function of Higgs mass [13].

2.4.3 Higgs boson decay channels

Higgs boson decay modes and their rates.

The possible SM Higgs boson decay modes are very dependant on the Higgs boson mass as shown in figure 2.7 for a Higgs boson mass range of 80 to 200 GeV. If the Higgs boson were heavy enough to decay into two real vector bosons, the modes $H \rightarrow WW^*$ and $H \rightarrow ZZ^*$ would have dominated the decay with small contribution from Higgs to di-top quarks. At very low masses of the Higgs boson, decays into vector boson or $t\bar{t}$ would have played almost no role and the dominant decay mode would have been the experimental challenging decay mode $H \rightarrow b\bar{b}$. Since photons are mass-less particles, the direct coupling of the Higgs

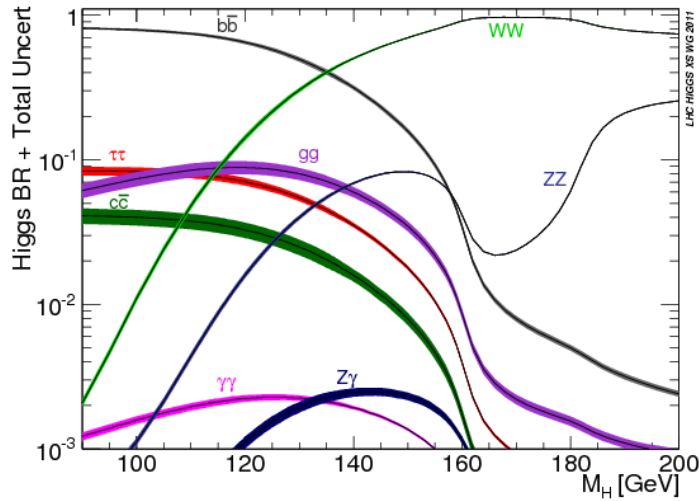


Figure 2.7: Higgs boson branching ratio of the possible Higgs decay channels as a function of the Higgs mass [14]

boson to photons is zero in the SM. However, the Higgs boson can decay into a pair of photons via loop processes. The main Feynman diagrams of this decay are shown in Figure 2.8. At a Higgs boson mass of 125 GeV, the dominant decay of the Higgs boson is $H \rightarrow b\bar{b}$ with a branching ratio of roughly 58%. At the same mass $H \rightarrow \gamma\gamma$ branching ratio is around 0.23% [15].

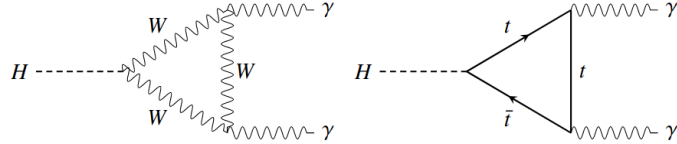


Figure 2.8: Feynman diagrams of the $H \rightarrow \gamma\gamma$ decay. Other particles can also propagate in the loop.

2.4.4 Higgs measurements

The discovery of Higgs boson in 2012 by ATLAS and CMS and first measurements of its mass. Recap of Higgs boson properties. and Introduction to self couplings no yet measured.

ATLAS and CMS collaborations, the two largest experiments of the LHC, announced on 4 July 2012 the identification with 99.99997% (5σ) of a new boson within a mass range of $125 - 127\text{GeV}$ [16, 17]. The new boson consistent the Standard Model Higgs boson properties. Later, was confirmed that the new particle, without doubt, corresponds to the Higgs boson. Higgs boson predicted in 1964, but the world had to wait until 2012 before its discovery by physicists at CERN. The Evidence of the new boson was present in the three bosonic decay modes $H \rightarrow ZZ^* \rightarrow 4l$, $H \rightarrow \gamma\gamma$ and $H \rightarrow WW^* \rightarrow l\nu l\nu$. The branching ratio of Higgs in the di-photon decay channel is small. Despite the comparably low branching fraction of this decay mode, their construction of two photons has a clean signature in the detector and allows a good energy resolution. This signal can therefore well be separated from the dominating continuum di-photon background from QCD jets, which has a smooth and well parametrisable shape. Which makes the expected Higgs boson signal significance in this decay mode is one of the highest among all the decay modes in the mass range $110 < m_H < 150\text{GeV}$. Events in data collected in 2010 and 2011 with centre-of-mass energy $\sqrt{s} = 7\text{TeV}$ and 8TeV respectively containing di-photons are combined to make the evidence of Higgs boson. Figure 2.9 shows the weighted distribution of the invariant mass of photon pairs measured by ATLAS experiments. The distributions are obtained by summing the invariant mass distributions of all of the selected events, with each event being weighted by S/B where S and B are the number of signal and background events, respectively. Figure 2.9 demonstrates a statistically significant excess of events near 125 GeV.

Measurement of the three channels are combined to confirm the observation of the new particle. The observed local significance reaches 6σ (the observed signal is $\sim 10^{-9}$ to be a background fluctuation) around 125 GeV making the first observation of Higgs boson, Figure 2.10.

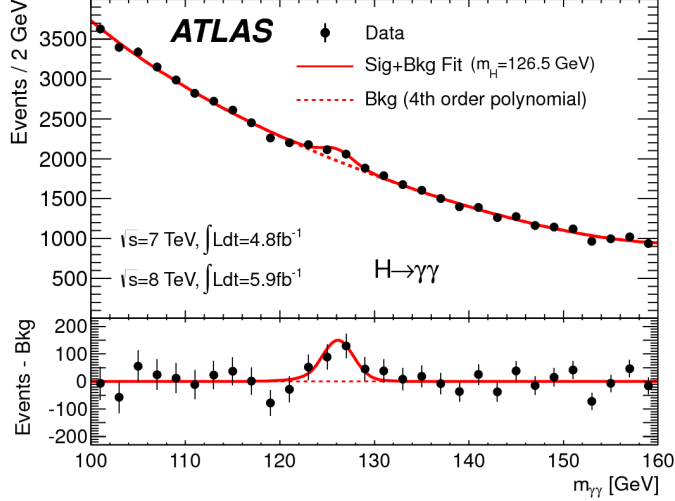


Figure 2.9: Weighted distributions of the invariant mass of di-photon [16].

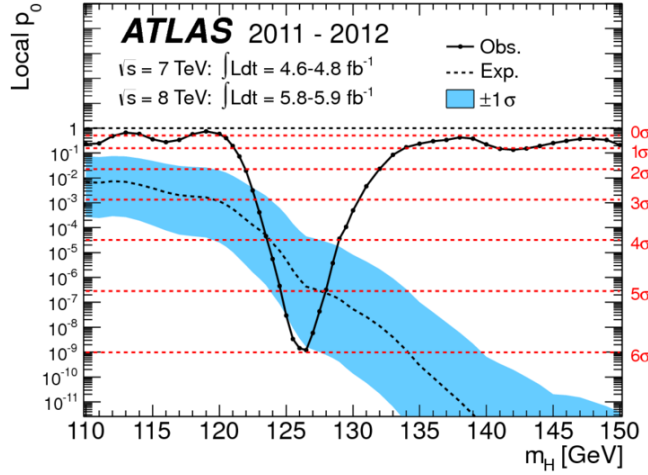


Figure 2.10: The observed local p-value as a function of m_H (solid line) and the expectation with its $\pm 1\sigma$ band assuming the presence of a Standard Model Higgs boson at that mass (dashed line) from the combination of the ZZ^* , $\gamma\gamma$ and WW^* channels by the ATLAS experiment. The horizontal dashed lines indicate the p-values corresponding to significances of 1 to 6σ [16].

The latest measurement of Higgs boson using the data collected during 2015-2018 corresponding to $139 fb^{-1}$ yields to a mass of $m_H = 125.09 \pm 0.24$ GeV [18]. Figure 2.11 shows the in the di-photon invariant mass distribution. Figure 2.12 shows the best-fit values of the production cross-sections times branching fraction in different channel to the Standard Model value with the $139 fb^{-1}$ data.

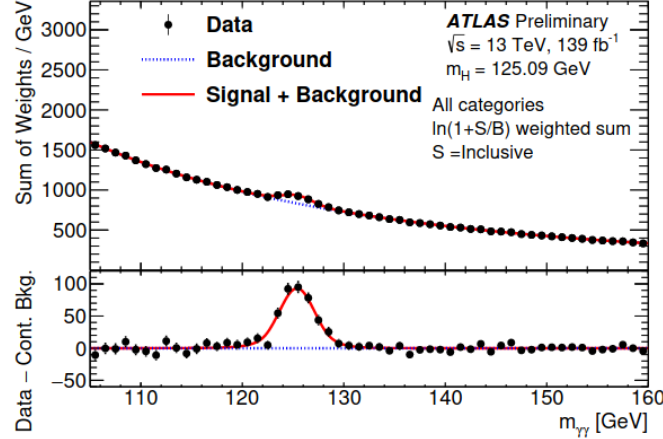


Figure 2.11: The inclusive diphoton invariant mass distribution [19].

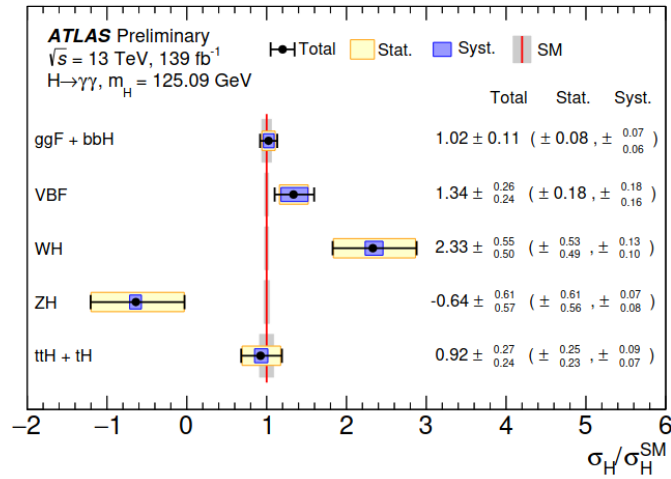


Figure 2.12: Cross sections times branching fraction for $ggF + b\bar{b}H$, VBF , VH and $t\bar{t}H + tH$ production, normalized to their SM predictions [19].

Finally, by the observation of Higgs boson the last piece of the standard model of elementary particles is was fund. SM particles are summarized in Figure 2.13.

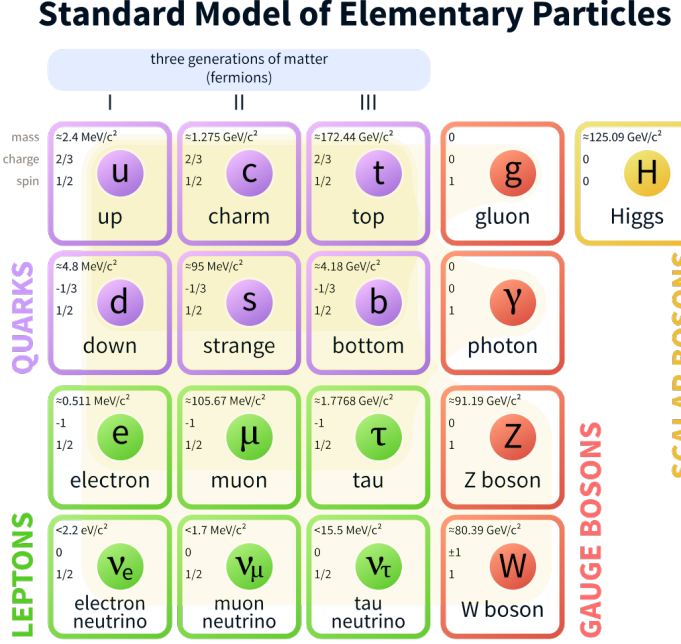


Figure 2.13: The particle content of the Standard Model (SM).

Understanding the properties and couplings of the last piece of SM is a priority of both ATLAS and CMS. Higgs self-couplings λ_{HHH} is vital, providing a direct probe on the EWSB and is a precision test of the electroweak theory. A direct probe of the trilinear coupling is possible through studying Higgs pair production where two Higgs bosons are produced in the same event, making di-Higgs analyses particularly interesting and the main subject of the thesis.

2.5 Double Higgs boson

This should contain the theory of HH and how it allows to measure the higgs self couplings.

Double Higgs production (HH) presents the only direct measurement of the Higgs self-coupling. Confirming the existence and amplitude of the Higgs Self-coupling is one of the main key prediction of the SM not observed yet. In particular, the measurement of the Higgs boson self-coupling λ (also referred to as the Higgs boson tri-linear coupling λ_{HHH}) is of great importance as expected to yield a deeper understanding of particle physics and cosmology. This measurement makes it possible to experimentally reconstruct the Higgs potential and check whether the Higgs boson discovered in 2012 at CERN is the one predicted by the Brout-Englert-Higgs mechanism. The di-Higgs production rate gives a handle to more accurately measure the Higgs potential. The main goal of this thesis is the search of Higgs boson pair production.

2.5.1 Di-Higgs production and decays

This should contain the production modes and decays of HH. and the $HH \rightarrow \gamma\gamma\bar{b}b$ channel.

As the SM provides the trilinear coupling of the Higgs boson, all SM Higgs boson production mode are known for di-Higgs production. Similarly to single Higgs boson, HH production is dominated by gluon-gluon fusion (ggF) through the destructive interference of two LO Feynman diagrams, shown in Figure 2.14, involving top-quark loops and the triple Higgs self-coupling. In the box diagram, the top-quark

Yukawa coupling λ_t is present in two vertices so the contribution of this diagram to the amplitude is proportional to λ_t^2 , while in the triangle diagram there is λ_t in one vertex and the triple Higgs self-coupling λ_{HHH} in the other vertex and the contribution of this diagram is proportional to $\lambda_t \cdot \lambda_{HHH}$. The amplitude of the process can be written as :

$$A(\lambda_t, \lambda_{HHH}) \equiv \lambda_t^2 \cdot \square + \lambda_t \cdot \lambda_{HHH} \triangle, \quad (2.24)$$

where \square represents the contribution of the box diagram and \triangle the one of the triangle diagram.

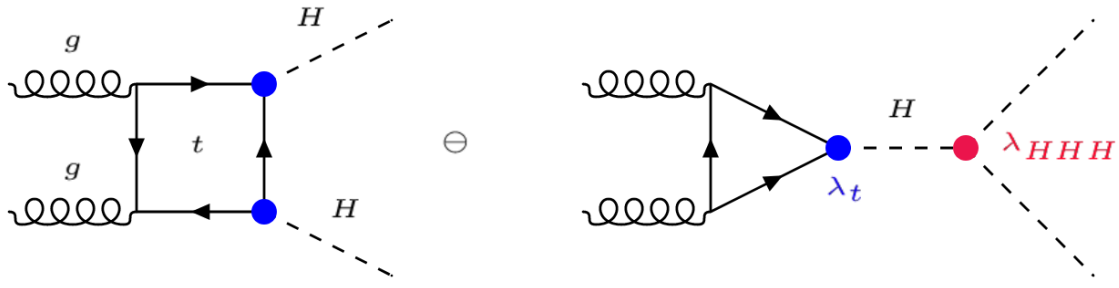


Figure 2.14: Leading Order (LO) Feynman diagrams contributing to ggF Higgs boson pair production through a top-quark loop (box) and through the triple self-coupling of the Higgs boson (triangle).

The SM cross section for Higgs boson pair production via ggF at $\sqrt{s} = 13$ TeV, calculated at Next-to-Next-to-Leading Order (NNLO) [20, 21], is:

$$\sigma_{HH}^{NNLO} = 33.53^{+4.3\%}_{-6.0\%} \text{ fb}, \quad (2.25)$$

three orders of magnitude smaller than the single Higgs production cross section. This accounts for more than 90% of the total Higgs boson pair production cross section. VBF mode also contributes to the di-Higgs production with a very low cross section (two orders of magnitude smaller). Therefore only the ggF production mode is considered in this thesis. Figure 2.15 shows the other production modes contributing to Higgs pair production. The corresponding cross section as a function of centre-of-mass energy is shown Figure 2.16.

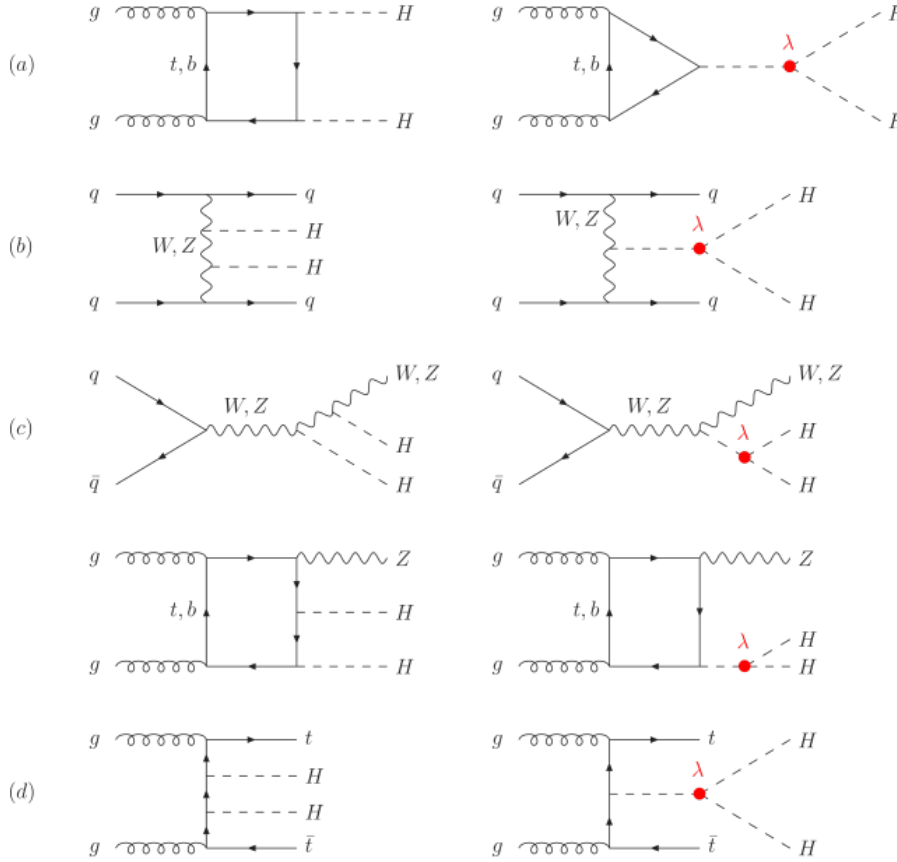


Figure 2.15: HH production modes, in decreasing order of cross section. λ refers to Higgs tri-linear coupling: (a) ggF mode, (b) VBF mode, (c) Vector boson association (VH) and (d) top associated production.

Figure 2.17 presents the matrix of the decay channels of Higgs boson pair resulting from all possible combination of decays of the two Higgs bosons. The dominant channels are $HH \rightarrow b\bar{b}b\bar{b}$, $HH \rightarrow b\bar{b}\tau\tau$ and $HH \rightarrow b\bar{b}WW^*$.

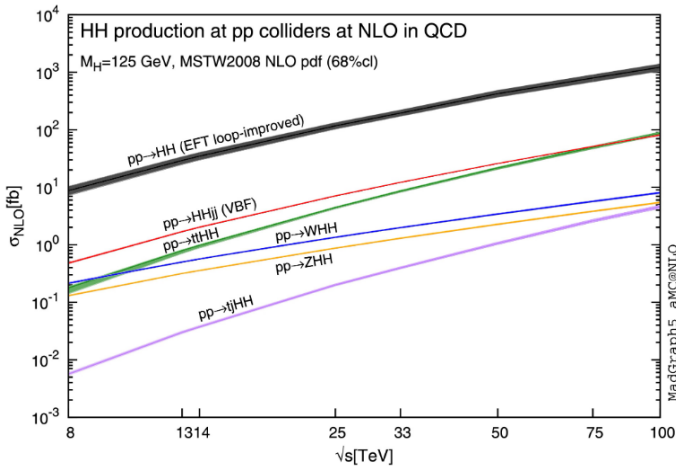


Figure 2.16: Total cross sections at the NLO for HH production as a function of centre-of-mass energy. Assuming κ_λ and κ_t equals to their SM values.

	bb	WW	$\tau\tau$	ZZ	$\gamma\gamma$
bb	33%				
WW	25%	4.6%			
$\tau\tau$	7.4%	2.5%	0.39%		
ZZ	3.1%	1.2%	0.34%	0.076%	
$\gamma\gamma$	0.26%	0.10%	0.029%	0.013%	0.0005%

Figure 2.17: Di-Higgs system decay branching ratios assuming SM Higgs bosons with $m_H = 125.09$ GeV.

Even if there are other channels with branching ratios higher by one or two orders of magnitude, $b\bar{b}\gamma\gamma$ final state is one of the most promising decay channels for the search for di-Higgs production as it has a good compromise between the very large branching ratio from $H \rightarrow b\bar{b}$ decay and the small Higgs to diphoton branching ratio. The $\gamma\gamma b\bar{b}$ channel is appealing thanks to an excellent diphoton resolution leads on a clean di-photon signature giving a narrow peak at Higgs mass in the $m_{\gamma\gamma}$ invariant mass spectrum on top of a smoothly falling background. These helps in separating the signal from the background processes comparing to other channels such $bbbb$, $b\bar{b}WW$ and $b\bar{b}\tau\tau$. This thesis is preformed on $\gamma\gamma b\bar{b}$ final state.

2.5.2 Di-Higgs as a probe of BSM physics

How κ_λ cloud probe the existence of BSM effects

The small cross section (Eq. 2.25) is challenging to measure. If SM expectations hold, the production of a Higgs boson pair in a single pp interaction should not be observable with the currently available LHC data set, unless its cross section is enhanced by an anomalous (new physics). Which makes HH production a promising process to probe new physics beyond the standard model (BSM). Beyond the Standard-Model (BSM) scenarios may enhance the Higgs boson pair production rate and would be indicating a new physics. Many of those BSM theories predict the existence of heavy particles that can decay into a pair of Higgs bosons. These could be identified as a resonance in the di-Higgs invariant mass spectrum. In addition to the resonant production, there can also be non-resonant scenarios which can bring substantial enhancement of the cross section by modifying the relative sign of Δ and \square , and by increasing the Δ which is proportional to κ_λ . Only the non-resonance search is considered in this thesis. These can either originate from loop corrections involving new particles, such a light colored scalars, or through non-SM couplings. Anomalous couplings of Higgs boson with the top-quark or triple Higgs self-coupling can either be extensions to the SM, such as contact interactions between two top quarks and two Higgs bosons, or be deviation from the SM values of the trilinear Higgs coupling. Considering possible modifications of them, the deviation is quantified by $\kappa_\lambda = \frac{\lambda_{HHH}}{\lambda_{HHH}^{SM}}$ and $\kappa_t = \frac{\lambda_t}{\lambda_t^{SM}}$, where λ_i is the coupling i of the new physics and λ_i^{SM} its SM value.

Given the κ_t and κ_λ modifiers, the Higgs pair production cross section can be parameterised as :

$$\sigma \approx k_t^4 \left[|\square|^2 + \frac{k_\lambda}{k_t} (\square \Delta + \Delta \square) + \left(\frac{k_\lambda}{k_t} \right)^2 |\Delta|^2 \right], \quad (2.26)$$

this shows that the production cross section depends on both parameters κ_t and κ_λ , while the kinematics only depends on their ratio, that modifies the relative contribution of the two diagrams and thus the shape of the kinematic distributions. The maximum interference between the two diagrams corresponds to the cross section minimum located at $\kappa_\lambda = 2.4\kappa_t$. Figure 2.18 shows an illustration of diagram contribution to the invariant mass distribution of di-Higgs system m_{HH} . The box diagram has an invariant mass spectrum peaking around $2m_t$. When including the triangle diagram with the triple Higgs self-coupling, the invariant mass spectrum becomes generally softer with the increase of its contribution. This effect cause a large change in m_{HH} distribution as shown in Figure 2.19.

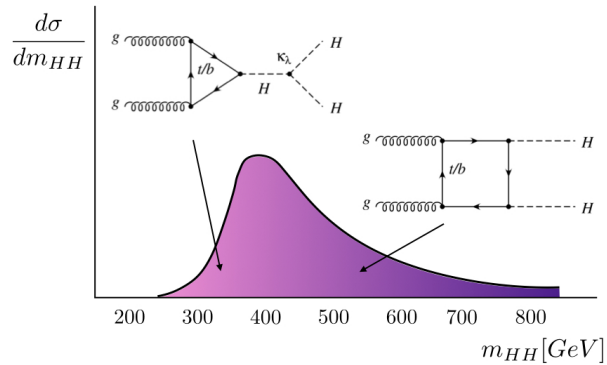


Figure 2.18: Illustration of both box and triangle diagrams contribution to di-Higgs invariant mass spectrum.

The interference of the two diagrams also generates local minima in the differential cross section around $m_{HH} = 2m_t$ for the case of $\kappa_\lambda = 2$.

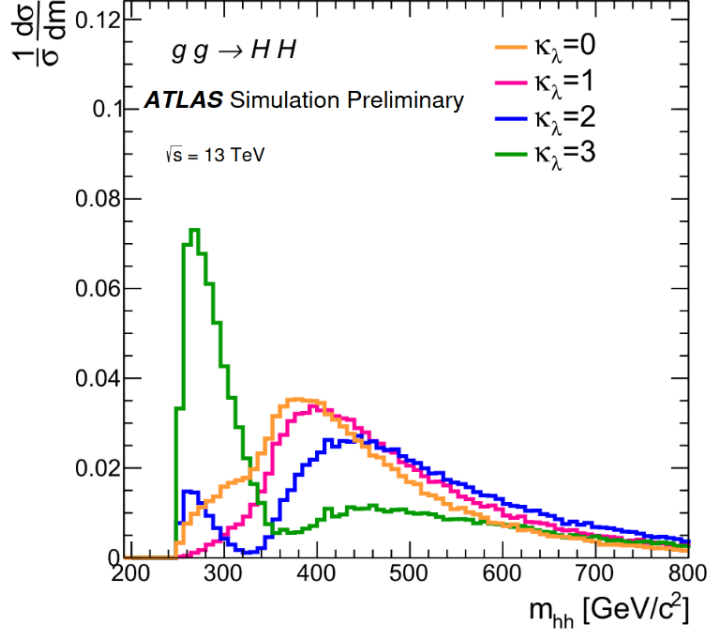


Figure 2.19: Higgs pair invariant-mass distribution in ggF for various values of κ_λ assuming $\kappa_t = 1$.

Figure 2.20 displays total LO and NLO cross sections for the six dominant HH production channels at the LHC with $\sqrt{s} = 14$ TeV, as a function of the self-interaction coupling κ_λ . As mentioned above, Higgs pair production is a promising process to probe new BSM physics. In this thesis, in addition to searching for the SM Higgs pair production process, constrain on κ_λ is also extracted.

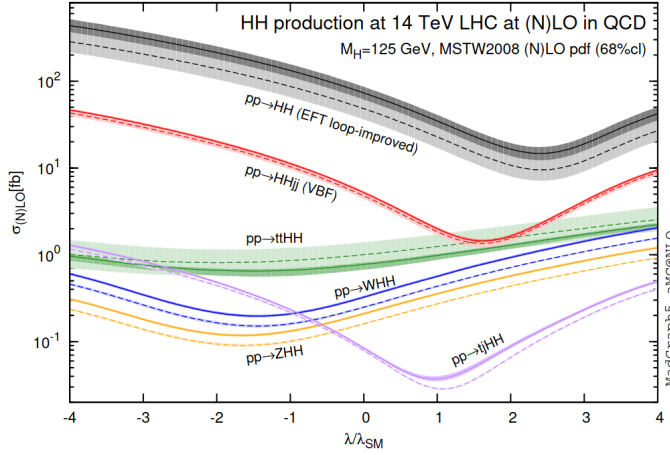


Figure 2.20: Total LO and NLO cross sections for HH production at the LHC with $\sqrt{s} = 14$ TeV, as a function of the self-interaction coupling κ_λ .

2.5.3 Current Measurements

This includes the 36 fb^{-1} results and the limit on HH cross section and κ_λ .

At the beginning of this thesis (2018), the latest measurement of Higgs pair production in $HH \rightarrow \gamma\gamma\bar{b}b$ channel was preformed with an amount of data of 36.1 fb^{-1} representing the data collected by ATLAS detector in 2015 and 2016 (Chapter 3 is dedicated to ATLAS detector). Results of the previous analysis

were consistent with the SM expectations [22]. In the non-resonant case, results are interpreted in the context of κ_λ . The analysis set an observed (expected) 95% CL upper limit on HH cross section of 0.73 (0.93) pb, corresponding to 22 (28) times the predicted SM value. The Higgs self coupling is constrained to be between $-8.2 < \kappa_\lambda < 13.2$ at 95% CL ($-8.3 < \kappa_\lambda < 13.2$ expected), other SM parameters are fixed to their expected value when extracting limits. The limit scan of κ_λ is shown in Figure 2.21.

	Observed	Expected	-1σ	$+1\sigma$
$\sigma_{gg \rightarrow HH}$ [pb]	0.73	0.93	0.66	1.3
As a multiple of σ_{SM}	22	28	20	40

Table 2.2: The 95% CL observed and expected limits on the Higgs boson pair cross-section in pb and as a multiple of the SM production cross-section. The $\pm 1\sigma$ band around each 95% CL limit is also indicated.

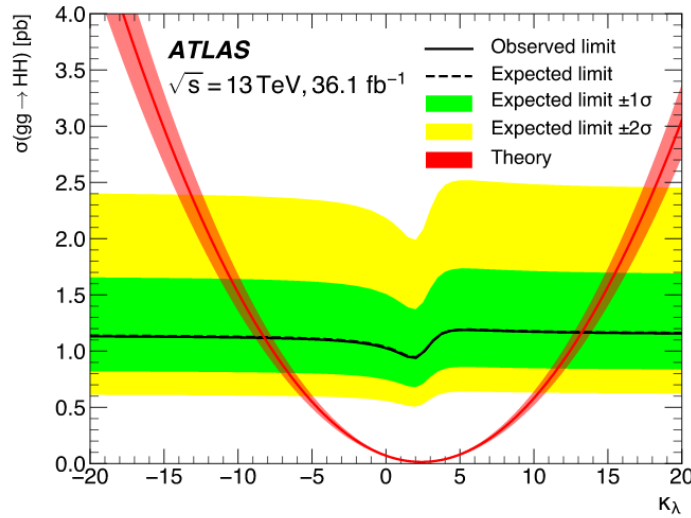


Figure 2.21: The expected and observed 95% CL limits on the non-resonant production cross section $\sigma_{gg \rightarrow HH}$ as a function of κ_λ . The red line indicates the predicted HH cross section if κ_λ is varied but all other couplings remain at their SM values. The red band indicates the theoretical uncertainty of this prediction.

Additionally to $HH \rightarrow \gamma\gamma b\bar{b}$ results, a combination of other decay modes is performed to better constrain the Higgs self coupling [23]. Figure 2.22 shows the upper limits on the cross section $\sigma_{gg \rightarrow HH}$ normalised to its SM expectation. The sensitivity of the SM HH search is driven by the final states $b\bar{b}b\bar{b}$, $b\bar{b}\tau\tau$ and $b\bar{b}\gamma\gamma$. The Extracted limit on the κ_λ is shown in Figure 2.23. The combination results are summarized in Table 2.3.

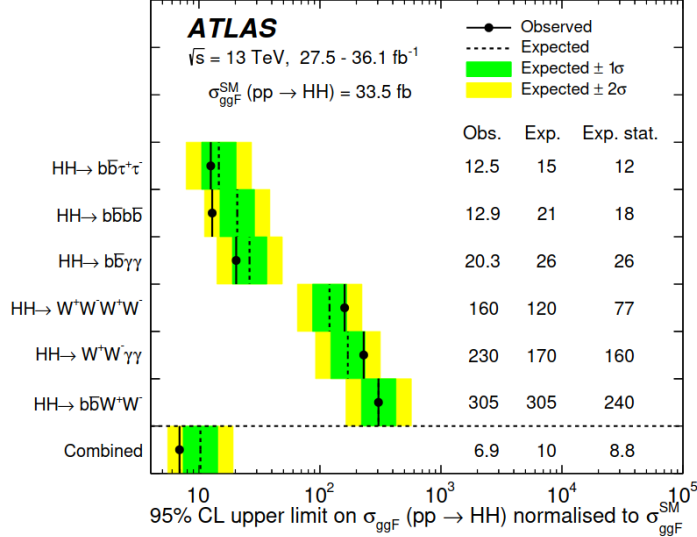


Figure 2.22: Upper limits at 95% CL on the cross-section of the ggF SM HH production normalized to its SM expectation $\sigma_{gg \rightarrow HH}^{SM}$ from the $b\bar{b}\tau\tau$ [24], $b\bar{b}b\bar{b}$ [25], $b\bar{b}\gamma\gamma$ [22], $WWWW$ [26], $WW\gamma\gamma$ [27] and $b\bar{b}WW$ [28] searches, and their statistical combination.

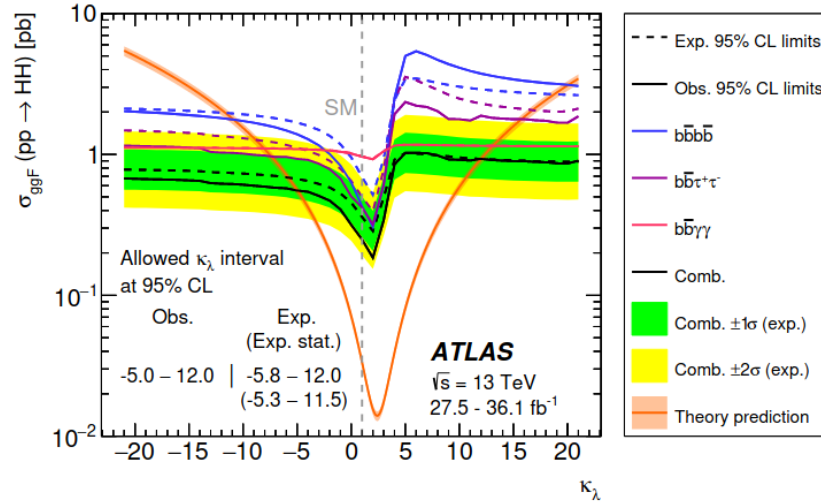


Figure 2.23: Upper limits at 95% CL on the cross-section of the ggF non-resonant as a function of κ_λ .

	Observed	Expected
$\sigma_{gg \rightarrow HH}/\sigma_{gg \rightarrow HH}^{SM}$	6.9	10
Allowed κ_λ interval	[-5,12]	[-5.8,12.0]

Table 2.3: The 95% CL observed and expected limits on the Higgs boson pair cross-section normalized to the SM production cross-section and the allowed κ_λ interval.

Contributing to the $HH \rightarrow \gamma\gamma b\bar{b}$ non-resonant analysis involves $139 fb^{-1}$ of data collected during the Run 2 (2015-2018) of the LHC program, and improve the current limits on the cross-section and self-coupling is the aim of this thesis.

2.6 Effective Field Theory (EFT)

A brief introduction to EFT and how it helps to probe physics at large scale.

In the context of search for BSM physics, so far, no indication has been found at the LHC. This could be explained by the fact that the new physics is not accessible at the LHC. Effective Field Theories (EFTs) provide an approach to probe the existence of BSM physics in a model independent way at the LHC, even if the new physics scale Λ is not directly accessible at the LHC. When BSM resides at scales larger than the EW scale ($\Lambda \gg vev$), the new physics decouples from the SM and no light hidden states are produced. When this condition is satisfied, an expansion of the Lagrangian is canonical dimensions of $\frac{vev}{\lambda}$ can be performed. The theory that results is the Standard Model Effective Field Theory (SMEFT) [29]. The SMEFT is well defined and has been studied with increased theoretical sophistication in recent years, and it can capture a wide range of possible extensions of the SM. Such SM extensions can address the strong evidence for dark matter and neutrino masses not covered by SM. A linear EFT model of SMEFT is considered in this thesis :

$$\mathcal{L}_{SMEFT} = \mathcal{L}_{SM} + \mathcal{L}^5 + \mathcal{L}^6 + \mathcal{L}^7 + \dots, \quad \mathcal{L}^d = \sum_{i=1}^{n_d} \frac{C_i^d}{\Lambda^{d-4}} Q_i^d \quad \text{for } d > 4. \quad (2.27)$$

The number of non-redundant operators in \mathcal{L}^i is known. The operators Q_i^d are suppressed by $d-4$ powers of the cutoff scale Λ . These operators build a complete set of all operators allowed by the SM gauge symmetries. The Warsaw basis is used for the invariant operators Q_i^d [30]. The coefficients C_i^d are called Wilson coefficients. They are free parameters of the theory.

The new physics interferes with the standard model, and modify the kinematics of the given process. The cross section of a specific process within the SMEFT can be splitted as :

$$\sigma = \sigma_{SM} + \sigma_{int} + \sigma_{BSM}, \quad (2.28)$$

where σ_{SM} is the SM cross section, σ_{int} represents the interference between the BSM physics with the SM, and σ_{BSM} is a pure BSM physics suppressed by Λ^{-4} that does not depend on the SM amplitude; it can however become important in specific regions of the phase space and its consideration can prevent negative cross sections.

Projecting measurements of the interactions of the known Standard Model (SM) states into an effective field theory (EFT) framework is an important goal of the LHC physics program [31]. The interpretation of measurements of the properties of the Higgs boson in an EFT allows one to consistently study the properties of this state. Similarly to κ_λ variations, new physics can affect Higgs pair production. Higgs pair production results can benefit from an interpretation beyond the κ_λ variations. The full Run 2 di-Higgs results can be used to set limits on SMEFT parameters. Detailed studies of EFT within double Higgs context are described in the dedicated Chapter **To Be Added**.

2.7 Conclusion

Brief conclusion of chapter 1.

Higgs mechanism was introduced into the SM to explain the origin of the masses of the particles. A particle with similar proprieties to SM Higgs boson was discovered at collisions of LHC in 2012. After its discovery, a priority of the ATLAS and CMS collaborations has been to better understand its properties and couplings. Understanding Higgs self-coupling is vital providing a direct probe on electroweak symmetry

breaking (EWSB) and reconstruct the Higgs potential to check whether the boson discovered is Higgs boson. The theoretical backgrounds needed to understand the main subject of the thesis are introduced. As well as the current results with 2015-2016 data. The EFT is highlighted as an interpretation of di-Higgs results beyond κ_λ . Next chapter focus on the experimental setup to produce and collect data, the Large Hadron Collider and the ATLAS detector.

The Large Hadron Collider and the ATLAS detector

This chapter will include :

- LHC description and how it works
- different LHC points
- focus on ATLAS as main experiment
- focus on EM and H calorimeters

Copy past from other thesis!

The physics described in this thesis exclusively uses data collected by the ATLAS (A Toroidal LHC Apparatus) detector collected from high-energy proton-proton collisions, accelerated and been collided by the Large Hadron Collider (LHC). In terms of achievable centre-of-mass energy, LHC is currently the most powerful particle accelerator. The structure, parameters and principles of LHC and ATLAS, besides the complex sub-detecting system is introduced in this chapter.

3.1 The Large Hadron Collider

LHC is a circular collider of hadrons with a circumference of 27 kilometers. It was designed to accelerate and collide proton beams with a centre-of-mass energy up to 14 TeV as well as heavy ions, in particular lead nuclei (Pb), at 2.3 TeV per nucleon. Inside this circular accelerator a set of protons (or ions) so-called bunch racing clockwise at near the speed of light (99.9999991%) crashes into an other bunch speeding anticlockwise. The energy involved in the collisions is so great that, in a sub-microscopic region at the heart of the collisions, it briefly generates conditions similar to those that occurred shortly after the birth of the Universe. This machine is installed in the 27 km tunnel, located underground between 50 m and 175 m depth, and was built between 1984 and 1989 for the LEP e^+e^- machine. In 2001, LEP was dismounted to give way to the LHC.

Within the tunnel are two adjacent parallel beam pipes and surrounded by superconductive magnets. In total there are 1232 dipole magnets which bend the beams into its circular orbit and 392 quadrupole magnets corresponding to the function of beams focusing. The strength of the focusing magnets is required to be high to squeeze the transverse beam sizes and, thus, increase the probability of collisions. The adopted design at the LHC is approximately 80% of the arcs is filled with dipole magnets. Dipoles are also equipped with sextupoles, octupoles and decapoles, function of which is to correct non-linear dynamics of the beams. Keeping 7 TeV proton energy beam on the designed orbit implies the use of magnetic bending

fields of 8.4 T. Generation of such field requires to use superconducting magnets at the limit of the existing technologies. Approximately 96 tonnes of liquid helium is needed to maintain the superconductivity of the magnets at operational temperature of 1.9 K (-271.3C), making the LHC the largest cryogenic facility in the world. A detailed description of the LHC and the CERN accelerator complex is given in Ref. [32].

3.1.1 Acceleration chain

A succession of small to large accelerators is used to accelerate the protons extracted from hydrogen gas to the energy needed for injection into the LHC. Figure 3.1 shows the CERN accelerator complex including all pre-acceleration steps before the LHC. The process of the acceleration starts from the linear accelerator

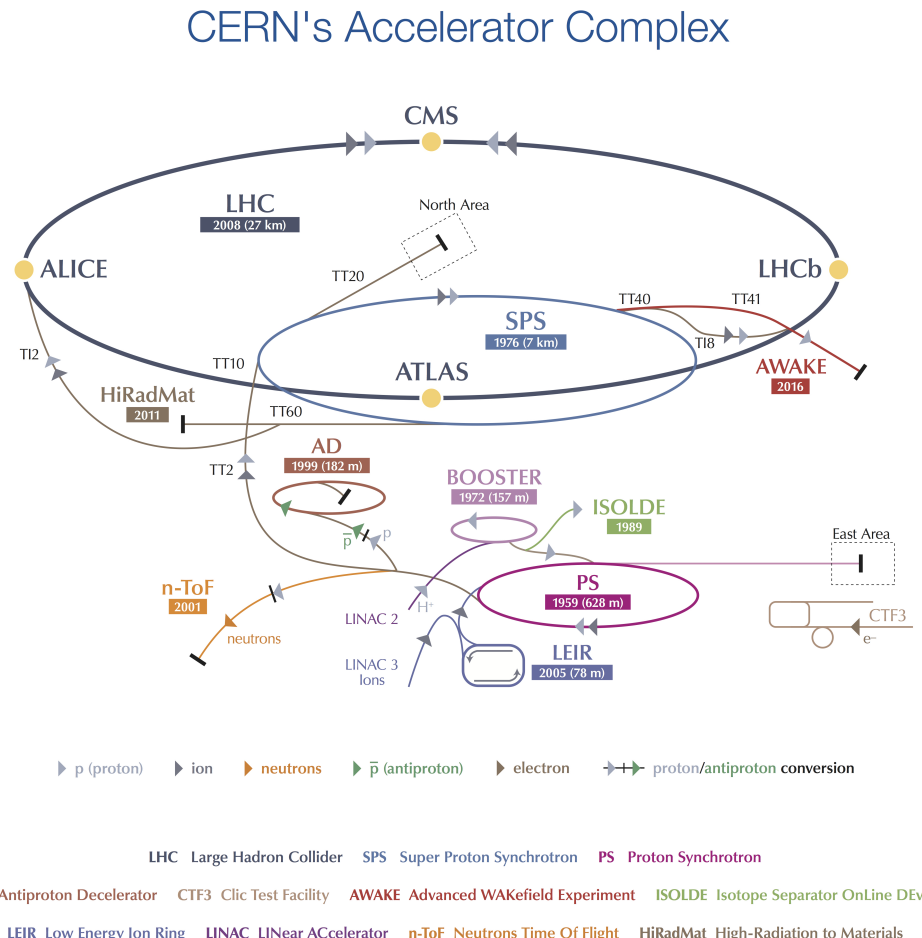


Figure 3.1: Overview of the CERN accelerator complex, including the LHC and its pre-accelerators [33]. The four main LHC experiments are depicted, too

Linac 2, which accelerates the protons up to 50 MeV. The beam is then injected into the Booster. The Booster accelerates the protons to 1.4 GeV and feeds the Proton Synchrotron (PS), where the protons are further accelerated to 25 GeV. The next chain is the Super Proton Synchrotron (SPS), which is 6.9 km long. Here the protons reach the energy of 450 GeV before they are transferred to two beam-pipes of the LHC main ring. It takes several minutes to fill the LHC ring and about 15 minutes to accelerate beams to their maximum energy of 6.5 TeV using eight radio frequency (RF) cavities at $f_{RF} = 400\text{MHz}$.

Each time a beam passes the electric field in the RF cavity, some of the energy from the radio waves is transferred to the particles, nudging them forwards. The beams are injected in bunches contained $\sim 10^{11}$ protons each beams contained 2808 bunches are spaced by 25 ns.

The particles created in LHC collisions are distributed over the full solid angles around the Interaction Point (IP), in four IP point is installed four detectors to record those particles and identified them as ATLAS, CMS, ALICE and LHCb each is specific to study a category of physics. LHCb built to study flavour physics looking at the properties of b-hadrons, and the ALICE detector that is specialised for measurements on heavy-ion collisions. CMS and ATLAS are general-purpose detectors. They allow to make precision measurements of SM processes, including the properties of the Higgs boson, and to search for physics beyond the SM. Section 3.2 is dedicated to ATLAS detector as the thesis is done withing ATLAS collaboration.

3.1.2 Luminosity

The number of collected events is proportional to the integrated luminosity \mathcal{L}_{int} multiplied by the cross section:

$$N_{events} = \int \mathcal{L} dt \times \sigma_{process}. \quad (3.1)$$

The instantaneous luminosity is the quality factor for colliders, measuring the intensity of the beam, luminosity is defined as :

$$\mathcal{L} = \frac{N_b^2 n_b f_r \gamma_r}{4\pi \epsilon_n \beta^*} F, \quad (3.2)$$

where for the design luminosity (nominal parameters for the LHC are given in parenthesis):

- N_b is the number of particle per bunch ($\sim 10^{11}$).
- n_b is the number of bunch per beam (2808).
- f_r is the revolution frequency (11245 Hz).
- γ_r is the relativistic γ factor (~ 700).
- ϵ_n is the normalized traverse beam emittance-characterizes its spread in coordinate and momentum phase space (3.75 μm).
- β^* is the beta function at the collision point determined by the magnets configuration (for ATLAS 0.55 m).
- F is the geometric luminosity reduction factor due to the crossing angle at the interaction point.

For optimising the analysis procedure, ATLAS has defined a basic time unit called Luminosity Block (LB) where the luminosity is assumed to be stable inside each LB. The typical LB duration is one to two minute. Data are analyzed under the assumption that each LB contains data taken under uniform conditions (data quality). To define a data sample for physics, quality criteria are applied to select LBs where the conditions are acceptable. The average luminosity in the LB is multiplied by the LB duration to provide the integrated luminosity delivered in the given LB.

The design luminosity of LHC is $10^{34} \text{ cm}^{-2}\text{s}^{-1}$. The integrated good quality data of Run-1 is approximately 25 fb^{-1} as shown in Figure 3.2, which Higgs self-coupling measurement does not benefit from it because of the low $\sigma_{pp \rightarrow HH}$. During the first long shutdown (LS1), LHC the energy of the beam is increased from 3.5 TeV to 6.5 TeV which increase the luminosity.

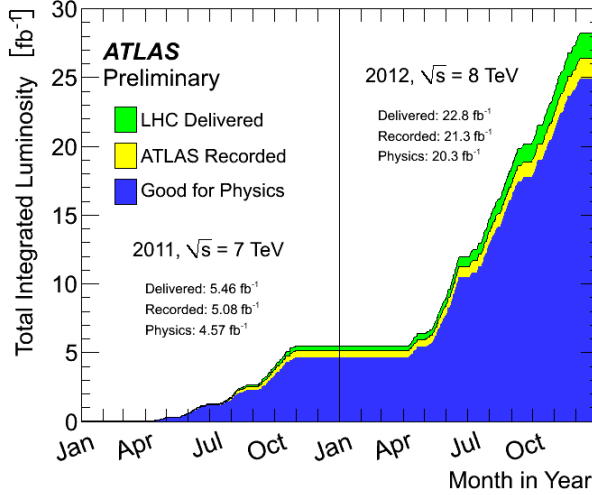


Figure 3.2: Cumulative luminosity versus time delivered to (green), recorded by ATLAS (yellow), and certified to be good quality data (blue) during stable beams and for pp collisions at 7 and 8 TeV centre-of-mass energy in 2011 and 2012 (Run 1).

Figure 3.3 shows the delivered and recorded luminosity during the Run 2 data taking [34]. $\mathcal{L}_{int} = 139 \text{ fb}^{-1}$ is used for physics since small fraction of full Run 2 data does not pass the good quality criteria compare to Run 1. For this reason the analyse described in this thesis is performed on the 2015-2018 data subsets.

Knowing the cross section of the $HH \rightarrow \gamma\gamma\bar{b}b$ production, one can evaluate the number of events available

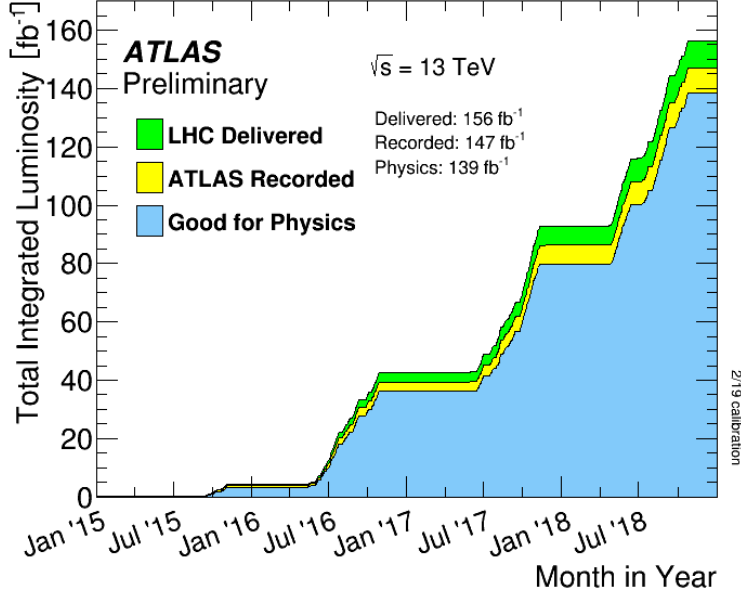


Figure 3.3: Luminosity delivered by the LHC during the Run 2 data taking. ATLAS recorded this data with an efficiency above 90%.

for the analysis as $N_{HH \rightarrow \gamma\gamma\bar{b}b} = \mathcal{L}_{int} \cdot \sigma_{pp \rightarrow HH} \cdot Br(HH \rightarrow \gamma\gamma\bar{b}b)$ that leads to about 12 events.

3.1.3 Pile-up

Because of the very high density of protons at the collision points, more than one proton interact when two LHC bunches cross each other at the center of the experiment. This is commonly referred to as pileup. On top of the usual *in – time* pileup, defined as the collision events occurring during the same bunch-crossing as the event of interest, one also has to consider *out – of – time* pileup, coming from remnants of information found in some of the detector subsystems that end-up being attributed to the wrong bunch-crossing, and therefore to the wrong event typically from previous collisions. Figure 3.4 shows the average number of simultaneous interactions per bunch crossing for Run 2.

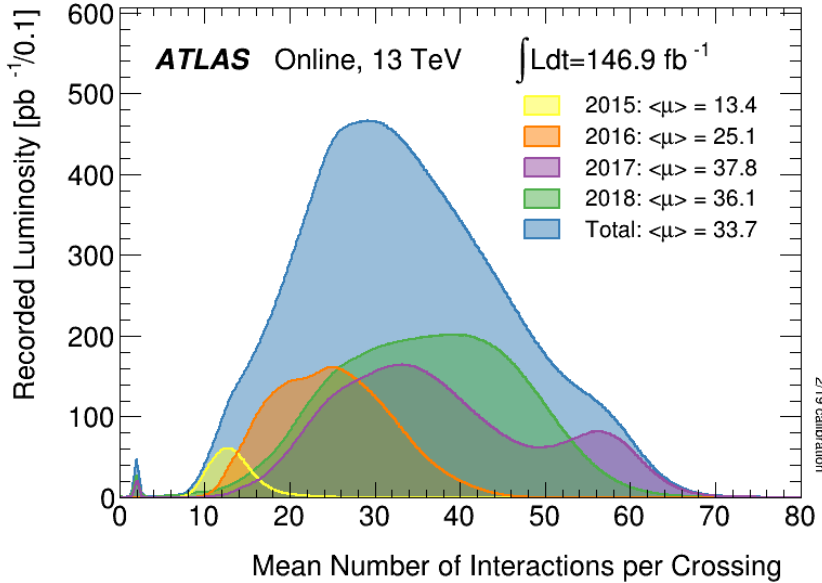


Figure 3.4: Recorded integrated luminosity as function of the mean number of interaction per bunch crossing in pp collisions recorded by the ATLAS detector during Run 2 at 13 TeV [34].

3.2 ATLAS A Toroidal LHC ApparatuS detector

The ATLAS detector is one of the four experiments placed on the four crossing points of the LHC beams. It is currently the largest experiment particle physics with a length of 46 m along the beam pipe and a transverse diameter of 25 m and more than 7000 tons of weight [35]. It is a superposition of four sub-detectors, each optimized for the identification and the measurement of a specific category of particles : Inner Tracker, Electromagnetic Calorimeter (ECAL), Hadronic Calorimeter (HCAL) and Muons Spectrometer. It is composed of central called Barrel and two End-Cap to cover the 4π solid angle. Its geometry is optimised to detect particles produced orthogonal to the beam pipe and allow for forward detection to estimate the energy of invisible particles. The detector has been operating since 2008, taking alignment data with cosmic rays before the LHC launch, and its data is exploited by a collaboration of about 3000 scientific authors from 181 institutions in 38 countries. An overview sketch of the ATLAS detector is shown in Figure 3.5.

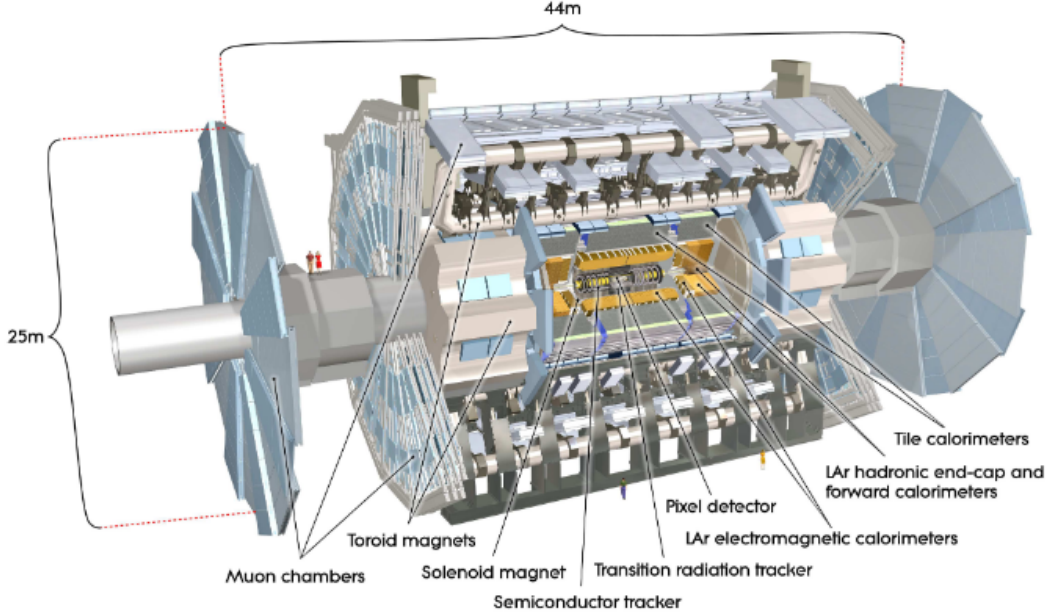


Figure 3.5: Sketch of the ATLAS detector with its different sub-detectors.

3.2.1 Coordinated system

The coordinate system used in the ATLAS experiment is cylindrical coordinates where the z-axis is along the LHC beam pipe, the x-axis pointing toward the center of the LHC ring and the y-axis pointing upward. A physic object (particle) is identified by its transverse component of the three-momentum $p_T = \sqrt{p_X^2 + p_Y^2}$, its azimuthal angle $\phi \in [-\pi, \pi]$ formed by the three-momentum and the x-axis and its polar angle $\theta \in [0, \pi]$, i.e the angle between the three-momentum and the z-axis.

The polar angle is expressed in terms of the pseudo-rapidity η , defined as

$$\eta = -\log[\tan(\theta/2)]. \quad (3.3)$$

In collisions involving, the adoption of η instead of θ ensure the detector balance over particles and particles distribution recorded is approximately flat with respect to η .

$$\frac{\partial \sigma_{QCD}}{\partial \eta} = cte. \quad (3.4)$$

The pseudo-rapidity η coincides for relativistic particles to the rapidity y , defined as

$$y = \frac{1}{2} \left(\frac{E + p_Z}{E - p_Z} \right), \quad (3.5)$$

where E is the particle energy. Figure 3.6 shows the coordinate system common to ATLAS and CMS experiments.

3.2.2 The Inner Tracker

The Inner Detector (ID) has been designed to detect and reconstruct the path of the electrically charged particle bent by a 2T solenoid magnetic field. It also provides a good momentum resolution by reconstructing the curvature and the direction, and both primary and secondary vertex measurements for tracks

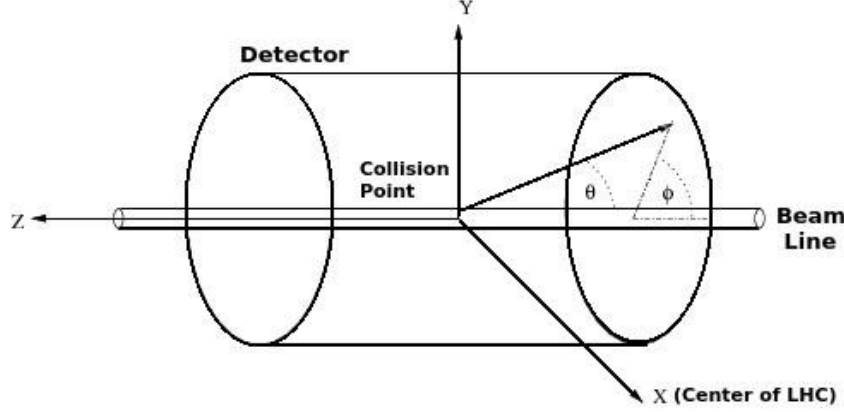


Figure 3.6: Coordinate system used by the ATLAS and CMS experiments at the LHC.

above approximately 0.5 GeV[36, 37]. In terms of acceptance, the ID covers region of $|\eta| \leq 2.5$. To achieve the momentum and vertex resolution requirements imposed by the physics goals at the LHC and the very large track density environment, the ID high-precision measurements must be made with fine detector granularity. The ID is composed of four complementary sub-detectors: IBL, the Pixel Detector, the Semi Conductor Tracker (SCT) and the Transition Radiation (TRT). The magnetic field of 2 T is provided by a solenoid inserted between the ID and the EM calorimeter. The layout of the Inner Detector (ID) is illustrated in Figure 3.7.

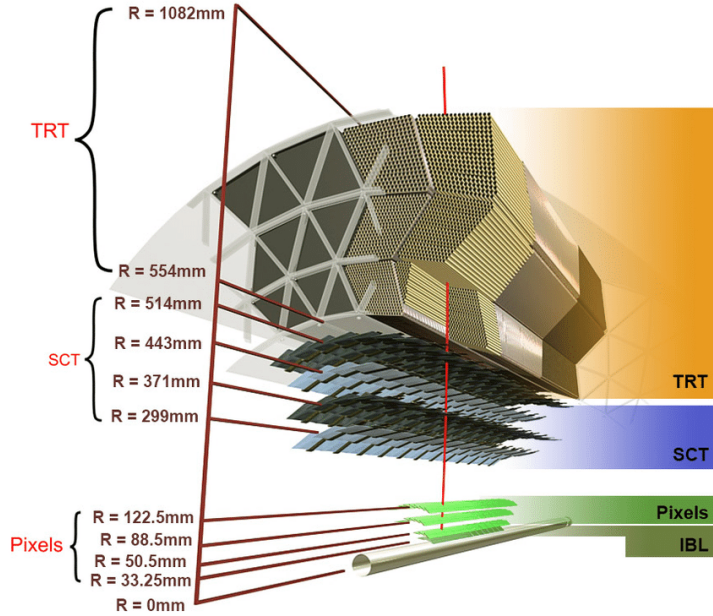


Figure 3.7: Layout of the Inner Detector (ID) [38].

3.2.2.1 IBL

In 2014, at the first LHC long shutdown, the ATLAS pixel detector was upgraded with a pixel layer installed close to the beam pipe called Insertable B-Layer (IBL) [39]. Its motivations are :

- Insure the good identification of the primary vertex which play an important role in b -jet identification (b -tagging), which in turn significantly improves the sensitivity of many analyses. Inefficiencies in

the other layers can be partially compensated during reconstruction at the cost of an increased fake rate, the IBL restore the full b -tagging efficiency even in case of a complete B-layer failure.

- Luminosity effects, The current pixel detector was designed for a peak luminosity of $10^{34} cm^{-2}s^{-1}$. With high luminosity the event pileup is increased, leading to high occupancy that can induce readout inefficiencies, would thereby limit the b -tagging efficiency. The addition of the IBL layer helps to preserve tracking performance in face of luminosity effects.

Strong constraints and project specifications have a substantial impact on the technologies required for the IBL. IBL covers the region of $|\eta| < 2.58$ in pseudo-rapidity and located at a mean radius of 33.2 mm around the beam pipe. The pixels uses 12 million pixels with a typical size of $50 \times 250 \mu m$. The IBL consists of 14 staves with each 20 modules made using planar sensors. The temperature of the IBL is controlled using a bi-phase CO₂ cooling system. Figure 3.8 shows the IBL within the Pixel Detector volume and around the beam pipe.

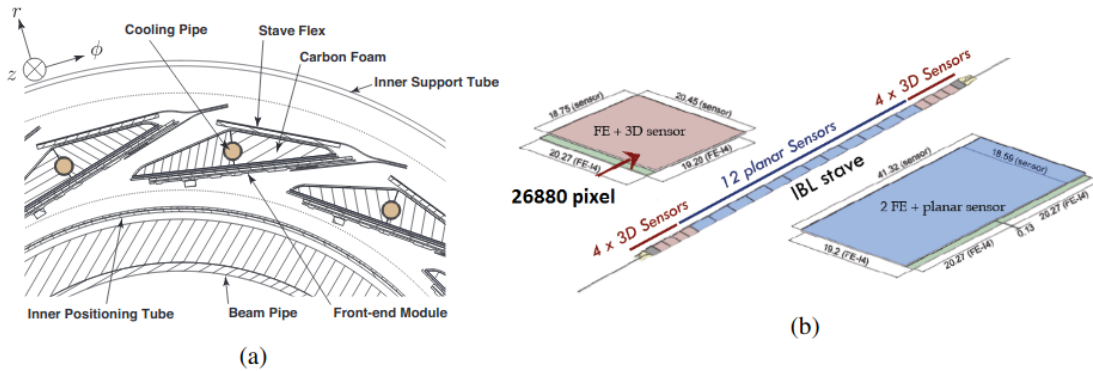


Figure 3.8: (a) Transverse view of 3 of the Insertable-B-Layer (IBL) staves, located directly on the beam pipe. (b) The layout of one of the 14 IBL staves [38].

Additional measurement point provided by IBL improves significantly the reconstructed parameters by the tracker. Figure 3.9 shows the improvement in impact parameter resolution due to the IBL as measured from early Run 2 data with respect to Run 1. In addition to a factor of 4 reduction in reconstruction times [41], Figure 3.10 shows the improvement achieved with IBL for the performance of tracking in dense environments (TIDE). Improvements in tracking have a direct impact on vertex identification and b -tagging. Figure 3.11 shows the improvement in the b -tagging efficiency with IP3D+SV1 b -tagging algorithms respect to Run 1 algorithm due to the IBL [43, 44]. The IP3D and SV1 algorithms will be explained later in the thesis.

3.2.2.2 Pixel Detector

With the existing technology at that time (2000s), the Pixel Detector (PD) is designed to provide high-granularity, high-precision measurements as close as possible to the interaction point (IP). It consists of three barrel layers placed at the radius of 50.5 mm, 88.5 mm and 122.5 mm centered around the beam axis and two end-cap with three disc layers each positioned at $|z| = 495.580$ and 650 mm . It provides three measurement points per track. The system is designed to be highly modular, containing approximately 1500 identical barrel modules and 1000 identical disk modules, each module is composed of 61440 pixel elements of silicon semi-conductor. In total there are about 80 million readout channels in the whole PD. The spatial resolution for the barrel modules is $10\text{ }\mu m$ in $r\phi$ and $66\text{ }\mu m$ in z , for the end-caps the spatial

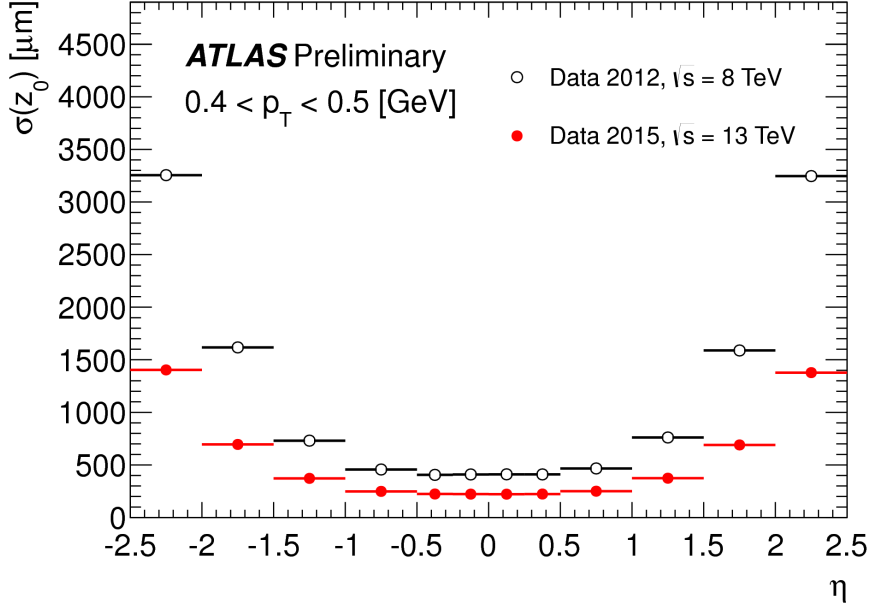


Figure 3.9: Unfolded longitudinal impact parameter resolution measured from data in 2015, $\sqrt{s} = 13$ TeV, with the Inner Detector including the IBL, as a function of η for values of $0.4 < p_T < 0.5$ GeV compared to that measured from data in 2012, $\sqrt{s} = 8$ TeV [40].

resolution in $r\phi$ is same as the barrel and $115\mu\text{m}$ in r . The main limitation of the pixel detector is the radiation hardness as the expected fluence is at the tolerable limit.

3.2.2.3 Semi Conductor Tracker

The SCT system is designed to provide four precision points per track in the intermediate radial range, contributing to the measurement of momentum, impact parameter and vertex position. The barrel and end-caps SCT are four layers of silicon microstrip for barrel and nine disks for end-caps. The spatial resolution is $16\mu\text{m}$ in $r\phi$ for both the barrel and the end-caps. The four complete barrels are positioned in radius of 300, 373, 447 and 520 mm. Tracks can be distinguished if separated by more than $\sim 200\mu\text{m}$. There are 6.3 millions readout channels for the SCT.

3.2.2.4 Transition Radiation Tracker

The TRT is positioned at the outer part of the ID. It consist of 370000 drift tubes called straws. Each straw has a diameter of 4 mm and 1.44 m in long. The straws are filled with a gas mixture of 70% Xe , 27% CO_2 and 3% O_2 . Its wall acts as a cathode and kept at high voltage. The anode is a $30\mu\text{m}$ diameter plated tungsten wire placed in the center of the straw. When a charged particle traverses a straw, it ionizes the gas and the produced electrons travel through the anode generating an electric signal. To keep the TRT performance to be constant, the close-loop gas system is used maintaining the correct gas fractions. The straws are arranged to be parallel to the beam-pipe in the barrel and perpendicular in the end-cap region. There are about 50k straws in the barrel and 320k straws in the end-cap providing high precision measurement for each track. The radial resolution is about $130\mu\text{m}$.

In the Perigee representation, tracks are described using the parameters of a helical trajectory at the point of closest approach to the z-axis: the transverse impact parameter d_0 , the z coordinate z_0 , the angles θ and ϕ and the inverse of the particle momentum multiplied by the charge q/p , as illustrated in Figure 3.12. The expected momentum resolution of the inner detector, without the IBL, is given by:

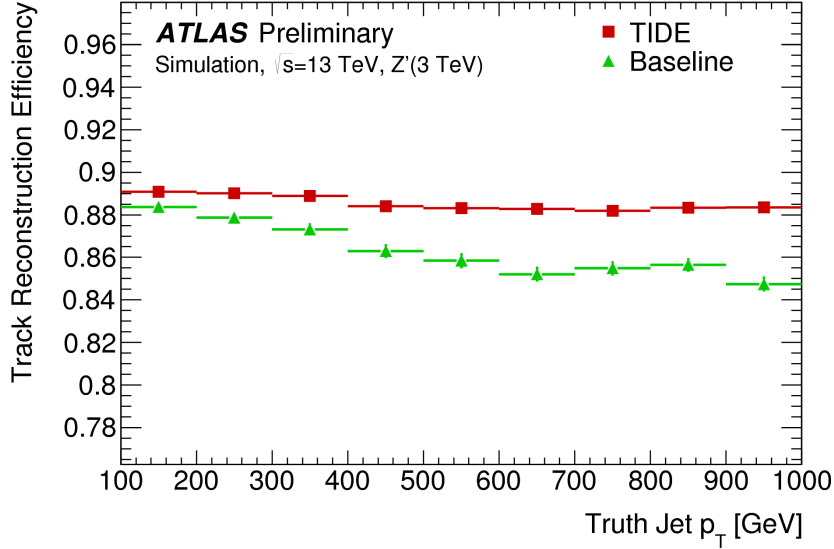


Figure 3.10: The average efficiency to reconstruct primary tracks with a production vertex before the first layer in jets as a function of jet p_T . The same sample generation, with limited statistics, is used for both reconstruction algorithms resulting in correlated features [42].

$$\sigma(1/p_T) \cdot p_T = 0.036\% \cdot p_T[GeV] \oplus 1.3\%, \quad (3.6)$$

\oplus denote the quadrature addition.

3.2.3 Calorimeter system

Based on the calorimetry, the ATLAS calorimeter system is designed to provide a precise energy and position reconstruction for electromagnetic particles (electrons, photons) and jets (hadrons). The good hermiticity of the calorimeter ($|\eta|$ up to 5) also allows to measure the missing transverse energy and provides the separation of electrons and photons from hadrons and jets. The calorimeter system is composed of two calorimeters: the electromagnetic calorimeter (ECal) and the hadronic calorimeter (HCal). Both are sampling calorimeters, with alternating layers of a heavy absorber material and an active material in which an ionisation signal is produced. Figure 3.13 shows a three dimensional view of the ATLAS calorimeter system.

3.2.3.1 Electromagnetic calorimeter

The ECal is the first sub-detector after the ID. Is optimised for the reconstruction of the energy of electrons and photons exploiting their showers [46]. It covers the region of $|\eta| < 3.2$ excluding the region $1.375 < |\eta| < 1.52$ which correspond to the transition region between the barrel and end-caps. The barrel part covers $|\eta| < 1.475$, while the two end-caps cover $1.375 < |\eta| < 3.2$. The barrel and end-caps are composed of alternated layers of absorbing material lead ($Z=82$) and plates (~ 1 mm thick), to enforce the development of the full EM showers within EM envelop and separated by active medium Liquid Argon (LAr) of 2 mm thick. The advantages of LAr, such as radiation hardness, intrinsic linear behaviour, cheapness compared to other noble gases, have been considered to outweigh the difficulties associated with the need of cryostats and signal feed-throughs. The total thickness of the calorimeter is at least 22 radiation lengths in the barrel, and more than 24 radiation lengths in the end-caps. The radiation lengths X_0 is defined as the scale after

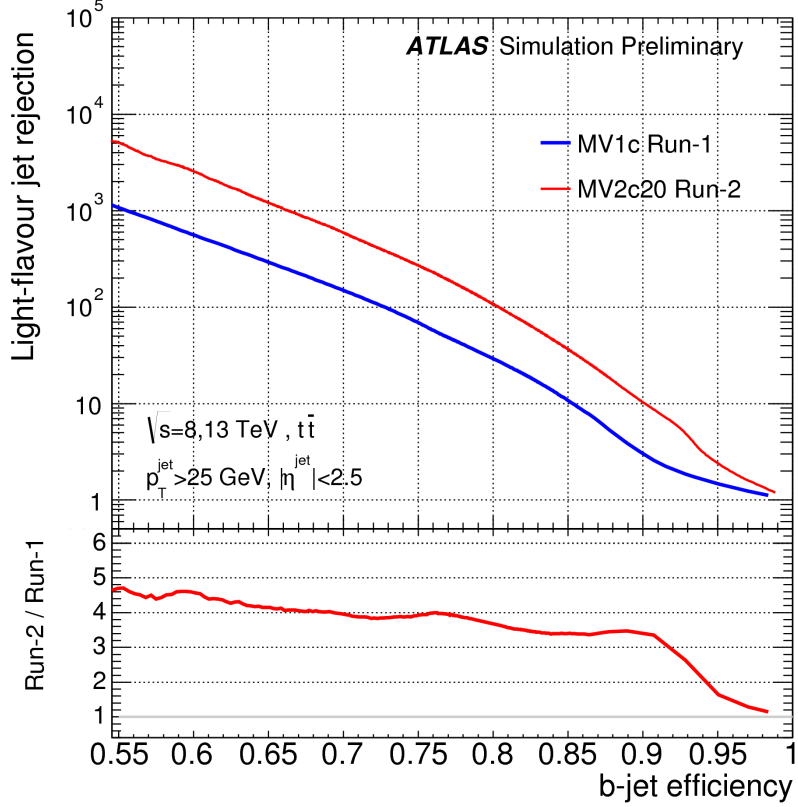


Figure 3.11: Rejection factor against light jets as a function of b -jet efficiency for the combined IP3D+SV1 tagger. Compared are the results with and without IBL.

which high-energy electrons loose all but $1/e$ of their initial energy. X_0 of lead is 5.6mm. Electrons and photons traversing the calorimeters initiate electromagnetic cascades, in which e^+e^- pair production and bremsstrahlung processes occur. High-energy electrons predominantly loose energy in matter through bremsstrahlung, while high-energy photons create e^+e^- . EM particle produce shower when passed through ECal until its energy falls below the critical energy E_c . E_c , can be defined as the energy for which the energy loss per X_0 due to ionisation of the material is equal to the particle energy. In lead, $E_c=7.4$ MeV for electrons. The EM shower ionizes the atom of the liquid Argon generating an electric signal proportional to the energy deposit by the particle. The ionization is drifted to the electrode under electric field generated by the high voltage of 2000 V. To provide a huge signal response and hermiticity, ATLAS Collaboration adopted a particular geometry for the ECal: *accordion* geometry. In the barrel, the accordion waves are axial and run in ϕ ; the folding angles of the waves vary with radius to keep the liquid-argon gap constant and reduce the dead zone. In the end-caps, the waves are parallel to the radial direction and run axially. The size of the drift gap on each side of the electrode is 2.1 mm. Figure 3.14 shows the accordion shape of the EM calorimeter. The ECal is further segmented in three longitudinal layers, to measure the longitudinal shower development called respectively strip, middle and back. It has different EM cells granularity $\Delta\eta \times \Delta\phi$ per layer. Cells of the middle layer (Lr2) in the barrel region are 0.025×0.025 , while for the strip (Lr1) cells are 8 times finer in the $|\eta|$ direction providing a precise η measurement of incident particles. The back layer (Lr3) cells has a twice coarser granularity in η and the same ϕ segmentation as in Lr2. Before the EM barrel calorimeter there is a Presampler (PS) LAr detector (Lr0), covering range $|\eta| < 1.8$ and placed to start the shower before the calorimeter. PS has the finest granularity with a cell size of $\Delta\eta \times \Delta\phi = 0.003 \times 0.1$ used for $\pi \rightarrow \gamma\gamma$ background separation.

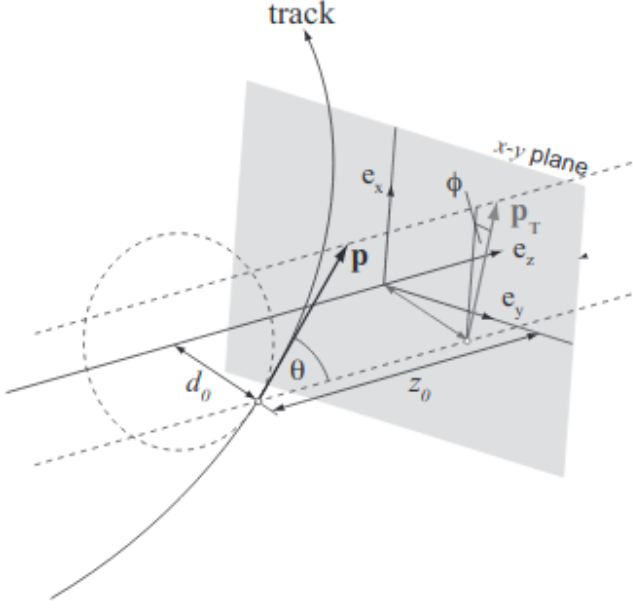


Figure 3.12: The Perigee representation of the track [45].

The number of samplings and the granularity in each of the samplings are summarized in Table 3.1. Physics studies showed that precision physics can hardly be extended beyond a pseudorapidity of 2.5. For

Sampling	$ \eta < 1.5$	$1.5 < \eta < 1.8$	$1.8 < \eta < 2.0$	$2.0 < \eta < 2.5$	$2.5 < \eta < 3.2$
Presampling	0.025×0.1	0.025×0.1			
Strip	$0.025/8 \times 0.1$	$0.025/8 \times 0.1$	$0.025/6 \times 0.1$	$0.025/4 \times 0.1$	0.1×0.1
Middle	0.025×0.025	0.025×0.025	0.025×0.025	0.025×0.025	0.1×0.1
Back	0.050×0.025	0.05×0.025	0.05×0.025	0.05×0.025	

Table 3.1: Granularity of the EM calorimeter ($\Delta\eta \times \Delta\phi$) [46].

this reason, the small wheel has a coarser granularity and only two samplings in depth. EM calorimeter resolution is given by:

$$\sigma_E/E = \frac{10\%}{E} \oplus 0.17\%. \quad (3.7)$$

3.2.3.2 Hadronic calorimeter

At high energy colliders, quarks and gluons fragment to a beam of particles called jets (hadronic showering). The Hadronic Calorimeter (HCal) completes the measurement of the jets energy [47]. Hadronic showers are larger than electromagnetic ones, thus it needs to be large enough to contain the hadronic showers and reduce the punch-through hadrons penetrating to the muon system. The total thickness is chosen to be about $11 X_0$ to allow good performance on resolution for high energy jets. The hadronic calorimeter is divided into the Tile calorimeter and the LAr hadronic end-caps calorimeter. The barrel calorimeter is made of steel as absorbing material and scintillating plastic tiles as active medium and cover the range $|\eta| < 1$ with two extensions in the range $0.8 < |\eta| < 1.7$. The end-caps cover the range

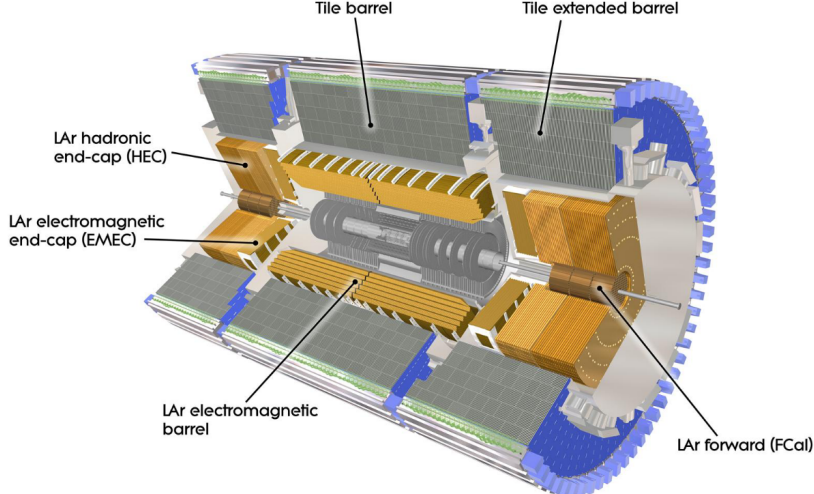


Figure 3.13: ATLAS Calorimeter system.

$1.5 < |\eta| < 3.2$ and it is composed of two wheels made of parallel copper plates with LAr as active material in between. For the determination of the missing energy a good hermetic coverage is essential. Therefore ATLAS calorimeter is also equipped with a calorimeter covering the very forward region of $3.1 < |\eta| < 4.9$ the LAr Forward Calorimeter (FCal).

The Tile calorimeter provides signal by the tiles scintillation. The tiles are perpendicular to the beam-pipe with 3 mm thick. It consists of a barrel ($|\eta| < 1.0$) and two extended barrels ($0.8 < |\eta| < 1.7$). The Tile calorimeter is segmented into three layers. The dimension of the cells corresponds to $\Delta\eta \times \Delta\phi = 0.1 \times 0.1$ in first two layers and $\Delta\eta \times \Delta\phi = 0.2 \times 0.1$ in the last layer to contain the hadronic shower. A vertical gap of 68 cm wide between the barrel and extended barrel regions is used for passage of cables from the ID and the EM calorimeter.

LAr cover end-cap and forward regions with $1.5 < |\eta| < 4.9$. Each end-cap calorimeter (HEC) consists of two independent wheels of equal diameter with copper absorber plates. The end-cap calorimeter is divided into front, middle and back longitudinal layers. The FCal is placed at a distance of about 5 meters from the interaction point. It high density detector facing a very high particle flux and consisting of three wheels on each side employing liquid argon as an active material. The innermost wheel is optimized for electromagnetic showers and employs copper as the absorber. While the other two wheels measure hadronic showers using tungsten as absorbing material. The granularity of the hadronic LAr calorimeter is $\Delta\eta \times \Delta\phi = 0.1 \times 0.1$ for $1.5 < |\eta| < 2.5$ and $\Delta\eta \times \Delta\phi = 0.2 \times 0.2$ for $2.5 < |\eta| < 3.2$ while the forward calorimeter has $\Delta\eta \times \Delta\phi = 0.2 \times 0.2$. The HCal is designed to measure the energy with a resolution of [48]:

$$\sigma_E/E = \frac{50\%}{E} \oplus 3\%. \quad (3.8)$$

3.2.4 Muon Spectrometer

Muons are minimally ionising particles in the detector due to their relatively high mass, therefore are not stopped by the calorimeter. The Muon Spectrometer (MS) is the outermost part of the ATLAS detector dedicated to detect muons exiting the calorimeter and measure their momentum in the range of $|\eta| < 2.7$ [49]. A large superconducting air-cored toroid magnet is used to bend muons trajectories. Over the range $|\eta| < 1.4$, magnetic bending is provided by the large barrel toroid. For $1.6 < |\eta| < 2.7$ region muon tracks

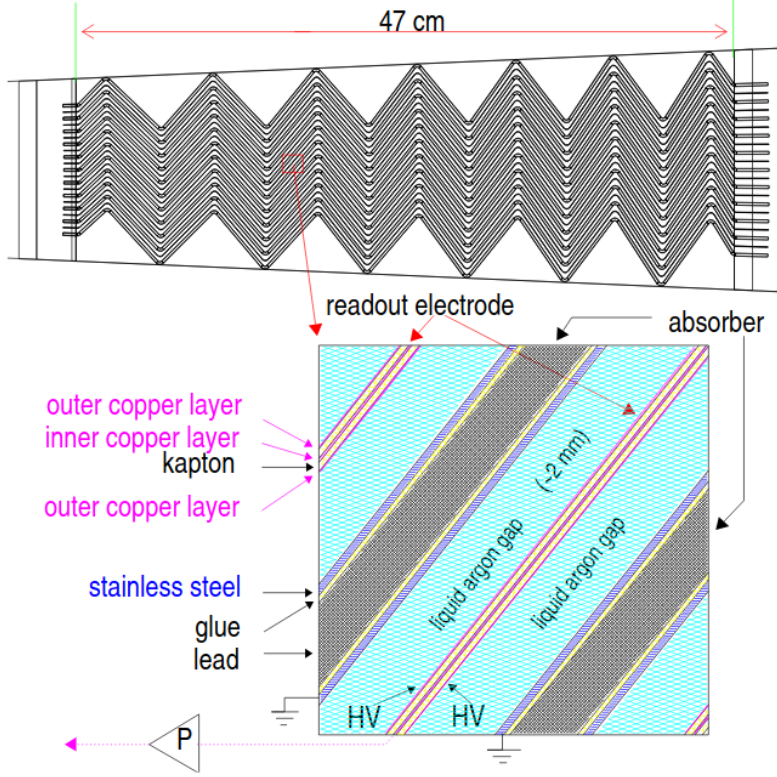


Figure 3.14: Accordion shape of the EM calorimeter.

are bent by two smaller end-cap magnets inserted into both ends of the barrel toroid. Over $1.4 < |\eta| < 1.6$, usually referred to as the transition region, magnetic deflection is provided by a combination of barrel and end-cap fields. Two different functions are accomplished by the MS: triggering and high precision tracking. The tracking is performed by the Monitored Drift Tubes (MDTs) and by Cathod Strip Chambers (CSCs) at large pseudo-rapidity. However, trigger system covers the region up to $|\eta| < 2.4$, and it is composed by Resistive Plate Chambers (RPCs) in the barrel and Thin Gap Chamber (TGC) in the end-caps. The conceptual layout of the spectrometer is shown in Figures 3.15.

The Monitored Drift Tubes are aluminium drift tubes with a diameter of 29.970 mm as Figure 3.16 shows, operating with a gas mixture of 93% of Ar and 7% of CO_2 Ar/CO₂ at 3 bar pressure. Each chamber consists of two sections with three (inner station) or four (middle and outer station) layers of the drift tubes. Tungsten-rhenium wire of 50 μm collects the electrons resulting from ionization at a potential of 3 kV. The maximum drift time can reach about 700 ns. The MDTs are designed for precise tracking of muons and cover most of the MS pseudorapidity total coverage, with a single-hit resolution of about 35 μm per chamber.

The Cathode-Strip Chambers are multi-wire proportional chambers filled with a mixture of 80% of Ar and 20% of CO_2 with cathode planes segmented into strips in an orthogonal direction to the beam axis. The CSCs cover the range of $2.0 < |\eta| < 2.7$ which is partially covered by the ID and has higher particle flux, because of their better time resolution and rate capability than MDTs. The CSC chambers have a slightly lower resolution than the MDTs, with 40 μm in the tracks bending plane, and 5 mm in the transverse plane.

For trigger purpose, the RPCs placed in the barrel, covering the range $|\eta| < 1.05$, are arranged into three concentric layers around the beam axis and placed before or after the MDT layers as Figure shows 3.15.

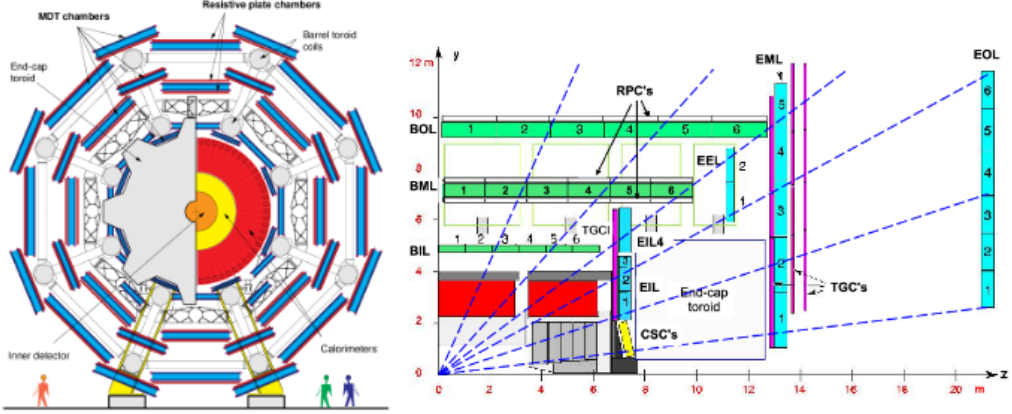


Figure 3.15: Side view of one quadrant (right) and transverse view (left) of the muon spectrometer.

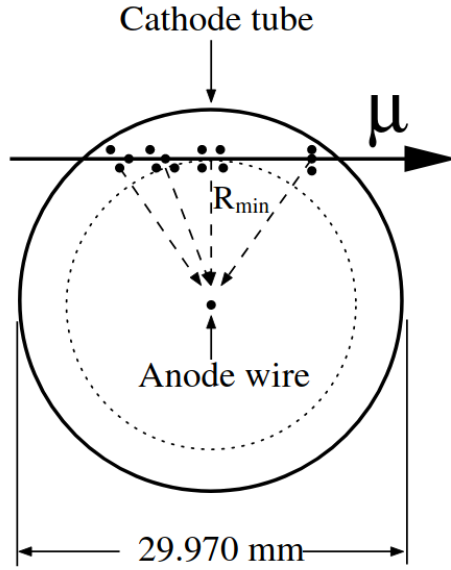


Figure 3.16: Transverse cross section of the MDT tube.

The RPC unit is composed of gap of 2 mm formed by two parallel electrodes. The gap is filled with a mixture gas of 94.7% of $C_2H_2F_4$, 5% of $Iso-C_2H_2F_4$ and 0.3% of SF_6 . The electric field between electrodes is about 4.9 kV/mm. The end-caps are equipped with the TGCs up to $|\eta| = 2.4$. The TGCs are multi-wire proportional chambers filled with a mixture 55% of CO_2 and 45% of $n - C_5H_{12}$. The TGCs are arranged in seven layers in each side.

The overall momentum resolution $\frac{\sigma_{p_T}}{p_T}$ provided by the muon system is 4% (1%) at 5GeV (1TeV) [50].

3.2.5 Trigger

Collision rate at the center of ATLAS is 40MHz due to the bunch crossing in each 25 ns provided by LHC. At such a rate, it is technically not possible to fully process and store all data recorded by the ATLAS detector. The ATLAS trigger system was design to handle this problem, the purpose of the trigger system is to reduce the input of 40 MHz bunch crossing rate to an output rate of about 200 Hz in order to record

them for further analysis. This is done thanks to two separated trigger systems. The first level so-called Level-1 (L1) [51] is a hardware-based trigger that uses reduced granularity signals from the calorimeter and the muon spectrometer to identify Regions-Of-Interest (ROI) with high energy objects or high multiplicity at a latency of $2.5\ \mu\text{s}$. The L1 trigger system is responsible for reducing the rate to at least 75 kHz. Events passing the L1 trigger are then sent to the software-based High-Level Trigger (HLT) [52]. At the HLT, a fast analysis of these ROTs followed by an offline-like reconstruction of the events takes place with a processing time of around 0.2 s. The HLT creates output with a frequency of around 1 kHz. Often the final output rate cannot be made small enough [53]. In this case only random events are selected and stored.

3.3 Physics objects reconstruction

ATLAS provides energy deposits collected by sub-detectors. To interpret this raw output in terms of the event particles an advanced particle reconstruction chains have to be employed. These are described in this Section.

3.3.1 Track and Vertex reconstruction

Tracks are reconstructed in the ID (Section 3.2.2) using a sequence of algorithms [54, 55]. The inside-out algorithm starts from three points seeds in the SCT. A combinatorial Kalman filter (Iterative algorithm that provides best estimate of the state based on projection of earlier measurements and current measurement [56]) is then used to build track candidates from the chosen seeds by incorporating additional space-points from the remaining layers of the pixel and SCT detectors which are compatible with the preliminary trajectory. Ambiguities in the track candidates are resolved, and tracks are extended into the TRT. The inside-out algorithm is the baseline algorithm designed for the efficient reconstruction of primary charged particles. In a second stage, a back-tracking algorithm is used in track search starting from segments reconstructed in the TRT and extending them inwards by adding silicon hits. The back-tracking is designed to reconstruct secondaries particles. Finally tracks with a TRT segment but no extension into the silicon detectors are referred as TRT-standalone tracks. The track reconstruction efficiency is defined as the fraction of primary particles with $p_T > 400\ \text{MeV}$ and $|\eta| < 2.5$ matched to a reconstructed track. Figure 3.17 shows the track reconstruction efficiency as a function of p_T and η . Primary vertices are reconstructed using an iterative vertex finding algorithm [57]. Vertex seeds are obtained from the z-position at beam axis of the reconstructed tracks. An iterative χ^2 fit constrained with the beam spot position is made using the seed and nearby tracks. Tracks are weighted depending on the χ^2 to measure the compatibility with the fitted vertex [58]. Tracks displaced by more than 7σ from the vertex are used to seed a new vertex and the procedure is repeated until no additional vertices can be found. During reconstruction vertices are required to contain at least two tracks. The efficiency to reconstruct a vertex from a minimum bias interaction is shown in Figure 3.18. Vertices are matched to interactions by calculating the sum of the weights of the tracks in a vertex matched to each interaction.

3.3.2 Electron and Photon reconstruction

Photons and Electrons are reconstructed in a similar way using the EM calorimeter (Section 3.2.3.1). When these particles pass through the calorimeter dense medium, they start a showering process through cascading bremsstrahlung and electron pair production. Their shower are quite wide, therefore they deposit their energy in many calorimeter cells of each sampling. The electrical signal induced by electrons from

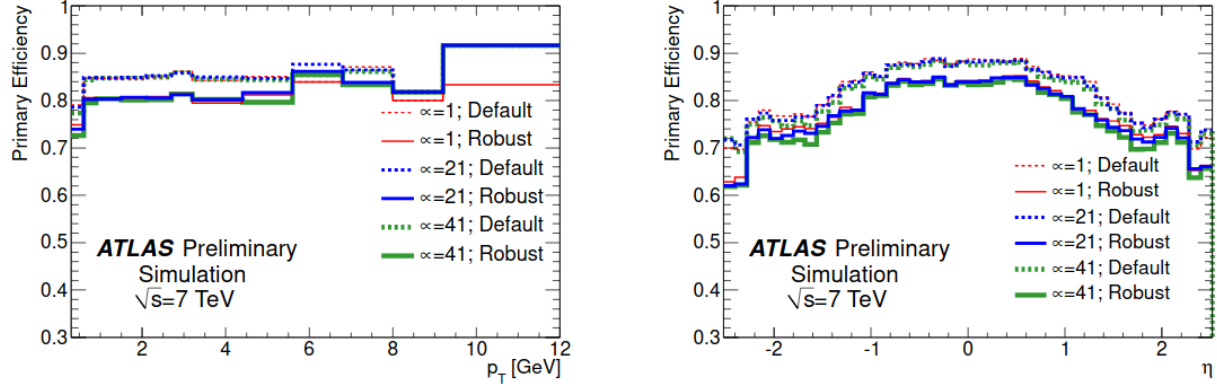


Figure 3.17: The primary track reconstruction efficiency in minimum bias Monte Carlo samples containing exactly one and on average 21 or 41 interactions. The distributions are shown for tracks passing the default(dashed) and robust (solid) requirements.

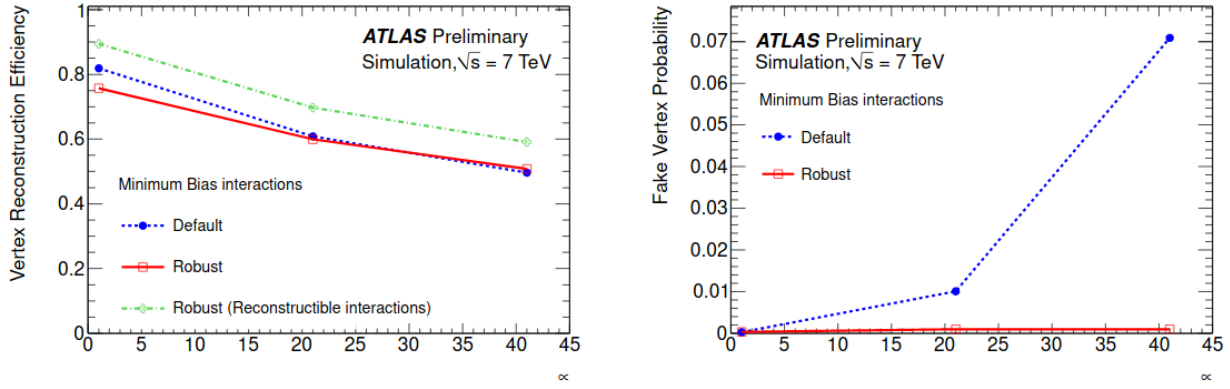


Figure 3.18: The vertex reconstruction efficiency (*left*) and fake probability (*right*) as a function of the aver-age number of interactions.

ionised active material (LAr) is proportional to deposited energy in the active volume of the calorimeter and used to compute the cell energy. Note that, the cell energy includes both the electronic noise which is about 10 MeV in the strip and 30 MeV in the middle and back layers, and the *pile – up* particles noise. The pile-up contributions can be either splitted into two components the *in – time* pile-up which due to particles coming from the same bunch crossing, and the *out – of – time* pile-up due to particles from previous bunch crossing. The total deposited energy is measured from the reconstructed EM clusters. To reconstruct the EM clusters, the EM calorimeter is divided into a grid of $N_\eta \times N\phi$ towers of size of the same middle layer granularity (0.025x0.025). Inside each of these elements, the energy of all cells in all longitudinal layers is summed into the tower energy. A window of fixed size 3×5 is moved across each element of the tower. If the window transverse energy E_T (defined as the sum of the transverse energy of the towers contained in the window) is a local maximum and is above a threshold (2.5 GeV), a cluster seed is formed. Then, if the reconstructed cluster can be associated with at least one reconstructed track, the candidate is classified as an electron. The described reconstruction algorithm until now is called *fixed – size* [59].

While, the reconstruction has been improved to use dynamic, variable-size clusters, called *super-clusters* [60]. This allows the recovery of low energy photons radiated due to bremsstrahlung interactions in the ID or electrons from photon conversions. In this scenario, the electron is defined as an object consisting of a super cluster and matched track. A converted photon is a cluster matched to a conversion vertex, and an unconverted photon is a cluster matched to neither an electron track or a conversion vertex. In contrast to the sliding window, the super-cluster selects clusters based on topologically connected calorimeter cells [61]. Figure 3.19 shows an illustration of super-clusters.

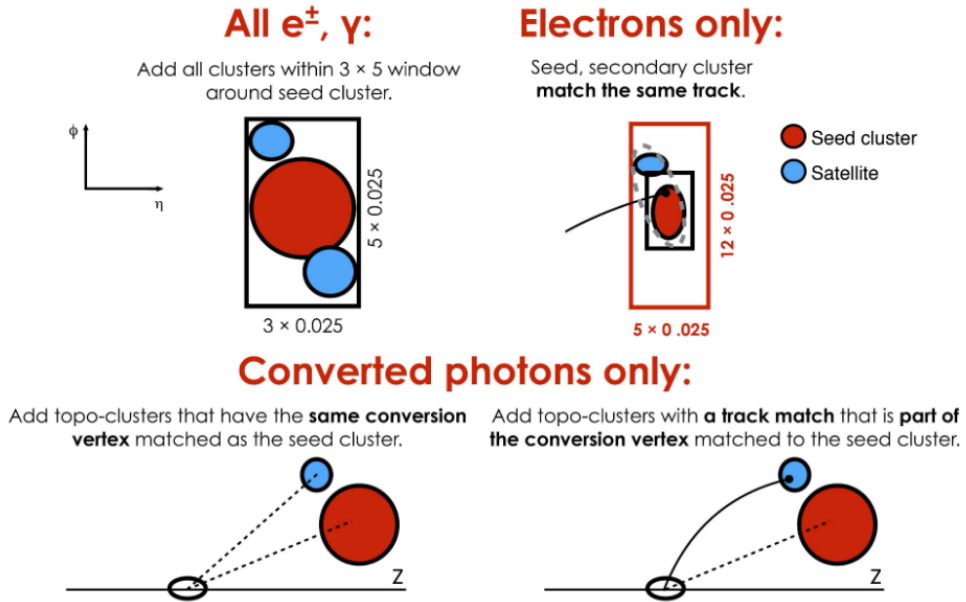


Figure 3.19: Diagram of the super clustering algorithm for electrons and photons. Seed clusters are shown in red, satellite clusters in blue.

The topo-cluster reconstruction starts from a cell with $|E_{cell}| > 4\sigma$, where σ is the expected cell noise includes the known electronic noise and an estimation of the pile-up noises. Then successively, all neighbouring cells with $|E_{cell}| > 2\sigma$ are added. The absolute cell energy is used to avoid biasing the cluster energy upwards due to negative energy induced by the calorimeter noise. The list of reconstructed topo-clusters is sorted according to descending total energy. The topo-clusters are tested one by one for use as super-cluster. For an electron the topo-cluster is required to have a minimum E_T of 1 GeV and matched to a track with at least four hits in the silicon detector [62], while for a photon the threshold is set to 1.5 GeV with no matched track or conversion vertex. For both, the electron and the photon case, to recover radiative losses, satellite clusters around that reconstructed cluster can be matched to the super-cluster. The seed clusters with their associated satellite clusters are called super-clusters. Tracks are matched to electron super clusters and conversion vertices to converted photon super clusters. The matching is performed in the same way that the matching to EM topo-clusters was performed, but using the super clusters instead. The reconstruction efficiency using super clusters for an electron is shown in Figure 3.20.

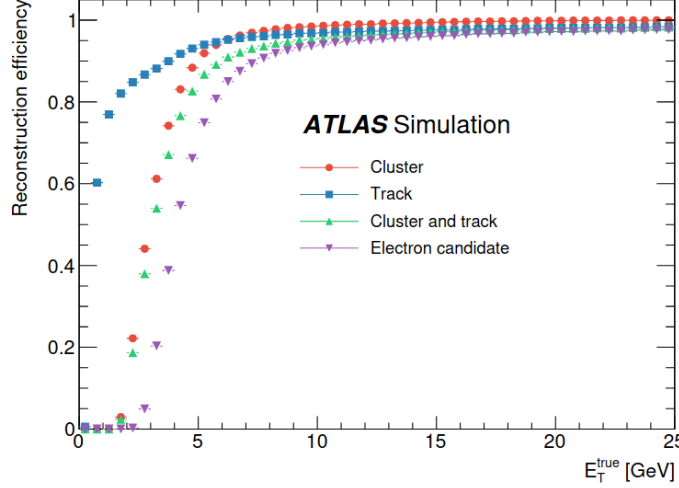


Figure 3.20: The cluster, track, cluster and track, and electron reconstruction efficiencies as a function of the generated electron E_T .

Figure 3.21 shows the reconstruction efficiency for converted photons as a function of the true E_T of the simulated photon for the previous version of the reconstruction software (fixed-size) and the current version (dynamic-size). An important reason for using super clusters is the improved energy resolution that super clusters provide by collecting more of the deposited energy **ADD PLOT OF ENERGY RESOLUTION COMPARISON**.

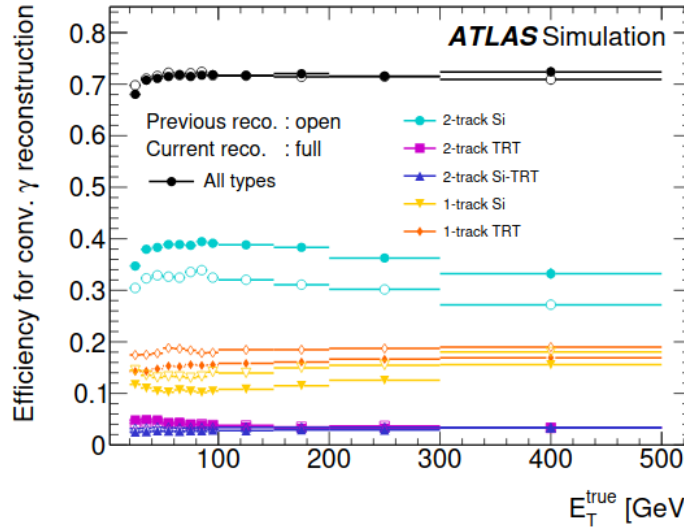


Figure 3.21: The converted photon reconstruction efficiency and contributions of the different conversion types as a function of E_T^{true}

Additionally, an ambiguity resolution is performed to remove a part of the overlap in case one object is reconstructed at the same time as electron and photon since electron and photon super clusters are built independently. However, in order to maintain a high reconstruction efficiency, a residual overlap is allowed, to allow physics analysis to define criteria based on their needs. Figure 3.22 shows the procedure used for ambiguity resolution.

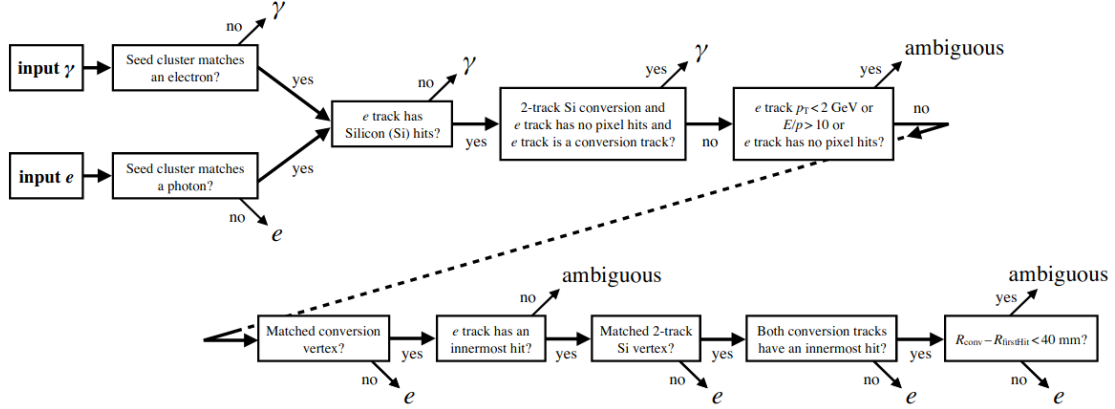


Figure 3.22: Flowchart showing the logic of the ambiguity resolution for particles initially reconstructed both as electrons and photons.

Most of LHC physics require the identification of prompt non-fake leptons and / or photons. Prompt particles are those not coming from a hadron or tau decay. Non-fake particles are those which type was properly reconstructed (*i.e.* a non-fake reconstructed electron is a true electron, not another mis-identified particle). Their identification and separation can be obtained with several selection criteria and algorithms. The identification for the reconstructed electrons and photons is finally based on the reconstructed super-cluster objects. A set of discriminating variables are calculated for the identification using cells in the fixed-size window. A list is given in Table 3.2 long with an indication if they are used for electron or photon identification. The prompt and non-fake leptons/photons are usually isolated, without much activity around them. It is therefore important to define a proper "isolation criteria" to reduce the contamination from non-prompt and fake objects. Electron isolation and identification are described in Sections 3.3.2.2 and 3.3.2.3 respectively, while Chapter 4 is dedicated to photon properties.

3.3.2.1 Electron and Photon calibration

After the electron and photon super clusters are built, an initial energy calibration and position correction is applied to them [63]. A complex chain with several successive calibration steps is used to calibrate the electron and photon energies based on simulation and well known reference processes. A schematic overview of the whole calibration chain is shown in Figure 3.23.

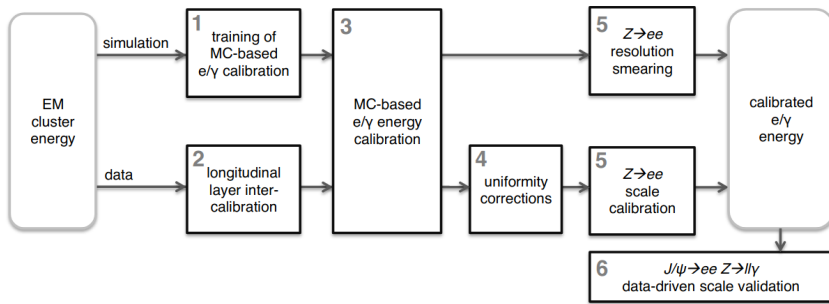


Figure 3.23: Schematic overview of the calibration chain for the electron and photon energies [64].

- Multivariate regression algorithm is trained on the properties of the shower development in the

Table 3.2: Discriminating variables used for electron and photon identification. The usage column indicates if the variables are used for the identification of electrons, photons, or both. [60].

Category	Description	Name	Usage
Hadronic leakage	Ratio of E_T in the first layer of the hadronic calorimeter to E_T of the EM cluster (used over the ranges $ \eta < 0.8$ and $ \eta > 1.37$)	R_{had_1}	e/γ
	Ratio of E_T in the hadronic calorimeter to E_T of the EM cluster (used over the range $0.8 < \eta < 1.37$)	R_{had}	e/γ
EM third layer	Ratio of the energy in the third layer to the total energy in the EM calorimeter	f_3	e
EM second layer	Ratio of the sum of the energies of the cells contained in a 3×7 ($\eta \times \phi$) rectangle (measured in cell units) to the sum of the cell energies in a 7×7 rectangle, both centred around the most energetic cell	R_η	e/γ
	Lateral shower width, $\sqrt{(\sum E_i \eta_i^2)/(\sum E_i) - ((\sum E_i \eta_i)/(\sum E_i))^2}$, where E_i is the energy and η_i is the pseudorapidity of cell i and the sum is calculated within a window of 3×5 cells	w_{η_2}	e/γ
	Ratio of the sum of the energies of the cells contained in a 3×3 ($\eta \times \phi$) rectangle (measured in cell units) to the sum of the cell energies in a 3×7 rectangle, both centred around the most energetic cell	R_ϕ	e/γ
EM first layer	Total lateral shower width, $\sqrt{(\sum E_i (i - i_{\text{max}})^2)/(\sum E_i)}$, where i runs over all cells in a window of $\Delta\eta \approx 0.0625$ and i_{max} is the index of the highest-energy cell	$w_{s \text{ tot}}$	e/γ
	Lateral shower width, $\sqrt{(\sum E_i (i - i_{\text{max}})^2)/(\sum E_i)}$, where i runs over all cells in a window of 3 cells around the highest-energy cell	w_{s3}	γ
	Energy fraction outside core of three central cells, within seven cells	f_{side}	γ
	Difference between the energy of the cell associated with the second maximum, and the energy reconstructed in the cell with the smallest value found between the first and second maxima	ΔE_s	γ
Track conditions	Ratio of the energy difference between the maximum energy deposit and the energy deposit in a secondary maximum in the cluster to the sum of these energies	E_{ratio}	e/γ
	Ratio of the energy measured in the first layer of the electromagnetic calorimeter to the total energy of the EM cluster	f_1	e/γ
Track–cluster matching	Number of hits in the innermost pixel layer	$n_{\text{innermost}}$	e
	Number of hits in the pixel detector	n_{Pixel}	e
	Total number of hits in the pixel and SCT detectors	n_{Si}	e
	Transverse impact parameter relative to the beam-line	d_0	e
	Significance of transverse impact parameter defined as the ratio of d_0 to its uncertainty	$ d_0/\sigma(d_0) $	e
	Momentum lost by the track between the perigee and the last measurement point divided by the momentum at perigee	$\Delta p/p$	e
Track–cluster matching	Likelihood probability based on transition radiation in the TRT	$e_{\text{ProbabilityHT}}$	e
	$\Delta\eta$ between the cluster position in the first layer of the EM calorimeter and the extrapolated track	$\Delta\eta_1$	e
	$\Delta\phi$ between the cluster position in the second layer of the EM calorimeter and the momentum-rescaled track, extrapolated from the perigee, times the charge q	$\Delta\phi_{res}$	e
	Ratio of the cluster energy to the measured track momentum	E/p	e

EM calorimeter to optimize the energy resolution and to minimize the impact of material in front of the calorimeter. The algorithm used in this step is the Boosted Decision Trees (BDTs) tuned in intervals of $|\eta|$ and E_T on samples of simulated single particles without pile-up, separately for electrons, converted and unconverted photons.

2. An inter-layer correction is applied to the relative energy response in data to match the relative response in MC in different calorimeter layers. The inter-layer calibration is independent from the material upstream of the calorimeter.
3. The BDTs correction is applied to both data and MC. This step performs the main correction of the absolute energy scale and improves significantly the energy resolution.
4. The non simulated detector non-uniformities are therefore corrected in data. Correcting the effects of energy loss between the barrel calorimeter modules and the high-voltage inhomogeneities.
5. Scale factors are applied to the energy in data to correct for the residual miscalibration between data and MC using $Z \rightarrow e^+e^-$ events.
6. The validity of the calibration is cross checked from data using different processes. For the low energy range $J/\Psi \rightarrow e^+e^-$ events are used. The calibration for photons is cross-checked using radiative $Z \rightarrow l^+l^-\gamma$ ($l = e, \mu$) decays.

3.3.2.2 Electron Isolation

The activity near leptons and photons can be quantified from the tracks of nearby charged particles or from energy deposits in the calorimeters, leading to two classes of isolation variables calorimeter based isolation E_T^{coneXX} and track-based p_T^{coneXX} [65]. The corrected E_T^{coneXX} is computed as the sum of the transverse energies of topo-clusters inside a cone of $\Delta R = \frac{XX}{100}$ around the reconstructed electrons, this is illustrated in Figure 3.24, after subtraction of the energy deposited by the electrons, pileup and underlying event [66]. The p_T^{coneXX} is computed by summing the transverse momentum of selected tracks of $p_T > 1$ GeV and $|\eta| < 2.5$, within a cone centred around the electron track. Tracks matched to the electron are excluded. In a high-momentum heavy particles decay, the electron is produced very close to other decay products, for this reason an isolation $p_T^{varconeXX}$ with a variable cone size ΔR^{XX} is defined the cone size shrinks for larger p_T electrons:

$$\Delta R^{XX} = \min\left(\frac{10}{p_T[\text{GeV}]}, \frac{XX}{100}\right). \quad (3.9)$$

Based on these variables, three different selection criteria, called working points (WPs), are implemented. The working points can be defined in two different ways, either targeting a fixed value of efficiency or with fixed cuts on the isolation variables. Table 3.3 lists the different electron-isolation WPs used in ATLAS.

WP	Calorimeter-based isolation	Track-based isolation
HighPtCaloOnly	$E_T^{cone20} < \max(0.015 \times p_T, 3.5 \text{ GeV})$	-
Loose	$E_T^{cone20}/p_T < 0.2$	$p_T^{varcone20}/p_T < 0.15$
Tight	$E_T^{cone20}/p_T < 0.06$	$p_T^{varcone20}/p_T < 0.06$

Table 3.3: Definition of the electron isolation working points.

An additional WP named Gradient is designed to give an efficiency of 90% at $p_T = 25$ GeV and 99% at 60 GeV, uniform in η . Figure 3.25 shows the electron isolation efficiency in data recorded in 2017

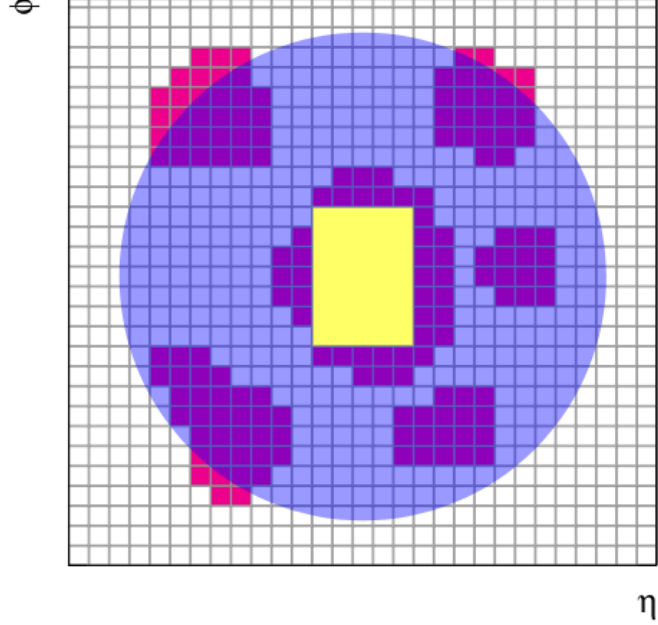


Figure 3.24: Schema of the calorimeter isolation method: the grid represents the second-layer calorimeter cells in the η and ϕ directions. The candidate electron is located in the centre of the purple circle representing the isolation cone. All topological clusters, represented in red, for which the barycentres fall within the isolation cone are included in the computation of the isolation variable. The 5x7 cells represented by the yellow rectangle correspond to the subtracted cells in the core subtraction method.

as a function of electron E_T [67]. The method used to compute the electron isolation efficiency and the associated uncertainties are described in Ref. [65]. The jump observed in Gradient efficiency at 15 GeV is due to the fact the the isolation efficiency is process dependent: the Gradient cut maps is optimized with $J/\Psi \rightarrow e^+e^-$ events below 15 GeV, while the efficiency measurement is performed with $Z \rightarrow e^+e^-$.

3.3.2.3 Electron Identification

The identification of prompt electrons relies on a likelihood (LH) discriminant constructed from quantities measured in the different sub-detectors and listed in Table 3.2. The electron LH is based on the products of the probability density functions (PDFs) for signal L_S , and for background L_B . The PDFs are created by smoothing histograms of the n discriminating variables with an adaptive kernel density estimator (KDE) [68] as implemented in TMVA [69] in 9 bins in $|\eta|$ and 7 bins of E_T :

$$L_{S(B)}(\mathbf{x}) = \prod_{i=1}^n P_{S(B),i}(x_i), \quad (3.10)$$

where \mathbf{x} is the vector of the various variables. For each electron candidate, a discriminant d_L is formed using an inverse sigmoid function transformation:

$$d_L = -\frac{1}{\tau} \ln\left(\frac{L_S + L_B}{L_S} - 1\right), \quad (3.11)$$

where τ is fixed to 15 [69]. Figure shows the an example of the distribution of the transformed discriminant for prompt electrons and for non-prompt one. This distribution illustrates the effective separation between signal and background encapsulated in this single quantity.

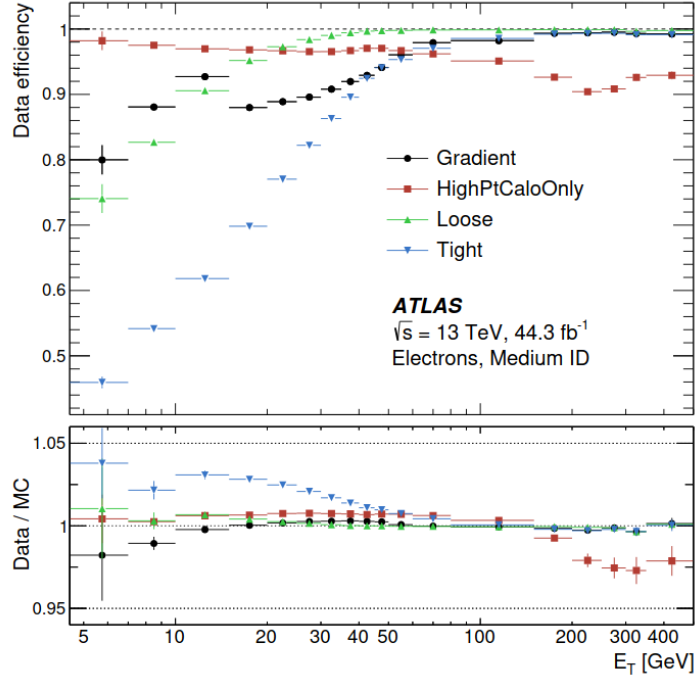


Figure 3.25: Efficiency of the different isolation working points for electrons from inclusive $Z \rightarrow e^+e^-$ events as a function of the electron E_T . The lower panel shows the ratio of the efficiencies measured in data and in MC simulations [67].

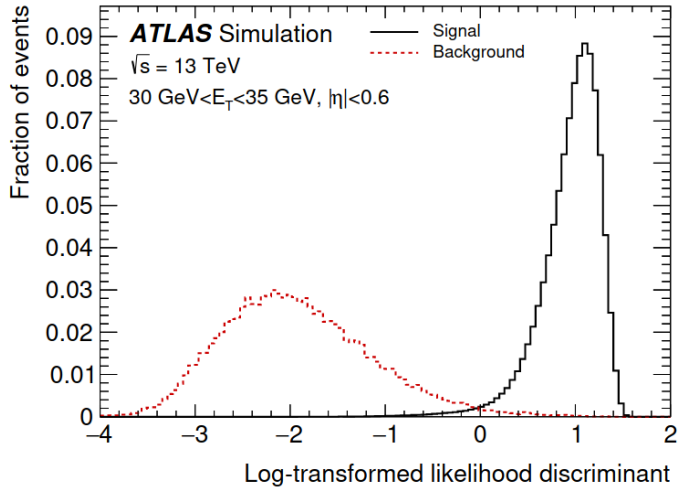


Figure 3.26: The transformed LH-based identification discriminant d_L for reconstructed electron candidates with good quality tracks with $30 < E_T < 35$ GeV and $|\eta| < 0.6$ [70].

For physics purposes three WPs are defined. These operating points are referred to as Loose, Medium, and Tight. The efficiency for identifying a prompt electron with $E_T = 40$ GeV are 93%, 88% and 80% for the Loose, Medium and Tight. Figure 3.27 shows the resulting efficiencies in data [60].

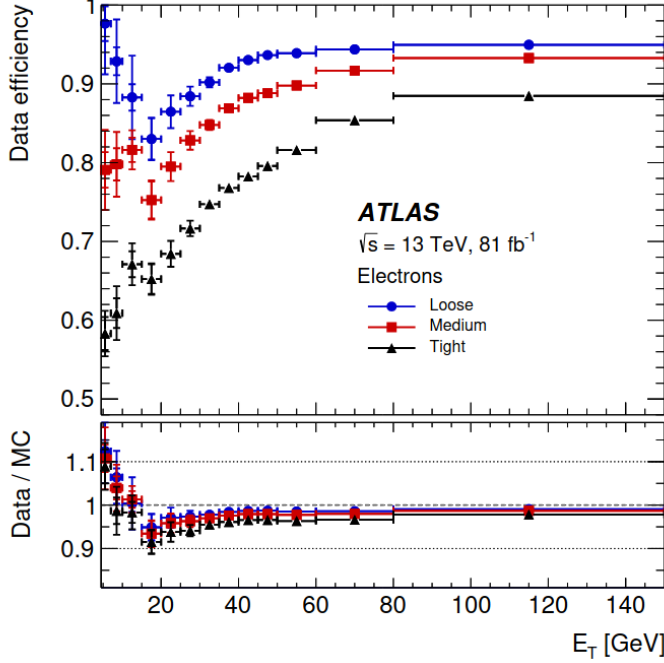


Figure 3.27: The electron identification efficiency in $Z \rightarrow e^+e^-$ events in data as a function of E_T for the Loose, Medium and Tight operating points.

3.3.3 Muon reconstruction and identification

3.3.3.1 Muon reconstruction

Muons are the only charged particles leaving the calorimeter system. Muon reconstruction is performed in two sub-detectors independently. Firstly, the muon tracks are reconstructed in the ID like any track as described in Section 3.3.1. Then, the ID reconstruction is combined with the muon reconstruction in MS sub-detector to perform the muon object used in physics analysis. In the MS, the muons are triggered in RPC/TGC if at least one hut exists, defining the region of activity (ROA). All the muon chambers intersecting with the ROA are then selected as muon track candidates. The MDT segments are reconstructed by performing a straight-line fit (the bending of muons $>$ few GeV is sufficiently small) to the hits found in each layer [71]. The fitted segments are required to point loosely towards the IP, in order to reject background events and random hit combinations. Muon track candidates are then built by extrapolation each of these segments to the other. At least two matching segments using their relative positions and angles are required to build a track, except in the barrel–endcap transition region where a single high-quality segment can be used.

The combined reconstruction is performed according to various algorithms based on the provided information by sub-detectors [72, 73]:

- Combined (CB) muon: the combined muon is formed with a global refit that used the hits from both the ID and MS sub-detectors. The reconstruction is done following two complementary approaches, the outside-in in which the reconstructed track in the MS are extrapolated inward and match to an ID track, and the inside-out reconstruction, in which ID tracks are extrapolated outward and matched to MS tracks.

- Segment-tagged (ST) muon: ST muons are used when muons cross only one layer MS chamber, either because of their low p_T or because of MS acceptance.
- Calorimeter-tagged (CT) muon: reconstructed track with an energy deposit in the calorimeter compatible with a minimum-ionizing particle is identified as CT muon.
- Extrapolated (ME) muon: ME muons are reconstructed based only on the MS track and a loose requirement on compatibility with originating from the IP.

Overlaps between different muon types are resolved with preference to CB, ST and CT muons respectively before producing the collection of muons used in physics analyses.

3.3.3.2 Muon identification

In order to suppress muons coming from background, mainly pion and kaon decays, and select prompt muons, a muon identification is performed. Muon identification uses several variables, for CB tracks, the variables used are:

- q/p significance defined as :

$$q/p \text{ significance} = \frac{|q/p_{\text{ID}} - q/p_{\text{MS}}|}{\sqrt{\sigma^2(q/p_{\text{ID}}) + \sigma^2(q/p_{\text{MS}})}}, \quad (3.12)$$

where q/p_{ID} and q/p_{MS} are the measurements in the ID and MS of the ratio of the charge q to the momentum p of the muon, expressed at the IP and σ is the corresponding uncertainties.

- ρ' , defined as the absolute value of the difference between the transverse momentum measurements in the ID and MS divided by the p_T of the combined track.
- Normalised χ^2 of the combined track fit.

Four muon identification WPs are provided to address specific needs of different physics analysis:

- *Loose* : identification criteria are designed to maximise the reconstruction efficiency while providing good-quality muon tracks. They are specifically optimised for reconstructing Higgs boson candidates in the four-lepton final state [74].
- *Medium* : identification criteria provide the default selection for muons in ATLAS. This selection minimises the systematic uncertainties associated with muon reconstruction and calibration. Only CB and ME tracks are used. About 0.5% of Medium muon originate from the inside-out reconstruction strategy, in the central region.
- *Tight* : muons are selected to maximise the purity of muons at the cost of some efficiency. Only CB muons with hits in at least two stations of the MS and satisfying the *Medium* selection criteria are considered.
- *High- p_T* : selection aims to maximise the momentum resolution for tracks with transverse momentum above 100 GeV. The selection is optimised for searches for high-mass Z' and W' resonances [75, 76]. CB muons passing the *Medium* selection and having at least three hits in three MS stations are selected.

Figure 3.28 shows the muon reconstruction and identification efficiency for *Loose*, *Medium* and *Tight* muons as measured in $J/\Psi \rightarrow \mu\mu$.

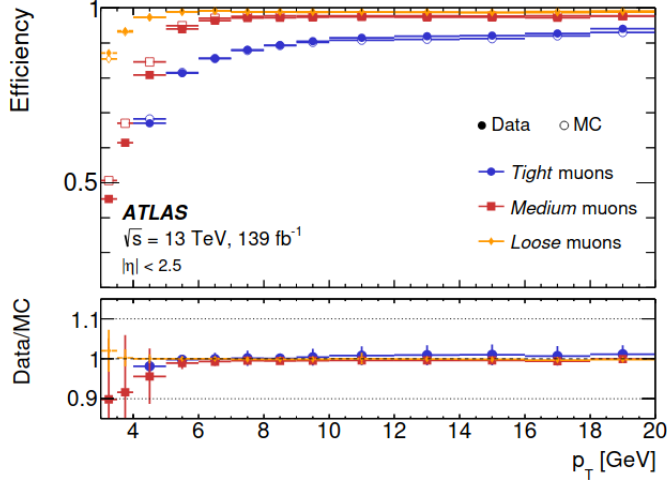


Figure 3.28: Muon reconstruction and identification efficiencies for the *Loose*, *Medium* and *Tight* criteria as function of p_T . The panel at the bottom shows the ratio of the measured to predicted efficiencies, with statistical and systematic uncertainties.

3.3.4 Jet reconstruction

Jets are made of a large number of partons coming from the initial quark or gluon hadronisation, appearing in the detector as a collimated shower. Many jets reconstruction algorithms exists, only two approaches are of interest for the work presented in this thesis. The first approach is based exclusively on electromagnetic and hadronic topological clusters, so-called EMTopo jets. The second approach uses both tracking and calorimetric information through a Particle Flow algorithm to build PFlow jets [77]. Jets are identified using the anti- k_t algorithm [78], with a distance parameter $R=0.4$. Jets reconstruction and calibration will be discussed in Chapter 5.

3.3.5 Missing transverse energy

Neutrinos and other BSM particles interact extremely weakly with matter, making them hard to detect and they cannot be observed directly as hadrons, electrons or muons discussed before. Their energy is reconstructed as missing transverse energy (MET). Thanks to momentum conservation, the transverse momentum of all particles generated in a collision should sum up to zero, since the original transverse momentum of the partons is negligible. MET is defined as the sum of the transverse energy momenta of all reconstructed objects i :

$$\vec{E}_T^{miss} = - \sum_i \vec{p}_T^i \quad (3.13)$$

Photons in ATLAS

Photons are crucial to study the $HH \rightarrow \gamma\gamma b\bar{b}$ properties. They are reconstructed similarly to electrons as introduced in Section 3.3.2, and their energy is calibrated in the same way. This chapter gives more details about photon identification and isolation. A new photon identification algorithm with a neural network (NN) will be introduced.

This include :

- Introduction to electromagnetic objects and shower
- Photon reconstruction
- Photon Isolation
- Photon identification (Run 2 cut based)
- Shower shape mis-modelling
- Convolutional Neural Network for photon identification

4.1 Photons Isolation

Photon isolation and different isolation WPs will be discussed here.

Photon isolation is almost similar to the one from electrons (Section 3.3.2.2). However, photon isolation uses different requirements to define three WPs. Table 4.1 summarizes the defined operating points [67].

WP	Calorimeter-based isolation	Track-based isolation
Loose	$E_T^{cone20} < 0.065 \times E_T$	$p_T^{varcone20}/E_T < 0.05$
Tight	$E_T^{cone40} < 0.022 \times E_T + 2.45 \text{ GeV}$	$p_T^{varcone20}/E_T < 0.05$
TightCaloOnly	$E_T^{cone40} < 0.022 \times E_T + 2.45 \text{ GeV}$	-

Table 4.1: Definition of the photon isolation working points.

A discrepancy between the peak positions of the simulated and real distributions of the calorimeter-based variables is observed since Run 1 [79], pointing to a mismodelling of the lateral profile development of the electromagnetic showers and results in different isolation efficiency in data and simulations and large scale factors. A data-driven shift is applied to handle the mismodelling in simulation. The shifts values are defined by the difference in the peak values between data and simulation from a fit. The fit is performed using the Crystal Ball pdfs [80] on the E_T^{cone40} and E_T^{cone20} variables in bin of η , E_T and conversion type

(Converted or Unconverted) separately. The resulting shift are then added to simulation. Figure 4.1 shows the distribution of E_T^{cone40} after the data-driven shifts applied.

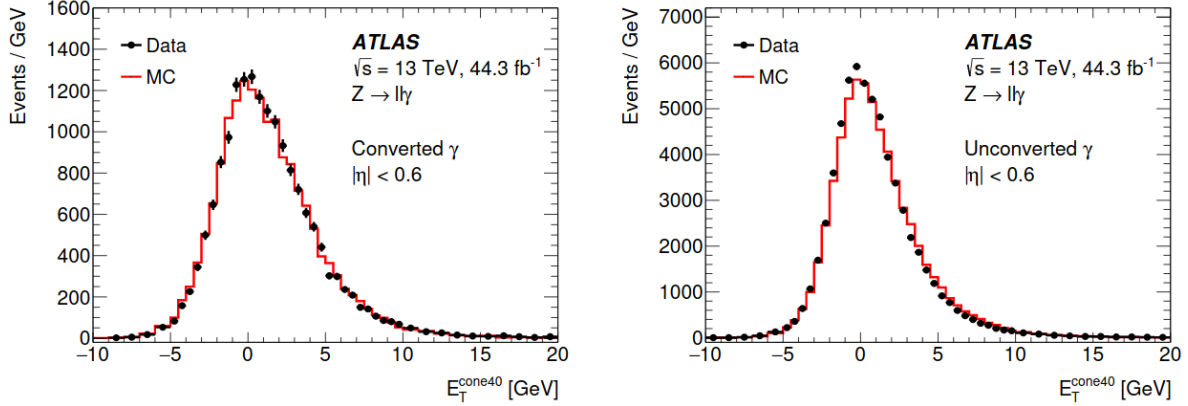


Figure 4.1: Distribution of E_T^{cone40} in data and simulation, in the central region of the detector ($|\eta| < 0.6$), separately for converted (left) and unconverted (right) photons after the data-driven shifts are applied.

Figure 4.2 shows the efficiency of the isolation working points defined in Table 4.1, using $Z \rightarrow ll\gamma$ ($l = e, \mu$). The radiative Z decays signature is used to estimate the photon efficiencies since it provides a clean environment of prompt photons, especially in the low- E_T range.

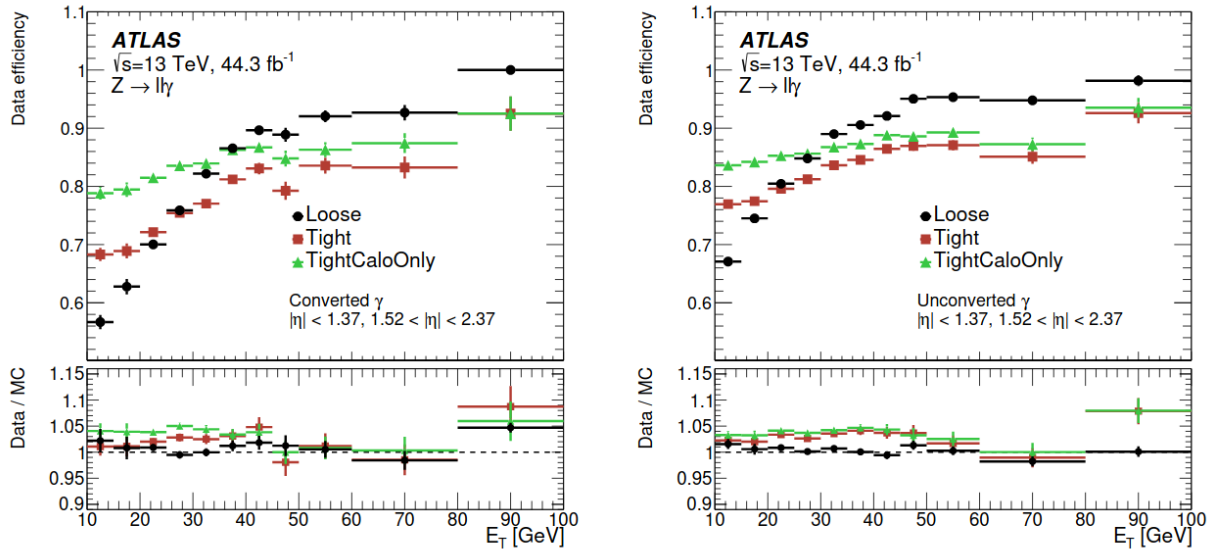


Figure 4.2: Efficiency of the isolation working points for converted(left) and unconverted (right) photons as a function of photon E_T . The lower panel shows the ratio of the efficiencies measured in data and in simulation (scale factors).

4.2 Photons Identification

The identification algorithm will be discussed here, and how the shower shape mis-modelling is affecting the ID efficiency.

In contrary to electron identification, photon identification lies on rectangular selection criteria, *cut-based algorithm*, using a set of global variables which characterize the lateral and longitudinal electromagnetic shower development in the calorimeter and encode separation between prompt-photons and fake photons originating from the decay of QCD jets. Such variables, listed in Table 3.2 and depicted in Figure 4.3 with their respective definitions, are called shower shapes. Shower shapes from the first EM layer play a significantly important role in rejecting the collimated photons from $\pi^0 \rightarrow \gamma\gamma$ decay.

The cut-based algorithm provides three WPs: Tight, Medium and Loose, with less restrictive selections

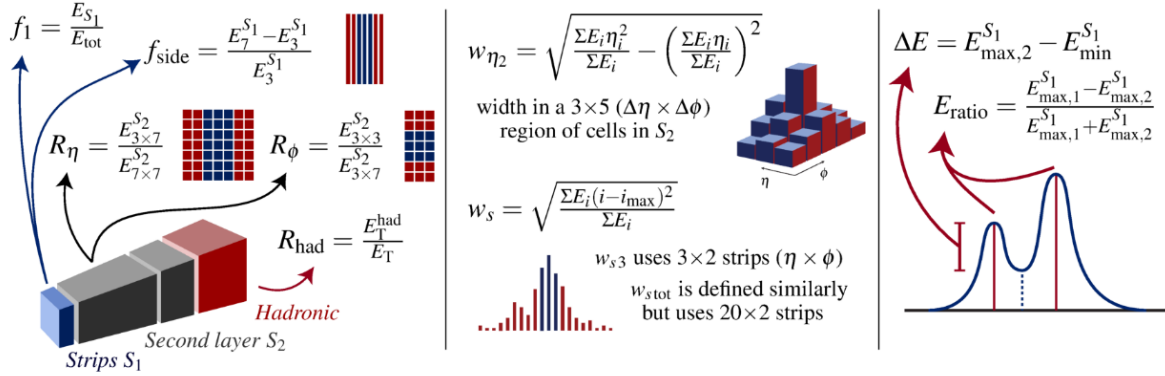


Figure 4.3: Schematic representation of the photon identification discriminating variable [81].

respectively. The Medium and Loose WPs mainly used for Trigger purposes, and since the trigger system is transparent between converted and unconverted photons, they are similar for both converted and unconverted. Table 4.2 lists the variables set used in each WP. The optimization of the WPs is done using TMVA [69] in bins of $|\eta|$ since the shower shapes vary due to calorimeter granularity. Because the shower shapes are different between the converted and unconverted photons due to the opening angle of the e^+e^- conversion pair and the material interaction, the optimization of Tight WP is preformed separately for converted and unconverted photons. The Tight WP comes with two versions: E_{T} -independent selection and the E_{T} -dependent tuned in separate bins of E_{T} . The tuning is done in two energy regimes with two different series of MC dataset. For photon with $10 < E_{\text{T}} < 25$ GeV, the $Z \rightarrow ll\gamma$ MC sample is used to define the signal, while the corresponding background is derived from the $Z \rightarrow ll + jets$ MC sample. Above $E_{\text{T}} = 25$ GeV, the inclusive-photon production MC sample is used as a signal, and the background is the dijet. The MC samples are described in Section 3.1 and 3.2 of Ref. [67].

Working Point	Variables set
Loose	$R_{\text{had}}, R_{\text{had}_1}, R_\eta$ and w_{η_2}
Medium	Loose + E_{ratio}
Tight	Medium + $R_\phi, w_{s,3}, w_{s,\text{tot}}, f_{\text{side}}, \Delta E$ and f_1

Table 4.2: Discriminating variables used for Loose, Medium and Tight photon identification.

Similarly to the calorimeter based variables for isolation, the shower shapes variables suffer from the mis-modelling of the EM shower. The mis-modelling is addressed using a data-driven correction similar to the one applied for isolation features. Corrections are applied as a simple shift to MC values to align with the real data distributions. Shifts are derived using a χ^2 minimization between the data and MC in bins of $|\eta|$ and E_{T} as described in Ref [82]. Figure 4.4 shows examples of the shower shapes distributions

before and after correction compared to the real distributions using radiative Z photons. Section 4.3 is dedicated to the shower shape mis-modelling and its correction using an alternative method. The photon

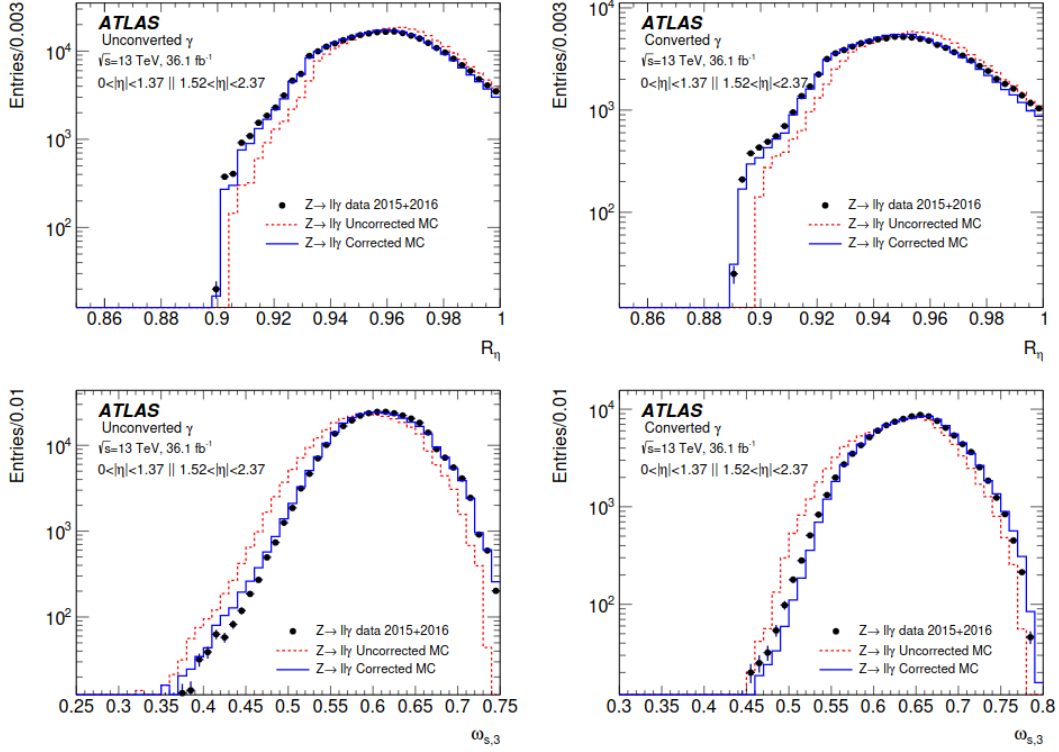


Figure 4.4: Distributions of the R_η and $w_{s,3}$ for converted and unconverted photon candidates with E_T in [10,50] GeV and $|\eta| < 2.37$ selected from radiative Z events for data (black), uncorrected MC (dashed red line) and the corrected MC (solid blue line).

identification efficiency is measured using three different methods over distinct energy regimes:

- The Matrix Method (MM) uses the inclusive-photon production sample collected using single-photon triggers and performed over a wide kinematic range from 25 GeV and up to 1.5 TeV.
- The Radiative Z method uses the clean signature of radiative Z at low-energy, allows a measurement of identification efficiency ϵ_{ID} from $E_T = 10$ GeV up to 100 GeV. This method handles small background contamination from Z+jets where the jet is misidentified as photon using a maximum-likelihood fit [83].
- Electron Extrapolation (EE) is the third method, uses a transformed electrons shower shapes sample from $Z \rightarrow e^+e^-$ and measures ϵ_{ID} in the region $25 < E_T < 150$ GeV.

These methods are fully described in Section 5 of Ref. [82]. The efficiencies from each method are then combined to provide a ϵ_{ID} measurement for the E_T -dependent selection as shown in Figures 4.5 and 4.6. A comparison between the two version of the Tight WP is shown in Figure 4.7. **The pile-up effect can fit with the CNN part**

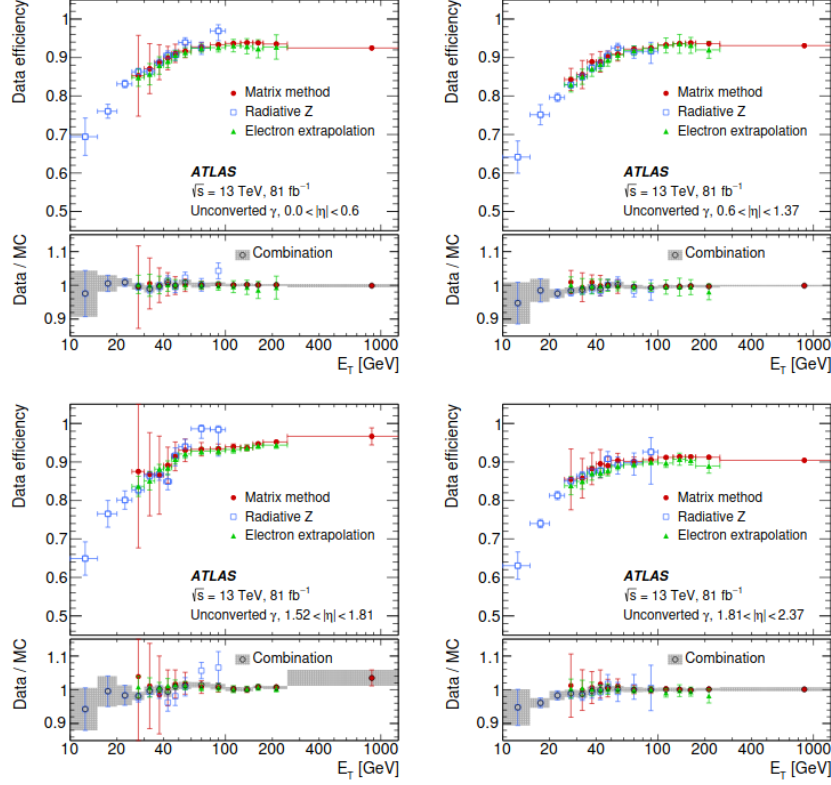


Figure 4.5: The photon identification efficiency with E_T -dependent selection, and the ratio of data to MC efficiencies, for unconverted photons with a Loose isolation requirement applied as pre-selection, as a function of E_T in four different $|\eta|$ regions. The combined scale factor, obtained using a weighted average of scale factors from the individual measurements, is also presented; the band represents the total uncertainty.

4.3 Shower shape mis-modelling

The QT work will fit here.

The source of the disagreement in shower shapes between the data and MC described above is remaining not clear. Many sources contribute to this mis-modelling, mainly from the detector geometry, material distribution and EM shower modelling. It is hard to handle those sources and fix the mis-modelling. Indeed a cell-based reweighting method has been developed for electrons to apply a global correction. The approach shows a promising electron result, which makes its application also interesting to photons. This work is done in the context of ATLAS qualification task for ATLAS authorship.

4.3.1 Cell-based reweighting correction

The aim is to redistribute the energy between the cluster cells in MC to becomes consistent with the data. The cell-based reweighting is derived for the second layer of the EM calorimeter. A cluster of 7×11 (7 cells in η and 11 cells in ϕ) centred around the cell with the highest energy (hottest) is considered. The correction is derived as a matrix (7×11) in bins of η in two steps:

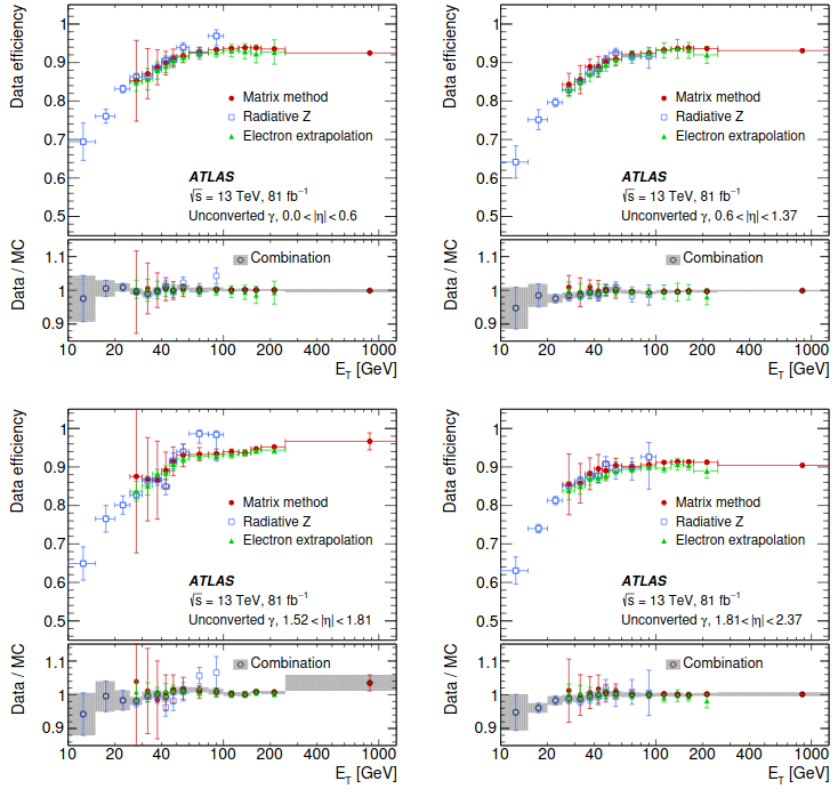


Figure 4.6: The photon identification efficiency with E_T -dependent selection, and the ratio of data to MC efficiencies, for converted photons with a Loose isolation requirement applied as pre-selection, as a function of E_T in four different $|\eta|$ regions. The combined scale factor, obtained using a weighted average of scale factors from the individual measurements, is also presented; the band represents the total uncertainty.

1. Compute single cell corrections as :

$$M_i^{Correction} = \frac{E_i^{data}}{\sum E_i^{data}} - \frac{E_i^{MC}}{\sum E_i^{MC}}. \quad (4.1)$$

Where $E_{i=1..77}$ denotes the cell energy in the 7x11 cluster of layer 2.

2. Compute the reweighted energy for each cluster cell as :

$$E_i^{Reweighted} = E_i^{non-reweighted}(1 + M_i^{Correction}). \quad (4.2)$$

The main idea behind the reweighting is to factorize out the material effects and not the physics behaviours, especially the Bremsstrahlung tails in the energy profile for electrons and positrons. For electron only, the bremsstrahlung tails are extracted from the e^+ and e^- energy profiles as:

$$E_i = (E_i^{electron} < E_i^{positron}) ? E_i^{electron} : E_i^{positron}, \quad (4.3)$$

so it is derived independent from bremsstrahlung and similar for both electrons and positrons.

4.3.2 Electron results

Figure 4.8 shows a reduction in data-MC discrepancy after the reweighting and leads on a similar distribution for shower shape computed from layer 2 (R_η and R_ϕ) between data and MC. The cell-based reweighting

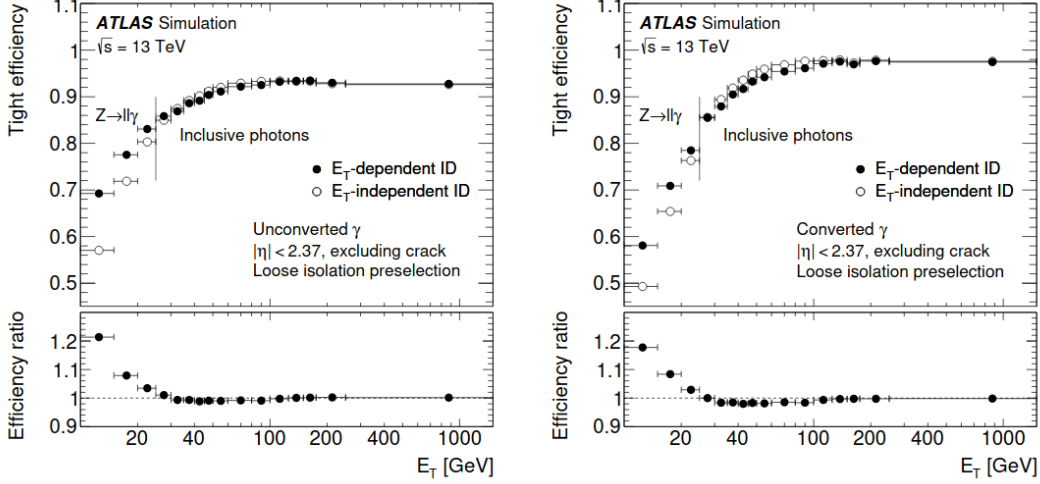


Figure 4.7: Efficiencies of the Tight photon identification for unconverted (left) and converted (right) signal photons, plotted as a function of photon E_T . The Loose isolation is applied as a pre-selection. For both plots, the bottom panel shows the ratios between the E_T -dependent and the E_T -independent identification efficiencies.

seems to be promising to reduce data-MC mis-modelling on electrons shower shapes. Applying the same strategy to photons is interesting.

4.3.3 Cell-based reweighting for photons

4.3.3.1 Event selection

For this study, we have considered photon from the $Z \rightarrow ll\gamma$. The criteria used for selection is the following:

1. Photon selection :
 - Transverse momentum $p_T > 10$ GeV.
 - Pseudorapidity $|\eta|$ within the calorimeter acceptance : $|\eta| < 2.37$, excluding the transition region between the barrel and end-cap (crack region) : $1.37 < |\eta| < 1.52$
 - Isolation : Tight WP.
 - Identification : Non.
2. Electron selection :
 - Transverse momentum $p_T > 10$ GeV.
 - Pseudorapidity $|\eta| < 1.37$ or $1.52 < |\eta| < 2.47$.
 - Longitudinal impact parameter $z_0 < 10$ mm, transverse impact parameter significance $|d_0|/\sigma_{d_0} < 10$.
 - Isolation : Loose WP.
 - Identification : Medium.
3. Combined Muon selection :

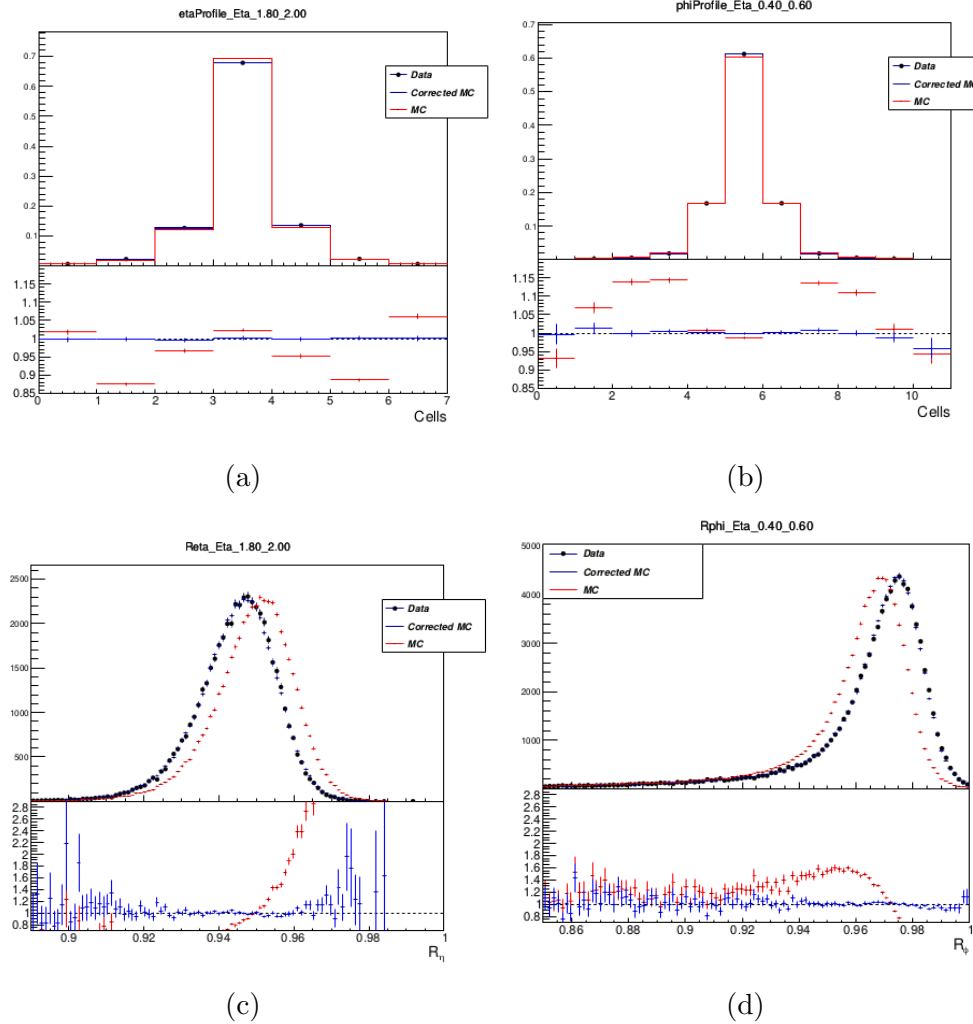


Figure 4.8: (a) Energy profile in η direction, (b) Energy profile in ϕ direction, (c) R_η variable and (d) R_ϕ variable before (red) and after reweighting for electrons from $Z \rightarrow e^+e^-$ for $1.80 < |\eta| < 2.00$ first column and $0.40 < |\eta| < 0.60$ in the second column (the bottom plot is the data/MC ratio).

- Transverse momentum $p_T > 10$ GeV.
 - Pseudorapidity $|\eta| < 2.5$.
 - Longitudinal impact parameter $z_0 < 10$ mm, transverse impact parameter significance $|d_0|/\sigma_{d_0} < 10$.
 - Isolation : Loose WP.
 - Identification : Medium WP.

4. $Z \rightarrow ll\gamma$ event selection :

- $\Delta R_{min}(e, \gamma) > 0.4$ and $\Delta R_{min}(\mu, \gamma) > 0.2$: the selection is tighter for electron channel to reduce the $e \leftrightarrow \gamma$ misidentifying.
 - $80 < m_{ll\gamma} < 100$ GeV to select Z peak, and $40 < m_{ll} < 83$ GeV for final state radiation (FSR) event selection.

No identification criteria is applied to photons to remove any bias from the identification. The SHERPA generator is used for MC samples while the data correspond to the 2017 proton-proton collisions.

4.3.3.2 Electrons reweighting applied to photons

The developed reweighting matrix for electrons is directly applied to the selected photons from radiative Z events. Figure 4.9 shows the energy profiles and layer 2 shower shapes variables before and after the reweighting. The reweighting seems to go in the correct direction but not enough to correct photons shower shape mis-modelling; this motivates to drive specific reweighting for photons. Additional control plots for other η regions and converted photons are provided in Appendix () .

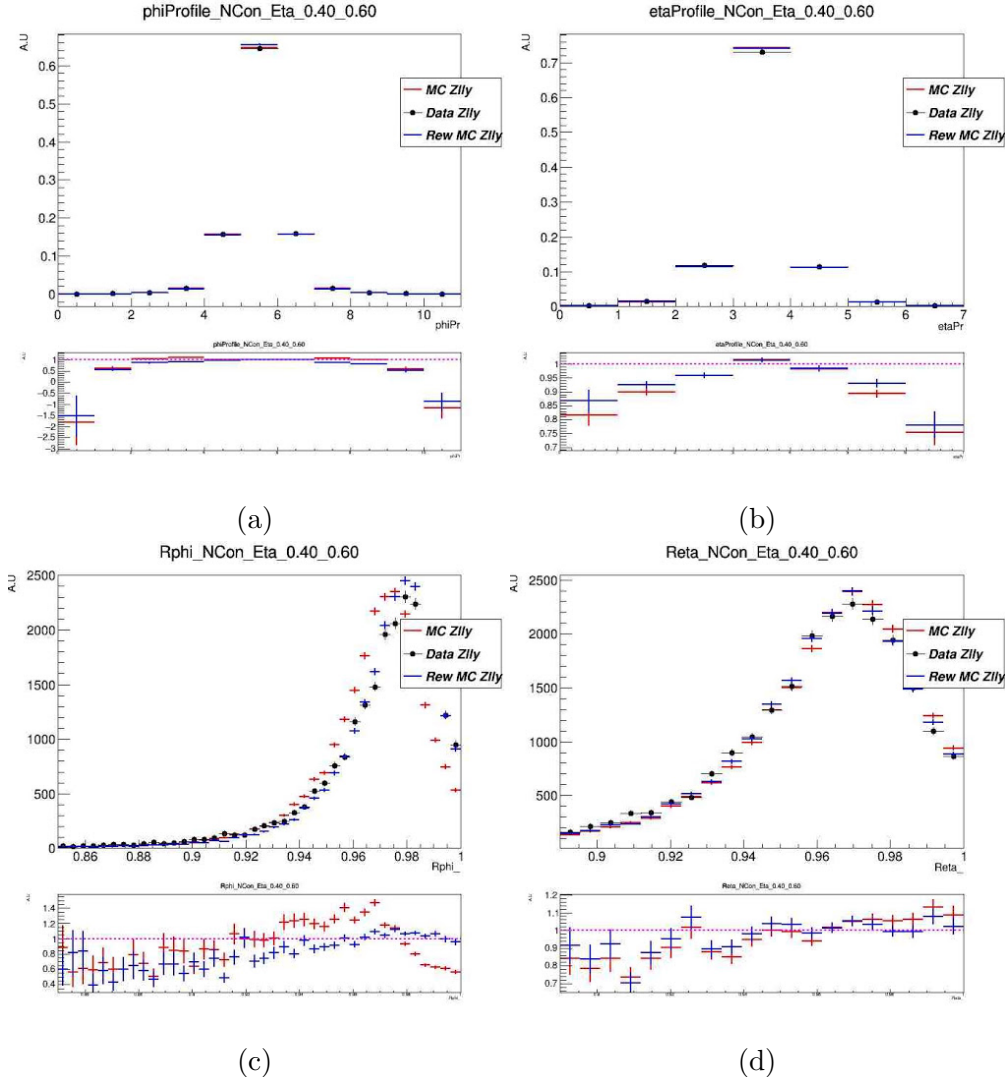


Figure 4.9: The energy profile in ϕ and η directions (a,b) and the corresponding R_ϕ and R_η variables, for unconverted photons with $0.40 < |\eta| < 0.60$. The black points correspond to Data 2017, red points to non-reweighted MC and blue points to the reweighted MC from $Z \rightarrow ll\gamma$.

4.3.3.3 Photon reweighting

Similarly to electrons, the reweighting is recomputed for photons using radiative Z events inclusively in conversion to allow for more statistics. Figure 4.10 shows the profiles and shower shapes after applying the derived reweighting on photons. A good agreement is observed in energy profiles for both direction η and ϕ . However for shower shapes variables, no significant improvement is observed and the reweighting seems to be not working for photons. Additional control plots for other η regions and converted photons are provided in Appendix (). To validate the reweighting procedure a closure test is performed on pseudo data.

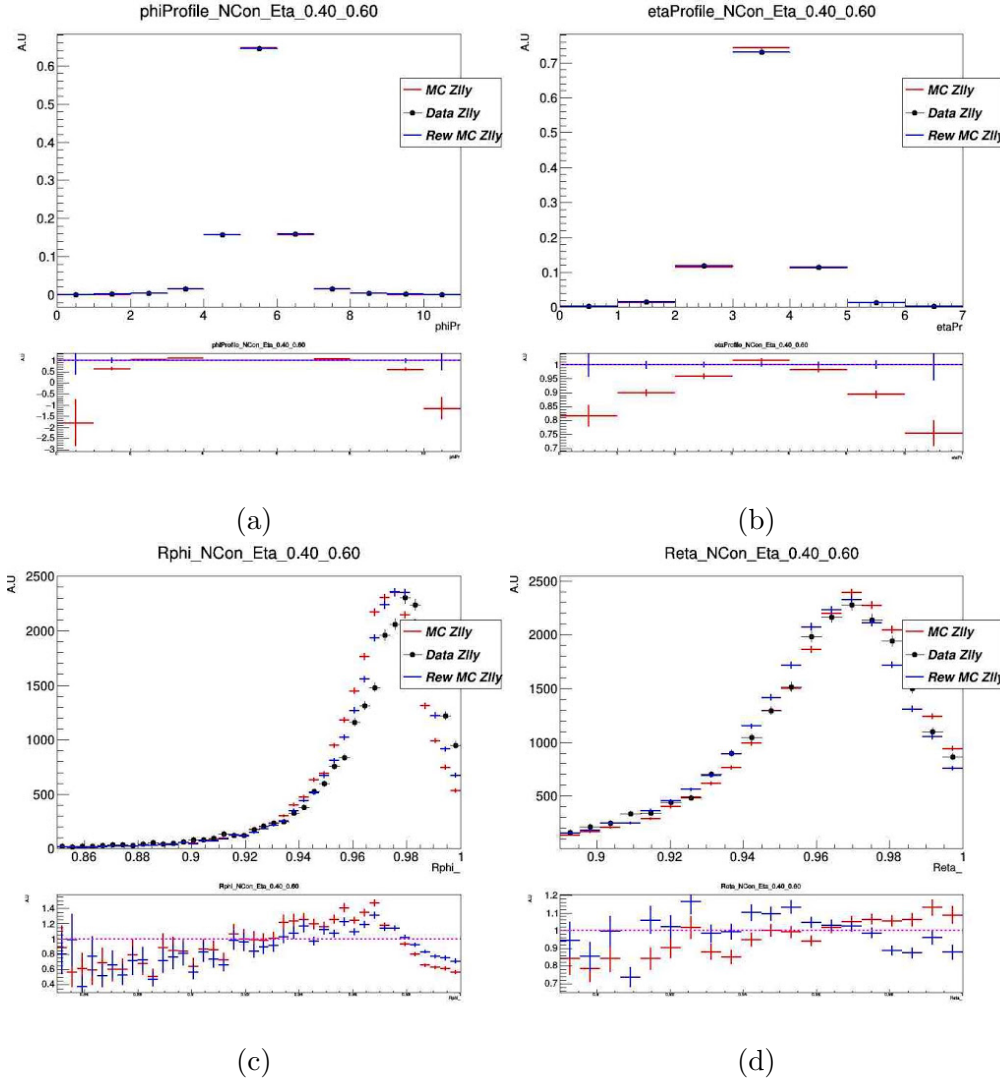


Figure 4.10: The energy profile in ϕ and η directions (a,b) and the corresponding R_ϕ and R_η variables, for unconverted photons with $0.40 < |\eta| < 0.60$. The black points correspond to Data 2017, red points to non-reweighted MC and blue points to the reweighted MC from $Z \rightarrow ll\gamma$.

4.3.3.4 Closure test

To test if the reweighting procedure can handle the discrepancy between data and MC. A closure test is preformed using pseudo data (PS) from MC, for that :

1. Pseudo data is produced by adding 50 MeV (arbitrary value) to each MC cells.
2. Re-compute the reweighting function with the same procedure as above using unconverted photons (for simplicity).
3. Correct MC cell to match the pseudo data.

Results of the closure test are shown in Figure 4.11. Perfect agreement in energy profiles for both directions

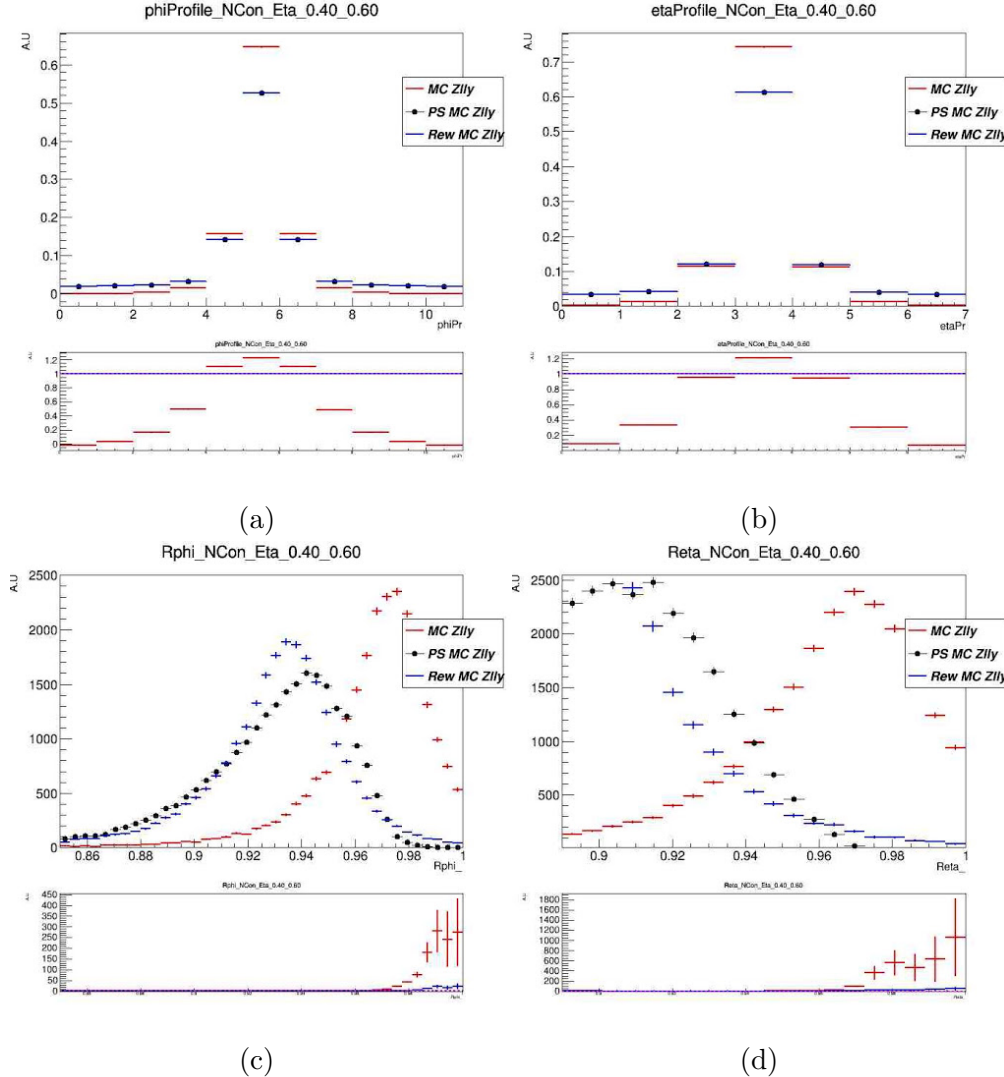


Figure 4.11: The energy profile in ϕ and η directions (a,b) and the corresponding R_ϕ and R_η variables, for unconverted photons with $0.40 < |\eta| < 0.60$. The black points correspond to the pseudo data, red points to non-reweighted MC and blue points to the reweighted MC from $Z \rightarrow ll\gamma$.

$(\eta$ and $\phi)$ is observed, the closure test reproduces the pseudo data, while for shower shapes the agreement is improved in the correct direction but not enough to correct the fake mis-modelling. The closure test shows that the reweighting procedure was not able to catch the discrepancy between data and MC, and seems to be working only on average and not event-by-event. Table ?? shows the averages of R_η and R_ϕ in real data, MC and after reweighting in bin of photon η . After reweighting, the average of shower shapes in MC perfectly matches the data distribution, which demonstrates that the reweighting is working on average and not event-by-event.

4.3.3.5 3-dimensional reweighting

Since the reweighting is only working on average and not event-by-event, a new reweighting technique is presented here. The idea is to add cell energy as a dimension to the previous reweighting procedure. The reweighting factor for each cell will be a function of cell energy. Instead of 2D reweighting the reweighting will be in 3 dimensions, defined as:

$$E_{k,n}^{Rew} = E_{k,n} \times \alpha ; \text{with } \alpha = f(k, n, E_{k,n}) = E_{k,n}^{Data} / E_{k,n} \quad (4.4)$$

Where $k = 1..77$ denotes the cell number, n the corresponding photon $|\eta|$ bin and $E_{k,n}$ is the energy of cell k in η bin n .

The new method needs a perfect matching between photons from data and MC to compute the α factors, which is technically complicated. The procedure is tested with PS data from MC. The PS data is derived from MC by scaling the energy of cell k by $0.26 \times k$ (the factor 0.26 is arbitrary). For simplicity, the reweighting is evaluated using unconverted photons only. The result of the new reweighting procedure is presented in Figure 4.12. A good agreement is observed after the 3D reweighting for both energy profiles and their corresponding shower shapes variables for layer 2. The improvement in data-MC agreement observed makes the new method promising to be applied to real data. This work is kept for the newcomers to the ATLAS collaboration.

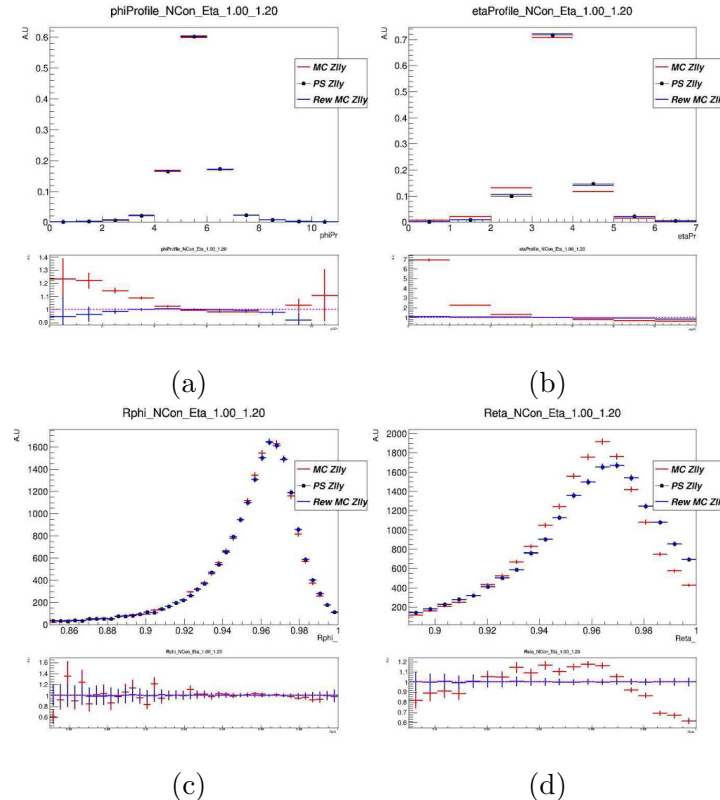


Figure 4.12: The energy profile in ϕ and η directions (a,b) and the corresponding R_ϕ and R_η variables, for unconverted photons with $1.00 < |\eta| < 1.20$. The black points correspond to the pseudo data, red points to non-reweighted MC and blue points to the reweighted MC from $Z \rightarrow ll\gamma$.

4.4 Convolutional Neural Network for Photon Identification

The CNN work will fit here to improve the photon identification efficiency and if scale factor are ready by the date of the thesis will be included to.

The shower shapes variables used for the identification algorithm limit its performance to learn the shower difference between prompt and fake photons. Correcting the mis-modelling seems to be a critical problem without any solution at the moment. Given these reasons, a significant improvement is possible to achieve by developing a new identification algorithm based on the EM cells and using advance Machine Learning (ML) techniques. The EM cells of the photon cluster are commonly represented as an image, where each pixel contains the cell energy, leading to use of images of the deposited energy of the photon in the calorimeter to learn the shower properties. The most adapted ML technique for image processing is Convolutional Neural Networks (CNNs). In the following, we describe how we develop a CNN algorithm to improve the photon identification efficiency using EM calorimeter images. This section assumes knowledge of the NNs system from the reader.

4.4.0.1 Event selection

Monte Carlo samples of inclusive photon production are used to train the CNN. The inclusive photon sample includes $\gamma + \text{jet}$ events from the hard subprocesses $qg \rightarrow q\gamma$ and $q\bar{q} \rightarrow g\gamma$, and it is enriched by prompt photon used as a signal for the training, while photon production from quark fragmentation in QCD di-jet events is enriched by background photons. Photons candidates are requested to pass the same photon selection defined for radiative Z in Section 4.3.3.1. Additionally, photons used as a signal in the training (prompt) are required to be a stable particle, not originating from a hadron and match a truth photon, photons fail one of these requirements are used as a background (fake). Photons from radiative Z decay are used as a control sample to evaluate the performance of the trained model on unseen photon (out-of-sample validation). The selected events are splitted for training (50%), validation (25%) and testing (25%).

4.4.0.2 Images pre-processing

To compromise between collecting more energy and being in-affected by the activity around the cluster, the 7x11 cluster around the hottest cell is considered similarly to the shower shapes computation. As the EM cell granularity changes with η (Table 3.1), it leads to different number of cells in each η region and different sizes. The corresponding number of cells in 7x11 windows are summarized in Table 4.3.

$ \eta $ range	0 to 1.4	1.4 to 1.8	1.8 to 2.0	2.0 to 2.5
Sampling 1	112	112	84	56
Sampling 2	77	77	77	77
Sampling 3	44	44	44	44

Table 4.3: Number of cells in 7x11 EM calorimeter windows.

The difference in shape and size of the EM calorimeter windows complicates the network training procedure. To avoid this issue, zeros are appended to the calorimeter cluster image to end up with the same shape in all η region for each sampling (e.g sampling 1 with 84 cells is completed by zeros, to have 112 cells). Table 4.4 shows the final image shape used for each sampling.

Sampling	Shape
Sampling 1	(56,2)
Sampling 2	(7,11)
Sampling 3	(4,11)

Table 4.4: Image shape of 7x11 windows in each sampling in (η, ϕ) .

It was decided to use the cell energy normalized to the total cluster energy as image pixel to build an energy independent algorithm which performs in the same way for all energy regime.

4.4.0.3 CNN Architecture

A CNN classifier is built to separate between prompt and background photons using images of the 7x11 cluster windows of sampling 1, 2, and 3. Figure 4.13 shows an illustration of the classifier.

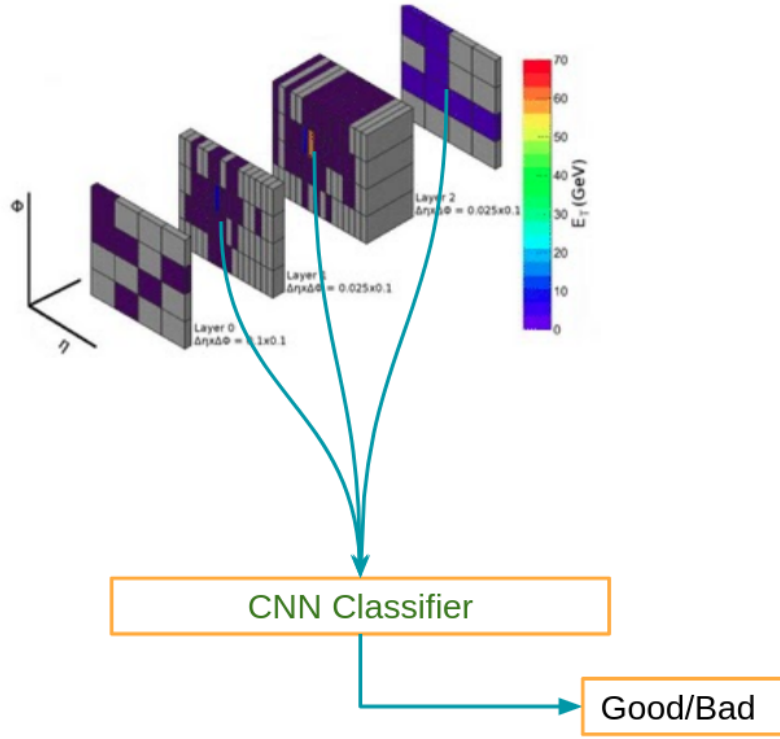


Figure 4.13: CNN classifier schema.

The Global CNN classifier is constructed using the KERAS library, with TENSORFLOW as a backend [84, 85]. Information from EM layers images is extracted using three babies CNN. Each one is connected to an EM layer and built from two sets of two-dimensional convolution (2DCov) and two-dimensional max-pooling (2DMaxPool) [86] layers followed by a flatten layer that prepares a vector for the fully connected network. Output vectors of the three flatten layers are combined using a concatenate layer, then pass through a Dense Neural Network (DNN) for the classification task. The DNN is made of two Dense (full connected) layers, a dropout, another Dense layer then a final output layer. An illustration of the architecture is given in Figure 4.14.

All layers in the network have their weights randomly initialized by sampling from a truncated normal distribution centred on zero with the width given by $\sqrt{1/N_{input}}$, where N_{input} is the number of input units in the weight tensor. The activation function of each layer is Scaled Exponential Linear Unit (SELU) [87] to preserve the mean and variance of the inputs between two consecutive layers and handle the normalization issues, except for the final output layer which has "sigmoid" as an activation function.

Layers in the babies CNN are 256 nodes wide, while in the DNN 128 nodes except for the output layer is one node wide.

Using an output layer with a sigmoid activation function allows interpreting the output as the probability for each class (Bad or Good photon), given the input images.

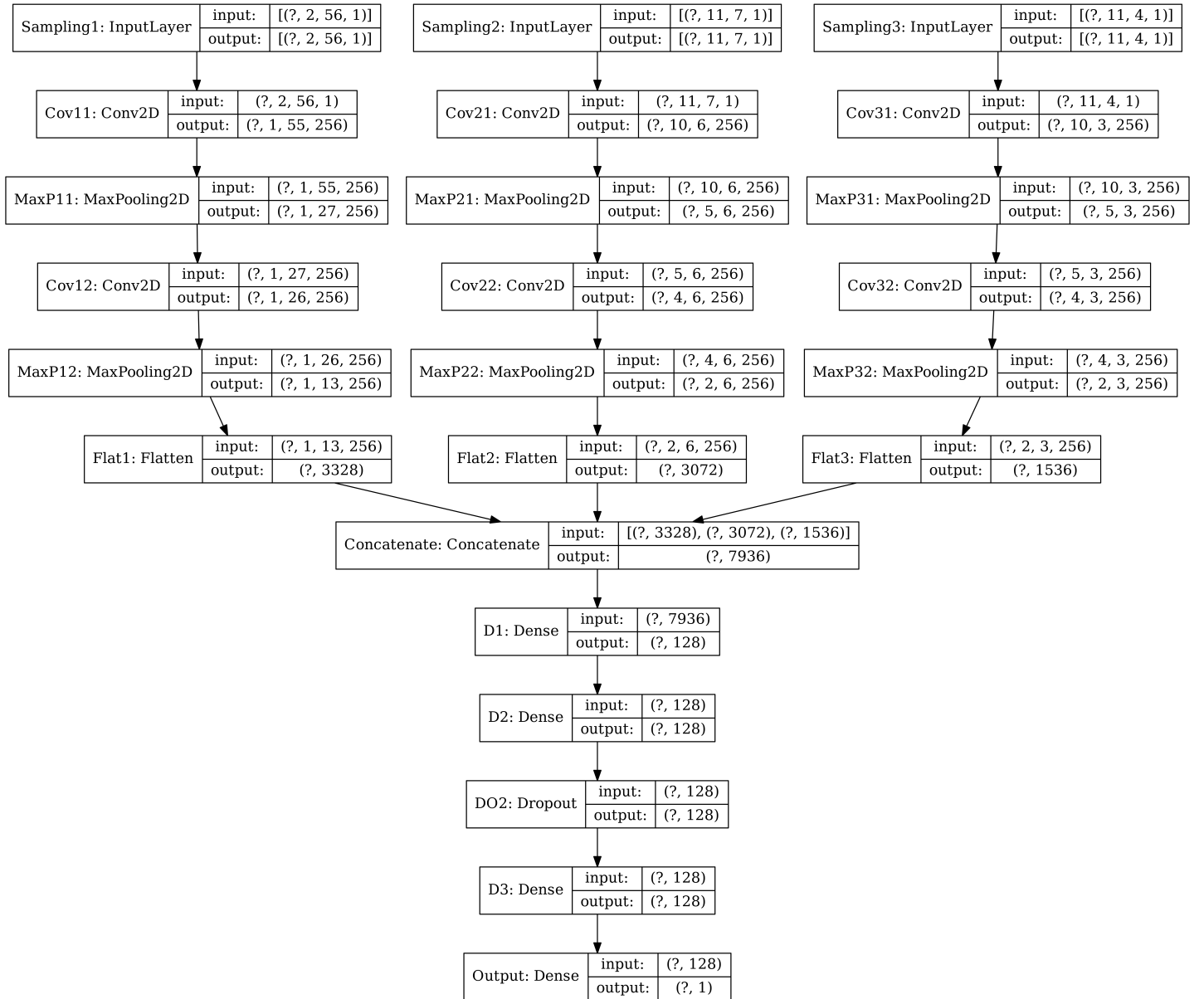


Figure 4.14: Illustration of the global CNN classifier graph.

In the network presented the dropout layer has a dropout rate of 8%.

During the training, the binary cross-entropy used as a loss metric, and Adam optimizer for the optimiza-

tion.

4.4.0.4 CNN Training

The CNN networks of $\sim 1.4\text{M}$ parameter is trained with a learning rate of $1e^{-4}$ and a batch size fixed to 96 images (32 photons) due to memory limitations, with a maximum number of epochs set to 20. CNN network is trained using two Tesla K80 GPUs with a memory of 12 GB each with ~ 15 min for each epoch run on CC-In2p3 cluster (France) [88]. An early stopping metric [89] is imposed during the training phase such that if the network's learning begins to the plateau it will stop, whether or not the maximum number of epochs is reached. The metric used to determine the early stopping is the network loss as evaluated on the validation data sample throughout the training. The network aims to minimize the weighted loss function between the truth and predicted labels. The network is trained inclusively in E_T , η , and photon conversion type. Only cluster images and no additional information is included during the training. Figure 4.15 shows the evaluation of loss function and the accuracy during the training time for the training and validation dataset. After the 4th epoch the network achieves the plateau and the validation loss do not decrease. To reduce the overtraining, the early stopping stops the training at epoch 4.

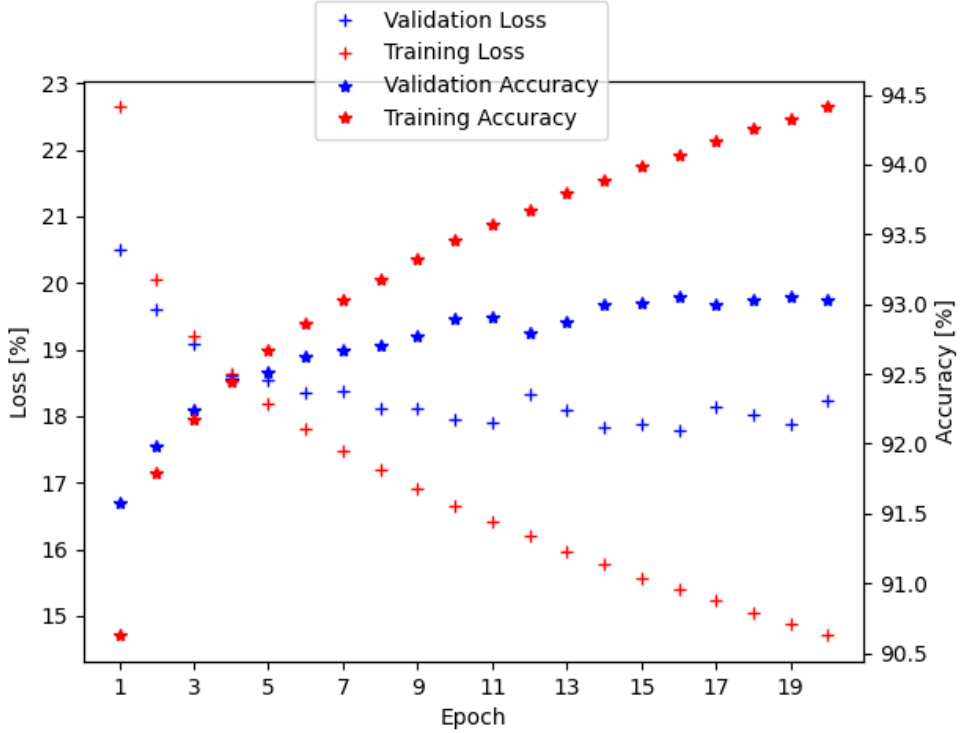


Figure 4.15: Neural network loss and accuracy as function of epoch number

4.4.0.5 CNN Validation

The CNN output is scanned to compute the improvement in background rejection for the same cut-based Tight WP signal efficiency and the signal efficiency for the same Tight WP background rejection in bins of photon p_T and $|\eta|$. The signal efficiency ϵ_{eff} and background rejection ϵ_{rej} are evaluated as the following :

$$\epsilon_{eff} = \frac{TP}{TP + FN} ; \epsilon_{rej} = \frac{TN}{TN + FP}, \quad (4.5)$$

where TP is the truth positive, TN the truth negative, FP the false positive and FN is the false negative rates. The following binning is used $p_T = [10, 20, 30, 40, 60, 80, \infty]$ and $|\eta| = [0., 0.6, 1.37, 1.52, 1.8, 2.4]$. Figure 4.16 shows the receiver-operating characteristic (ROC) which illustrates the diagnostic ability of the CNN as its discrimination threshold is varied. The blue dot shows the signal and background rejection of the current cut-based Tight WP, CNN demonstrates a significant performance over Tight WP for both converted and unconverted photons. Figure 4.17 shows the relative improvement over the Tight WP in

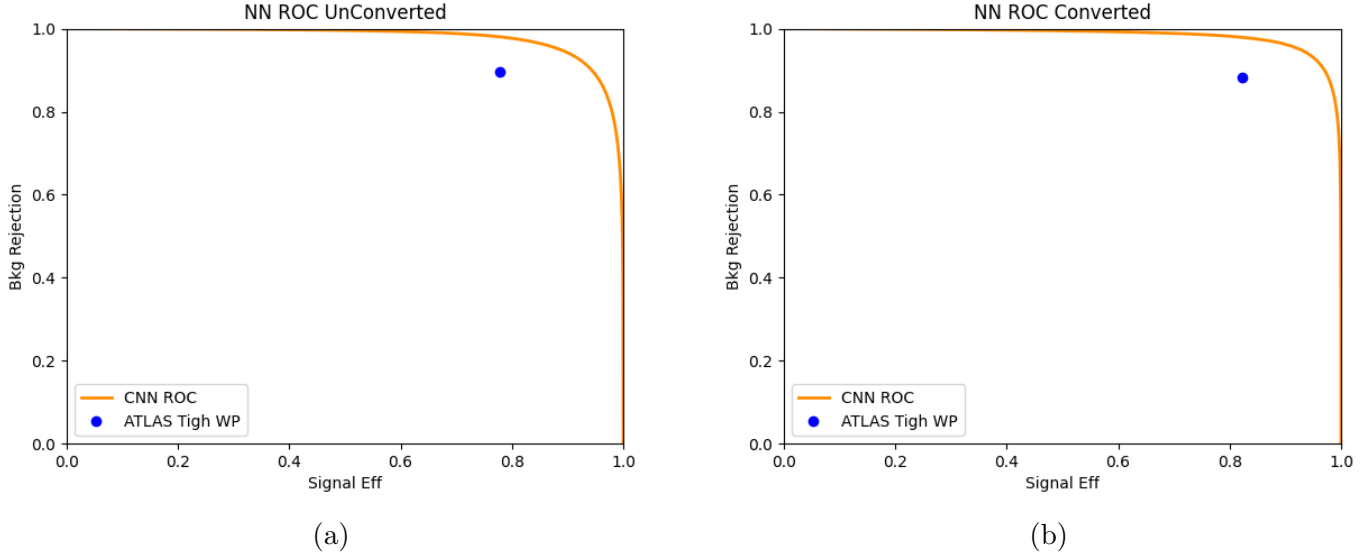


Figure 4.16: Network ROC curve for (a) Unconverted photons (b) Converted photons, the yellow line show the ROC curve and the blue dot show the Tight WP, x-axis is the ϵ_{eff} and y-axis show the ϵ_{rej} as defined in equation 4.5.

term of signal efficiency for the same background rejection. An improvement of up to 93% is achieved.

4.4.0.6 Out-of-Sample validation $Z \rightarrow ll\gamma$

Radiated photons from Z boson decay are used to evaluate the final improvement achieved by CNN after an appropriate optimization to define the CNN WPs. The optimization is done by maximizing the $\sqrt{(S/S + B)}$ with at least the same or higher background rejection as cut-based WPs which leads to maximize the signal efficiency. CNN output then is scanned in bins of $|\eta|$ for both converted and unconverted photons separately to define two WPs (Loose and Tight). To be more consistent with cut-based Tight WP the following binning is chosen : [0, 0.6, 0.8, 1.15, 1.37, 1.81, 2.01, 2.37]. The identification efficiency is evaluated using the Radiative Z method already described in Section 4.2.

Figure 4.18 shows the result identification efficiency for Tight and Loose WPs compared to cut-based Tight and Loose WPs respectively as a function of photon E_T . CNN over performs the cut-based algorithm for both WPs. The Loose CNN WP achieve an efficiency of 99% on the full energy spectrum. Without any correction, the CNN performs in the same way for both Data and MC (scale factor close to unity). The CNN is not sensitively to any shower shapes modelling as it uses the cell fraction energy where the mis-modelling is infinitesimal and not cached by the CNN algorithm, as Figure 4.20 shows no significance shift in the CNN distribution.

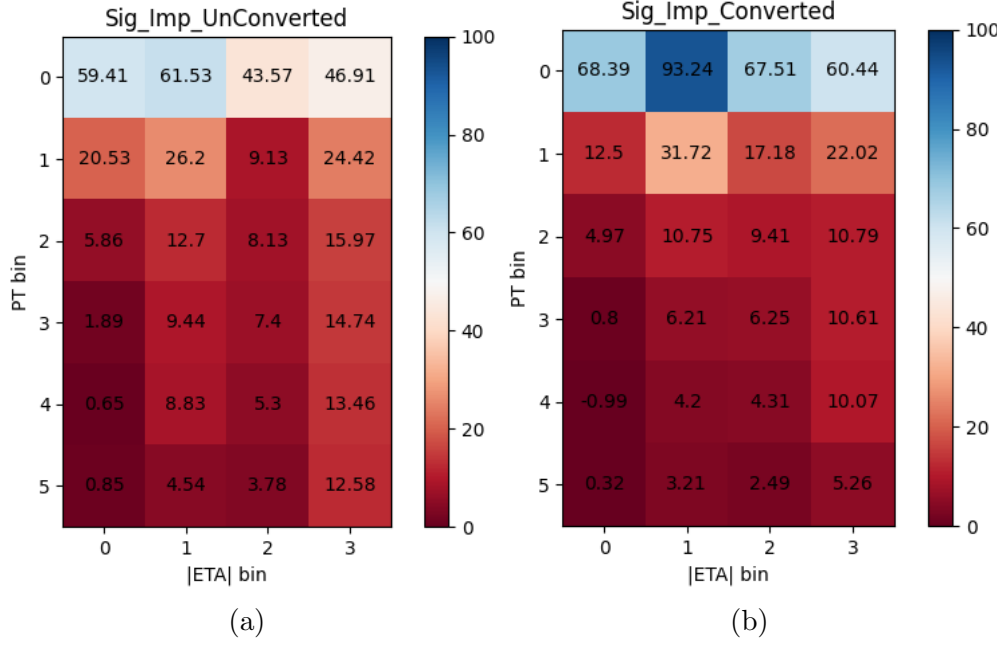


Figure 4.17: Relative signal efficiency improvement for similar Tight WP background rejection (a) for Unconverted photons and (b) Converted photons.

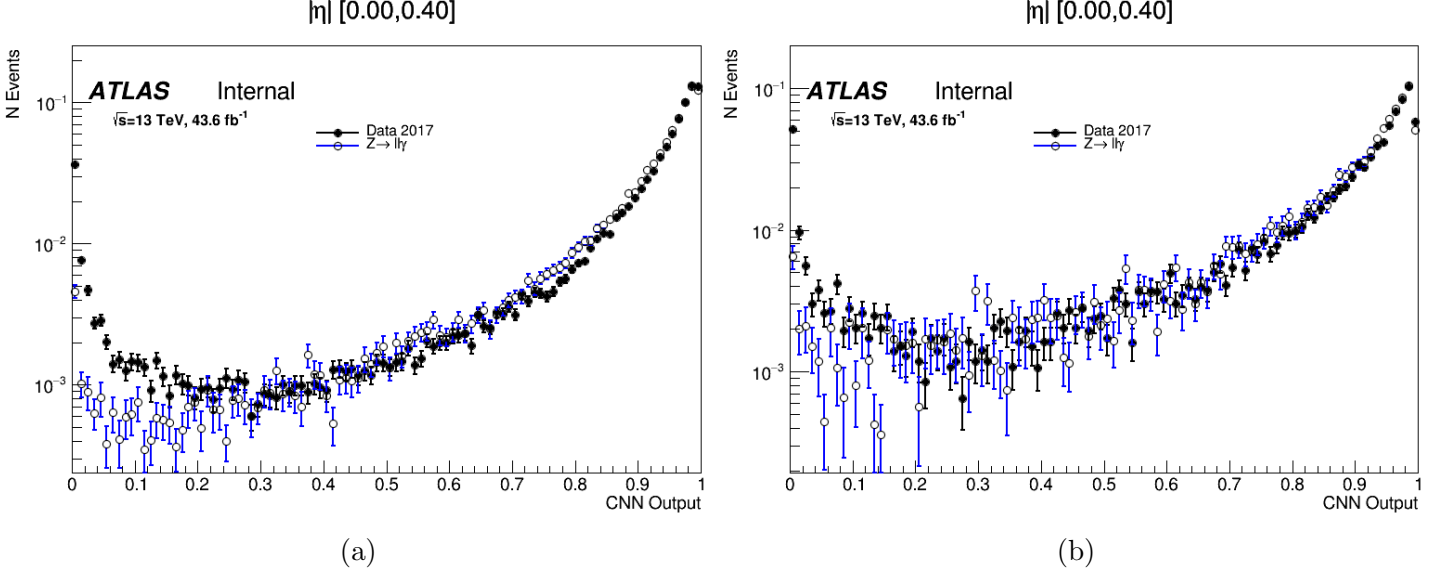


Figure 4.20: CNN output distribution as computed for data (black) and MC (blue) for (a) for Unconverted photons and (b) Converted photons with $|\eta| < 0.4$.

At low photon E_T and especially for high $|\eta|$, the efficiency dropped because photons with low E_T deposit more energy at the first sampling compared to photons with high E_T , and the zeros added to the first sampling whitens more than the half of the image which reduce the CNN learning ability for this category of photons.

The presence of additional pp interactions in the event affects the photon identification and isolation efficiencies. Figure 4.19 shows the evolution of photon identification efficiency as a function of pile up. A clear drop by $\sim 9\%-16\%$ when going from $\mu \sim 5$ to $\mu \sim 70$, depending on the photon candidate's pseudorapidity

and conversion status. The drop is explained by the additional activities around the hottest cell affecting the CNN performance of extracting the shower.

The proposed identification algorithm is getting integrated into the ATLAS Athena framework and is planned to be used as a baseline for Run 3.

Additional control plots are shown in the Appendix ()�.

4.5 Conclusion

As mentioned at the beginning of this chapter, photon identification is an essential ingredient to select and study the $HH \rightarrow \gamma\gamma b\bar{b}$ decay. ATLAS provides a cut-based algorithm that uses global shower shapes variables to identify prompt photons. However, the shower shapes are affected by the mis-modelling discrepancy leading to a scale factor far from one. Besides, the cut-based algorithm suffers from the features space dimensionality which limit its performance. The CNN algorithm provides a solution to these problems by using low-level detector information. Using the neural network with low-level detector information scale up the features space. The CNN over performs the cut-based method by generating its complicated variables and handling their correlations for better separation. Even with the performance achieved, CNN still needs to be improved to handle some issues, the low efficiency at low E_T and the pile-up effect which reduce its performance for high pile events. Appendix is dedicated to discuss future improvements for the CNN identification algorithm.

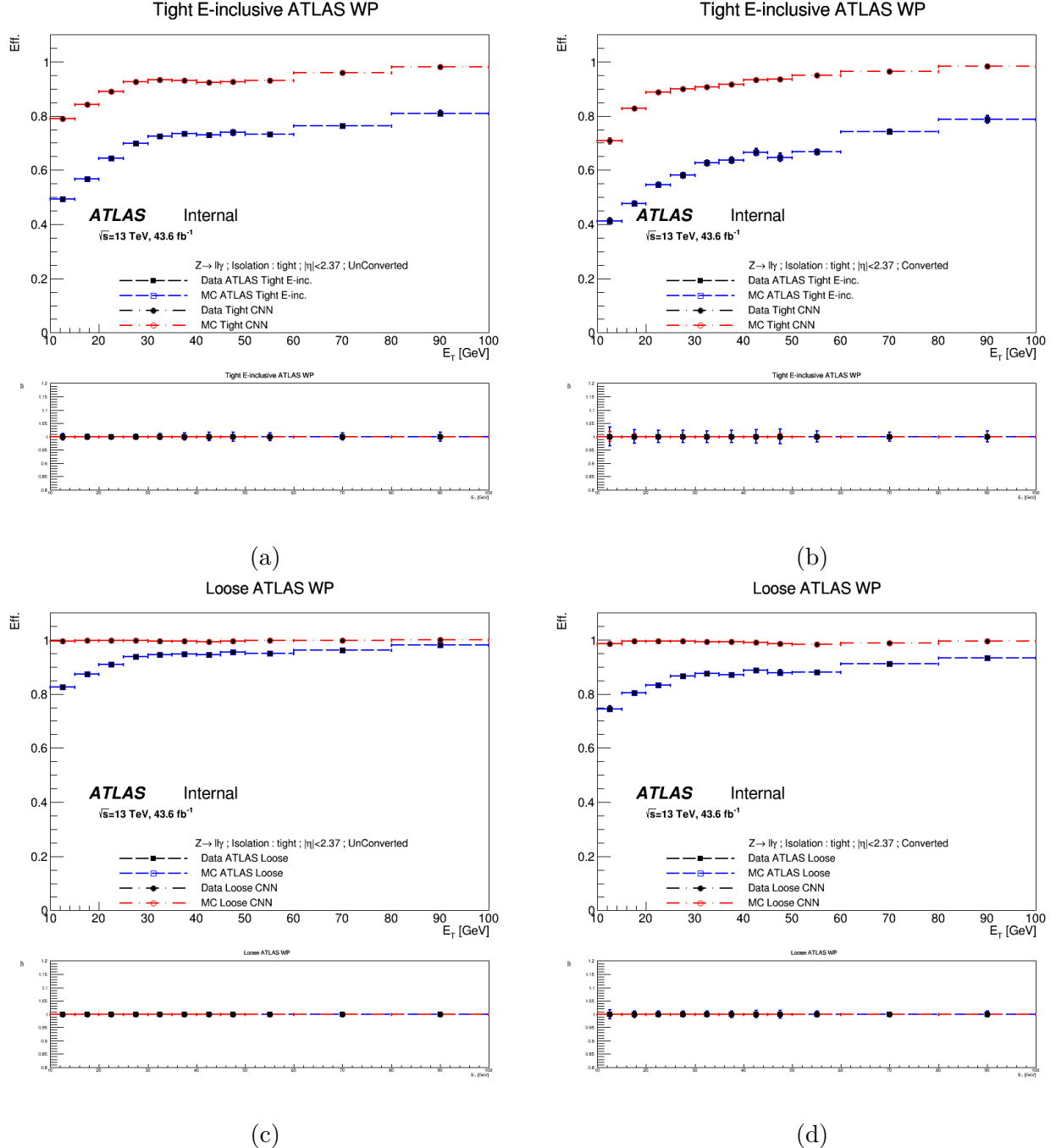


Figure 4.18: Photon identification efficiency for CNN (red) and cut-based (blue) indicated with ATLAS, for data (full marks) and MC (open marks). For both Tight WP (top) and Loose WP (bottom). Unconverted photons (right) and converted photons (left). As a function of photon E_T . Bottom ratios show the scale factors. 2017 Data is used.

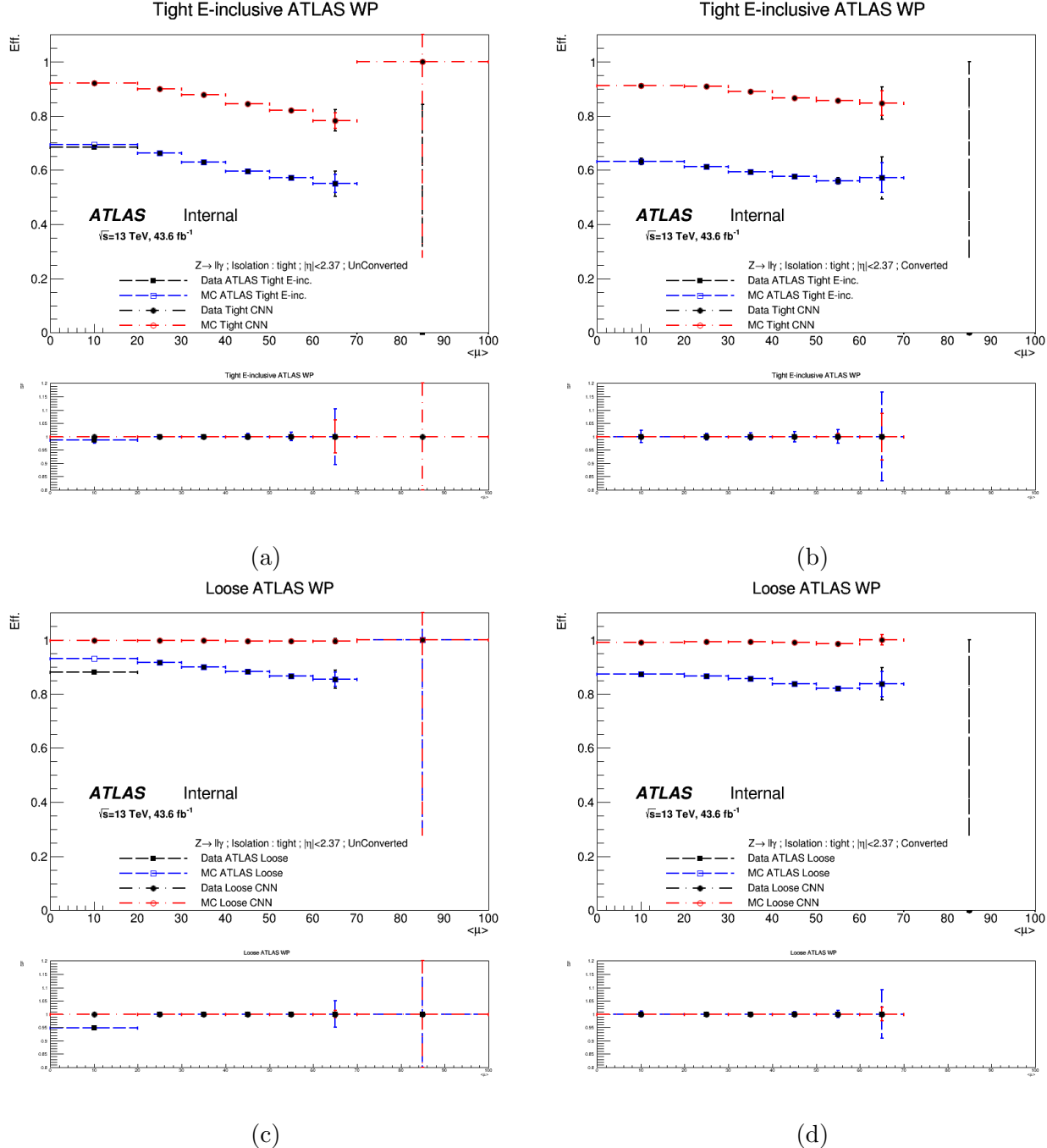


Figure 4.19: Photon identification efficiency for CNN (red) and cut-based (blue) indicated with ATLAS, for data (full marks) and MC (open marks). For both Tight WP (top) and Loose WP (bottom). Unconverted photons (right) and converted photons (left). As a function of pile up $\langle \mu \rangle$. Bottom ratios show the scale factors. 2017 Data is used.

Jets and Tagging in ATLAS

This includes :

- Introduction to Jet
- Jet reconstruction
- Jet Calibration
- Jet tagging (B-Tagger)
- B-Jet Calibration

5.1 Jet Reconstruction

This section will discuss the jet reconstruction algorithms Topological cluster and particle flow.

5.1.1 Topological Cluster

The topological reconstruction... and the moving for particle flow for run 2

5.1.2 Particle Flow

The particle flow algorithms, the main difference from the topological one.

5.2 Jet Tagging

Discuss the jet tagging algorithms JVT and b-tagging

5.2.1 Jet Vertex Tagging

This section will focus on the jet vertex tagger used in the analysis.

5.2.2 B-jet Tagger

This section will discuss the DLr1 and MV2c10 tagger to identify the b-jet.

5.3 Jet Energy Calibration

5.3.1 Jet Calibration Chain

This section will discuss the nominal jet calibration chain step by step.

5.3.2 B-Jet Calibration

The b-jet calibration work will fit here.

5.4 Conclusion

The conclusion of the chapter will be here in which I will introduce the b-jet regression by jannicke as an alternative solution for run 3.

Experimental Setup for Self-coupling measurement

This chapter should include the HH analysis and κ_λ limits

Conclusion

Appendix 1

Bibliography

- [1] M. Tanabashi et al. “Review of Particle Physics”. In: *Phys. Rev. D* 98 (3 2018), p. 030001. DOI: 10.1103/PhysRevD.98.030001. URL: <https://link.aps.org/doi/10.1103/PhysRevD.98.030001>.
- [2] G. Arnison et al. “Experimental observation of isolated large transverse energy electrons with associated missing energy at $s=540\text{ GeV}$ ”. In: *Physics Letters B* 122.1 (1983), pp. 103–116. ISSN: 0370-2693. DOI: [https://doi.org/10.1016/0370-2693\(83\)91177-2](https://doi.org/10.1016/0370-2693(83)91177-2). URL: <http://www.sciencedirect.com/science/article/pii/0370269383911772>.
- [3] P. Bagnaia et al. “Evidence for $Z \rightarrow e^+e^-$ at the CERN pp collider”. In: *Physics Letters B* 129.1 (1983), pp. 130–140. ISSN: 0370-2693. DOI: [https://doi.org/10.1016/0370-2693\(83\)90744-X](https://doi.org/10.1016/0370-2693(83)90744-X). URL: <http://www.sciencedirect.com/science/article/pii/037026938390744X>.
- [4] F. Englert and R. Brout. “Broken Symmetry and the Mass of Gauge Vector Mesons”. In: *Phys. Rev. Lett.* 13 (9 1964), pp. 321–323. DOI: 10.1103/PhysRevLett.13.321. URL: <https://link.aps.org/doi/10.1103/PhysRevLett.13.321>.
- [5] John Ellis, Mary K. Gaillard, and Dimitri V. Nanopoulos. *A Historical Profile of the Higgs Boson*. 2012. arXiv: 1201.6045 [hep-ph].
- [6] David Delgove. “Mesure des propriétés du boson de Higgs avec l’expérience ATLAS au LHC”. Theses. Université Paris-Saclay, 2016. URL: <https://tel.archives-ouvertes.fr/tel-01494070>.
- [7] In: *Physics Letters B* 565 (2003), pp. 61–75. ISSN: 0370-2693. DOI: 10.1016/S0370-2693(03)00614-2. URL: [http://dx.doi.org/10.1016/S0370-2693\(03\)00614-2](http://dx.doi.org/10.1016/S0370-2693(03)00614-2).
- [8] T. Aaltonen et al. “Combination of Tevatron Searches for the Standard Model Higgs Boson in the W+W-Decay Mode”. In: *Physical Review Letters* 104.6 (2010). ISSN: 1079-7114. DOI: 10.1103/physrevlett.104.061802. URL: <http://dx.doi.org/10.1103/PhysRevLett.104.061802>.
- [9] ALEPH Collaboration et al. *Precision Electroweak Measurements and Constraints on the Standard Model*. 2009. arXiv: 0911.2604 [hep-ex].
- [10] Sayipjamal Dulat et al. “New parton distribution functions from a global analysis of quantum chromodynamics”. In: *Physical Review D* 93.3 (2016). ISSN: 2470-0029. DOI: 10.1103/physrevd.93.033006. URL: <http://dx.doi.org/10.1103/PhysRevD.93.033006>.
- [11] Sayipjamal Dulat et al. “New parton distribution functions from a global analysis of quantum chromodynamics”. In: *Physical Review D* 93.3 (2016). ISSN: 2470-0029. DOI: 10.1103/physrevd.93.033006. URL: <http://dx.doi.org/10.1103/PhysRevD.93.033006>.
- [12] *LHC Higgs Working Group*. URL: <https://twiki.cern.ch/twiki/bin/view/LHCPhysics/LHCHWG?redirectedfrom=LHCPhysics.LHCHXSWG>.
- [13] S. Dittmaier et al. “Handbook of LHC Higgs Cross Sections: 1. Inclusive Observables”. In: (2011). DOI: 10.5170/CERN-2011-002. arXiv: 1101.0593 [hep-ph].

- [14] S. Dittmaier et al. “Handbook of LHC Higgs Cross Sections: 2. Differential Distributions”. In: (2012). DOI: 10.5170/CERN-2012-002. arXiv: 1201.3084 [hep-ph].
- [15] D. de Florian et al. “Handbook of LHC Higgs Cross Sections: 4. Deciphering the Nature of the Higgs Sector”. In: 2/2017 (2016). DOI: 10.23731/CYRM-2017-002. arXiv: 1610.07922 [hep-ph].
- [16] G. Aad et al. “Observation of a new particle in the search for the Standard Model Higgs boson with the ATLAS detector at the LHC”. In: *Physics Letters B* 716.1 (2012), pp. 1–29. ISSN: 0370-2693. DOI: 10.1016/j.physletb.2012.08.020. URL: <http://dx.doi.org/10.1016/j.physletb.2012.08.020>.
- [17] S. Chatrchyan et al. “Observation of a new boson at a mass of 125 GeV with the CMS experiment at the LHC”. In: *Physics Letters B* 716.1 (2012), pp. 30–61. ISSN: 0370-2693. DOI: 10.1016/j.physletb.2012.08.021. URL: <http://dx.doi.org/10.1016/j.physletb.2012.08.021>.
- [18] Aad and *al.* “Combined Measurement of the Higgs Boson Mass in pp Collisions at $\sqrt{s} = 7$ and 8 TeV with the ATLAS and CMS Experiments”. In: *Phys. Rev. Lett.* 114 (19 2015), p. 191803. DOI: 10.1103/PhysRevLett.114.191803. URL: <https://link.aps.org/doi/10.1103/PhysRevLett.114.191803>.
- [19] *Measurement of the properties of Higgs boson production at $\sqrt{s}=13$ TeV in the $H \rightarrow \gamma\gamma$ channel using 139 fb^{-1} of pp collision data with the ATLAS experiment*. Tech. rep. ATLAS-CONF-2020-026. Geneva: CERN, 2020. URL: <https://cds.cern.ch/record/2725727>.
- [20] D. de Florian et al. *Handbook of LHC Higgs Cross Sections: 4. Deciphering the Nature of the Higgs Sector*. CERN Yellow Reports: Monographs. 869 pages, 295 figures, 248 tables and 1645 citations. Working Group web page: <https://twiki.cern.ch/twiki/bin/view/LHCPhysics/LHCHXSWG>. 2016. DOI: 10.23731/CYRM-2017-002. URL: <http://cds.cern.ch/record/2227475>.
- [21] S. Borowka et al. “Higgs Boson Pair Production in Gluon Fusion at Next-to-Leading Order with Full Top-Quark Mass Dependence”. In: *Phys. Rev. Lett.* 117 (1 2016), p. 012001. DOI: 10.1103/PhysRevLett.117.012001. URL: <https://link.aps.org/doi/10.1103/PhysRevLett.117.012001>.
- [22] Aaboud et al. “Search for Higgs boson pair production in the $\gamma\gamma b\bar{b}$ final state with 13 TeV pp collision data collected by the ATLAS experiment”. In: (2018). URL: <http://cds.cern.ch/record/2630823>.
- [23] G. Aad et al. “Combination of searches for Higgs boson pairs in pp collisions at $s=13\text{TeV}$ with the ATLAS detector”. In: *Physics Letters B* 800 (2020), p. 135103. ISSN: 0370-2693. DOI: 10.1016/j.physletb.2019.135103. URL: <http://dx.doi.org/10.1016/j.physletb.2019.135103>.
- [24] M. Aaboud et al. “Search for Resonant and Non-resonant Higgs Boson Pair Production in the $b\bar{b}\tau^+\tau^-$ Decay Channel in pp Collisions at $\sqrt{s} = 13$ TeV with the ATLAS Detector”. In: *Physical Review Letters* 121.19 (2018). ISSN: 1079-7114. DOI: 10.1103/physrevlett.121.191801. URL: <http://dx.doi.org/10.1103/PhysRevLett.121.191801>.
- [25] M. Aaboud et al. “Search for pair production of Higgs bosons in the $b\bar{b}b\bar{b}$ final state using proton-proton collisions at $\sqrt{s} = 13$ TeV with the ATLAS detector”. In: *Journal of High Energy Physics* 2019.1 (2019). ISSN: 1029-8479. DOI: 10.1007/jhep01(2019)030. URL: [http://dx.doi.org/10.1007/JHEP01\(2019\)030](http://dx.doi.org/10.1007/JHEP01(2019)030).
- [26] M. Aaboud et al. “Search for Higgs boson pair production in the $WW^{(*)}WW^{(*)}$ decay channel using ATLAS data recorded at $\sqrt{s} = 13$ TeV”. In: *Journal of High Energy Physics* 2019.5 (2019). ISSN: 1029-8479. DOI: 10.1007/jhep05(2019)124. URL: [http://dx.doi.org/10.1007/JHEP05\(2019\)124](http://dx.doi.org/10.1007/JHEP05(2019)124).

- [27] M. Aaboud et al. “Search for Higgs boson pair production in the $\gamma\gamma WW^*$ channel using pp collision data recorded at $\sqrt{s}=13$ TeV with the ATLAS detector”. In: *The European Physical Journal C* 78.12 (2018). ISSN: 1434-6052. DOI: 10.1140/epjc/s10052-018-6457-x. URL: <http://dx.doi.org/10.1140/epjc/s10052-018-6457-x>.
- [28] M. Aaboud et al. “Search for Higgs boson pair production in the $b\bar{b}WW^*$ decay mode at $\sqrt{s} = 13$ TeV with the ATLAS detector”. In: *Journal of High Energy Physics* 2019.4 (2019). ISSN: 1029-8479. DOI: 10.1007/jhep04(2019)092. URL: [http://dx.doi.org/10.1007/JHEP04\(2019\)092](http://dx.doi.org/10.1007/JHEP04(2019)092).
- [29] Ilaria Brivio, Yun Jiang, and Michael Trott. “The SMEFTsim package, theory and tools”. In: *Journal of High Energy Physics* 2017.12 (2017). ISSN: 1029-8479. DOI: 10.1007/jhep12(2017)070. URL: [http://dx.doi.org/10.1007/JHEP12\(2017\)070](http://dx.doi.org/10.1007/JHEP12(2017)070).
- [30] B. Grzadkowski et al. “Dimension-six terms in the Standard Model Lagrangian”. In: *Journal of High Energy Physics* 2010.10 (2010). ISSN: 1029-8479. DOI: 10.1007/jhep10(2010)085. URL: [http://dx.doi.org/10.1007/JHEP10\(2010\)085](http://dx.doi.org/10.1007/JHEP10(2010)085).
- [31] Ilaria Brivio and Michael Trott. “The standard model as an effective field theory”. In: *Physics Reports* 793 (2019), pp. 1–98. ISSN: 0370-1573. DOI: 10.1016/j.physrep.2018.11.002. URL: <http://dx.doi.org/10.1016/j.physrep.2018.11.002>.
- [32] Oliver Sim Brüning et al. *LHC Design Report*. CERN Yellow Reports: Monographs. Geneva: CERN, 2004. DOI: 10.5170/CERN-2004-003-V-1. URL: <https://cds.cern.ch/record/782076>.
- [33] Cinzia De Melis. “The CERN accelerator complex. Complexe des accélérateurs du CERN”. In: (2016). General Photo. URL: <https://cds.cern.ch/record/2119882>.
- [34] The ATLAS Collaboration. *Public luminosity results*. URL: https://twiki.cern.ch/twiki/bin/view/AtlasPublic/LuminosityPublicResultsRun2#Multiple_Year_Collision_Plots.
- [35] The ATLAS Collaboration et al. “The ATLAS Experiment at the CERN Large Hadron Collider”. In: *Journal of Instrumentation* 3.08 (2008), S08003–S08003. DOI: 10.1088/1748-0221/3/08/s08003. URL: <https://doi.org/10.1088/1748-0221/3/08/s08003>.
- [36] *ATLAS inner detector: Technical Design Report, 1*. Technical design report. ATLAS. Geneva: CERN, 1997. URL: <https://cds.cern.ch/record/331063>.
- [37] Kyungeon Choi. *Tracking and Vertexing with the ATLAS Inner Detector in the LHC Run-2*. Tech. rep. ATL-PHYS-PROC-2017-075. Geneva: CERN, 2017. DOI: 10.1007/978-981-13-1316-5_75. URL: <https://cds.cern.ch/record/2271033>.
- [38] Karolos Potamianos. *The upgraded Pixel detector and the commissioning of the Inner Detector tracking of the ATLAS experiment for Run-2 at the Large Hadron Collider*. Tech. rep. ATL-PHYS-PROC-2016-104. 15 pages, EPS-HEP 2015 Proceedings. Geneva: CERN, 2016. URL: <https://cds.cern.ch/record/2209070>.
- [39] M Capeans et al. *ATLAS Insertable B-Layer Technical Design Report*. Tech. rep. CERN-LHCC-2010-013. ATLAS-TDR-19. 2010. URL: <https://cds.cern.ch/record/1291633>.
- [40] ATLAS Collaboration. *Impact Parameter Resolution*. URL: <https://atlas.web.cern.ch/Atlas/GROUPS/PHYSICS/PLLOTS/IDTR-2015-007/>.
- [41] *Timing improvements for the ATLAS offline reconstruction for run-2*. Tech. rep. ATL-SOFT-PUB-2014-004. Geneva: CERN, 2014. URL: <https://cds.cern.ch/record/1955923>.

- [42] ATLAS Collaboration. *The Optimization of ATLAS Track Reconstruction in Dense Environments*. URL: <https://atlas.web.cern.ch/Atlas/GROUPS/PHYSICS/PUBNOTES/ATL-PHYS-PUB-2015-006/>.
- [43] *Expected performance of the ATLAS b-tagging algorithms in Run-2*. Tech. rep. ATL-PHYS-PUB-2015-022. Geneva: CERN, 2015. URL: <http://cds.cern.ch/record/2037697>.
- [44] *Commissioning of the ATLAS high-performance b-tagging algorithms in the 7 TeV collision data*. Tech. rep. ATLAS-CONF-2011-102. Geneva: CERN, 2011. URL: <http://cds.cern.ch/record/1369219>.
- [45] T G Cornelissen et al. *Updates of the ATLAS Tracking Event Data Model (Release 13)*. Tech. rep. ATL-SOFT-PUB-2007-003. ATL-COM-SOFT-2007-008. Geneva: CERN, 2007. URL: <https://cds.cern.ch/record/1038095>.
- [46] *ATLAS liquid-argon calorimeter: Technical Design Report*. Technical design report. ATLAS. Geneva: CERN, 1996. URL: <https://cds.cern.ch/record/331061>.
- [47] *ATLAS tile calorimeter: Technical Design Report*. Technical design report. ATLAS. Geneva: CERN, 1996. URL: <https://cds.cern.ch/record/331062>.
- [48] A. Hrynevich. “Performance of the ATLAS Tile Calorimeter”. In: *Journal of Instrumentation* 12.06 (2017), pp. C06021–C06021. DOI: [10.1088/1748-0221/12/06/c06021](https://doi.org/10.1088/1748-0221/12/06/c06021). URL: <https://doi.org/10.1088/1748-0221/12/06/c06021>.
- [49] *ATLAS muon spectrometer: Technical Design Report*. Technical design report. ATLAS. Geneva: CERN, 1997. URL: <https://cds.cern.ch/record/331068>.
- [50] A. Airapetian et al. *ATLAS detector and physics performance: Technical Design Report, 1*. Technical design report. ATLAS. Geneva: CERN, 1999. URL: <https://cds.cern.ch/record/391176>.
- [51] *ATLAS level-1 trigger: Technical Design Report*. Technical design report. ATLAS. Geneva: CERN, 1998. URL: <https://cds.cern.ch/record/381429>.
- [52] Peter Jenni et al. *ATLAS high-level trigger, data-acquisition and controls: Technical Design Report*. Technical design report. ATLAS. Geneva: CERN, 2003. URL: <https://cds.cern.ch/record/616089>.
- [53] T. Golling et al. “The ATLAS data quality defect database system”. In: *The European Physical Journal C* 72.4 (2012). ISSN: 1434-6052. DOI: [10.1140/epjc/s10052-012-1960-y](https://doi.org/10.1140/epjc/s10052-012-1960-y). URL: <http://dx.doi.org/10.1140/epjc/s10052-012-1960-y>.
- [54] *Performance of the ATLAS Inner Detector Track and Vertex Reconstruction in the High Pile-Up LHC Environment*. Tech. rep. ATLAS-CONF-2012-042. Geneva: CERN, 2012. URL: <https://cds.cern.ch/record/1435196>.
- [55] T Cornelissen et al. *Concepts, Design and Implementation of the ATLAS New Tracking (NEWT)*. Tech. rep. ATL-SOFT-PUB-2007-007. ATL-COM-SOFT-2007-002. Geneva: CERN, 2007. URL: <https://cds.cern.ch/record/1020106>.
- [56] R. Frühwirth. “Application of Kalman filtering to track and vertex fitting”. In: *Nuclear Instruments and Methods in Physics Research Section A: Accelerators, Spectrometers, Detectors and Associated Equipment* 262.2 (1987), pp. 444–450. ISSN: 0168-9002. DOI: [https://doi.org/10.1016/0168-9002\(87\)90887-4](https://doi.org/10.1016/0168-9002(87)90887-4). URL: <http://www.sciencedirect.com/science/article/pii/0168900287908874>.

- [57] *Performance of the ATLAS Inner Detector Track and Vertex Reconstruction in the High Pile-Up LHC Environment*. Tech. rep. ATLAS-CONF-2012-042. Geneva: CERN, 2012. URL: <https://cds.cern.ch/record/1435196>.
- [58] T G Cornelissen et al. “The global 2track fitter in ATLAS”. In: *Journal of Physics: Conference Series* 119.3 (2008), p. 032013. DOI: 10.1088/1742-6596/119/3/032013. URL: <https://doi.org/10.1088/1742-6596/119/3/032013>.
- [59] W Lampl et al. *Calorimeter Clustering Algorithms: Description and Performance*. Tech. rep. ATL-LARG-PUB-2008-002. ATL-COM-LARG-2008-003. Geneva: CERN, 2008. URL: <https://cds.cern.ch/record/1099735>.
- [60] G. Aad et al. “Electron and photon performance measurements with the ATLAS detector using the 2015–2017 LHC proton-proton collision data”. In: *Journal of Instrumentation* 14.12 (2019), P12006–P12006. ISSN: 1748-0221. DOI: 10.1088/1748-0221/14/12/p12006. URL: <http://dx.doi.org/10.1088/1748-0221/14/12/P12006>.
- [61] G. Aad et al. “Topological cell clustering in the ATLAS calorimeters and its performance in LHC Run 1”. In: *The European Physical Journal C* 77.7 (2017). ISSN: 1434-6052. DOI: 10.1140/epjc/s10052-017-5004-5. URL: <http://dx.doi.org/10.1140/epjc/s10052-017-5004-5>.
- [62] *Improved electron reconstruction in ATLAS using the Gaussian Sum Filter-based model for bremsstrahlung*. Tech. rep. ATLAS-CONF-2012-047. Geneva: CERN, 2012. URL: <https://cds.cern.ch/record/1449796>.
- [63] M. Aaboud et al. “Electron and photon energy calibration with the ATLAS detector using 2015–2016 LHC proton-proton collision data”. In: *Journal of Instrumentation* 14.03 (2019), P03017–P03017. ISSN: 1748-0221. DOI: 10.1088/1748-0221/14/03/p03017. URL: <http://dx.doi.org/10.1088/1748-0221/14/03/P03017>.
- [64] G. Aad et al. “Electron and photon energy calibration with the ATLAS detector using LHC Run 1 data”. In: *The European Physical Journal C* 74.10 (2014). ISSN: 1434-6052. DOI: 10.1140/epjc/s10052-014-3071-4. URL: <http://dx.doi.org/10.1140/epjc/s10052-014-3071-4>.
- [65] M. Aaboud et al. “Electron reconstruction and identification in the ATLAS experiment using the 2015 and 2016 LHC proton–proton collision data at $\sqrt{s} = 13$ TeV”. In: *The European Physical Journal C* 79.8 (2019). ISSN: 1434-6052. DOI: 10.1140/epjc/s10052-019-7140-6. URL: <http://dx.doi.org/10.1140/epjc/s10052-019-7140-6>.
- [66] Matteo Cacciari and Gavin P. Salam. “Pileup subtraction using jet areas”. In: *Physics Letters B* 659.1-2 (2008), pp. 119–126. ISSN: 0370-2693. DOI: 10.1016/j.physletb.2007.09.077. URL: <http://dx.doi.org/10.1016/j.physletb.2007.09.077>.
- [67] G. Aad et al. “Electron and photon performance measurements with the ATLAS detector using the 2015–2017 LHC proton-proton collision data”. In: *Journal of Instrumentation* 14.12 (2019), P12006–P12006. ISSN: 1748-0221. DOI: 10.1088/1748-0221/14/12/p12006. URL: <http://dx.doi.org/10.1088/1748-0221/14/12/P12006>.
- [68] David W. Scott. *Multivariate Density Estimation: Theory, Practice, and Visualization*. Wiley Series In Probability and Statistics. WILEY, 2015.
- [69] Andreas Hocker et al. *TMVA - Toolkit for Multivariate Data Analysis with ROOT: Users guide. TMVA - Toolkit for Multivariate Data Analysis*. Tech. rep. physics/0703039. TMVA-v4 Users Guide: 135 pages, 19 figures, numerous code examples and references. Geneva: CERN, 2007. URL: <https://cds.cern.ch/record/1019880>.

- [70] M. Aaboud et al. “Electron reconstruction and identification in the ATLAS experiment using the 2015 and 2016 LHC proton–proton collision data at $\sqrt{s} = 13$ TeV”. In: *The European Physical Journal C* 79.8 (2019). ISSN: 1434-6052. DOI: 10.1140/epjc/s10052-019-7140-6. URL: <http://dx.doi.org/10.1140/epjc/s10052-019-7140-6>.
- [71] J. Illingworth and J. Kittler. “A survey of the hough transform”. In: *Computer Vision, Graphics, and Image Processing* 44.1 (1988), pp. 87–116. ISSN: 0734-189X. DOI: [https://doi.org/10.1016/S0734-189X\(88\)80033-1](https://doi.org/10.1016/S0734-189X(88)80033-1). URL: <https://www.sciencedirect.com/science/article/pii/S0734189X88800331>.
- [72] G. Aad et al. “Measurement of the muon reconstruction performance of the ATLAS detector using 2011 and 2012 LHC proton–proton collision data”. In: *The European Physical Journal C* 74.11 (2014). ISSN: 1434-6052. DOI: 10.1140/epjc/s10052-014-3130-x. URL: <http://dx.doi.org/10.1140/epjc/s10052-014-3130-x>.
- [73] G. Aad et al. “Muon reconstruction performance of the ATLAS detector in proton–proton collision data at $\sqrt{s} = 13$ TeV”. In: *The European Physical Journal C* 76.5 (2016). ISSN: 1434-6052. DOI: 10.1140/epjc/s10052-016-4120-y. URL: <http://dx.doi.org/10.1140/epjc/s10052-016-4120-y>.
- [74] G. Aad et al. “Measurements of Higgs boson production and couplings in the four-lepton channel in pp collisions at center-of-mass energies of 7 and 8 TeV with the ATLAS detector”. In: *Physical Review D* 91.1 (2015). ISSN: 1550-2368. DOI: 10.1103/physrevd.91.012006. URL: <http://dx.doi.org/10.1103/PhysRevD.91.012006>.
- [75] G. Aad et al. “Search for new particles in events with one lepton and missing transverse momentum in pp collisions at $\sqrt{s} = 8$ TeV with the ATLAS detector”. In: *Journal of High Energy Physics* 2014.9 (2014). ISSN: 1029-8479. DOI: 10.1007/jhep09(2014)037. URL: [http://dx.doi.org/10.1007/JHEP09\(2014\)037](http://dx.doi.org/10.1007/JHEP09(2014)037).
- [76] G. Aad et al. “Search for high-mass dilepton resonances in pp collisions at $\sqrt{s}=8$ TeV with the ATLAS detector”. In: *Physical Review D* 90.5 (2014). ISSN: 1550-2368. DOI: 10.1103/physrevd.90.052005. URL: <http://dx.doi.org/10.1103/PhysRevD.90.052005>.
- [77] A. Hrynevich. “ATLAS jet and missing energy reconstruction, calibration and performance in LHC Run-2”. In: *Journal of Instrumentation* 12.06 (2017), pp. C06038–C06038. DOI: 10.1088/1748-0221/12/06/c06038. URL: <https://doi.org/10.1088/1748-0221/12/06/c06038>.
- [78] Matteo Cacciari, Gavin P Salam, and Gregory Soyez. “The anti-ktjet clustering algorithm”. In: *Journal of High Energy Physics* 2008.04 (2008), pp. 063–063. ISSN: 1029-8479. DOI: 10.1088/1126-6708/2008/04/063. URL: <http://dx.doi.org/10.1088/1126-6708/2008/04/063>.
- [79] G. Aad et al. “Electron performance measurements with the ATLAS detector using the 2010 LHC proton-proton collision data”. In: *The European Physical Journal C* 72.3 (2012). ISSN: 1434-6052. DOI: 10.1140/epjc/s10052-012-1909-1. URL: <http://dx.doi.org/10.1140/epjc/s10052-012-1909-1>.
- [80] P. Colangelo, F. Fazio, and G. Nardulli. “A STUDY OF THE REACTIONS OF”. In: 1992.
- [81] James Saxon. “Discovery of the Higgs Boson, Measurements of its Production, and a Search for Higgs Boson Pair Production”. Presented 13 06 2014. 2014. URL: <https://cds.cern.ch/record/1746004>.

- [82] M. Aaboud et al. “Measurement of the photon identification efficiencies with the ATLAS detector using LHC Run 2 data collected in 2015 and 2016”. In: *The European Physical Journal C* 79.3 (2019). ISSN: 1434-6052. DOI: 10.1140/epjc/s10052-019-6650-6. URL: <http://dx.doi.org/10.1140/epjc/s10052-019-6650-6>.
- [83] M. Aaboud et al. “Measurement of the photon identification efficiencies with the ATLAS detector using LHC Run-1 data”. In: *The European Physical Journal C* 76.12 (2016). ISSN: 1434-6052. DOI: 10.1140/epjc/s10052-016-4507-9. URL: <http://dx.doi.org/10.1140/epjc/s10052-016-4507-9>.
- [84] F. Chollet et al. *Keras*. <https://keras.io/>. 2015.
- [85] M. Abadi et al. *TensorFlow: Large-Scale Machine Learning on Heterogeneous Systems, Software available from tensorflow.org*. <http://tensorflow.org/>. 2015.
- [86] Keras. *Pooling layers*. https://keras.io/api/layers/pooling_layers/. 2015.
- [87] Zhen Huang et al. *SNDCNN: Self-normalizing deep CNNs with scaled exponential linear units for speech recognition*. <https://arxiv.org/abs/1910.01992>. 2019.
- [88] Centre de Calcul de l’Institut National de Physique Nucléaire et de Physique des Particules, Lyon (France). <https://cc.in2p3.fr/>. 1976.
- [89] Yuan Yao, Lorenzo Rosasco, and Andrea Caponnetto. “On early stopping in gradient descent learning”. In: (2007).